

GRID IMPEDANCE ESTIMATION BASED ADAPTIVE CONTROLLER
DESIGN FOR BACK-TO-BACK WIND TURBINE POWER CONVERTERS FOR
STABLE OPERATION IN DISTORTED AND WEAK GRID

A THESIS SUBMITTED TO
THE GRADUATE SCHOOL OF NATURAL AND APPLIED SCIENCES
OF
MIDDLE EAST TECHNICAL UNIVERSITY

BY

HAKAN TEMIZ

IN PARTIAL FULFILLMENT OF THE REQUIREMENTS
FOR
THE DEGREE OF MASTER OF SCIENCE
IN
ELECTRICAL AND ELECTRONICS ENGINEERING

SEPTEMBER 2019

Approval of the thesis:

**GRID IMPEDANCE ESTIMATION BASED ADAPTIVE CONTROLLER
DESIGN FOR BACK-TO-BACK WIND TURBINE POWER CONVERTERS
FOR STABLE OPERATION IN DISTORTED AND WEAK GRID**

submitted by **HAKAN TEMİZ** in partial fulfillment of the requirements for the degree of **Master of Science in Electrical and Electronics Engineering Department, Middle East Technical University** by,

Prof. Dr. Halil Kalıpçılar
Dean, Graduate School of **Natural and Applied Sciences**

Prof. Dr. İlkay Ulusoy
Head of Department, **Electrical and Electronics Eng.**

Assist. Prof. Dr. Ozan Keysan
Supervisor, **Electrical and Electronics Eng., METU**

Dr. Erhan Demirok
Co-Supervisor, **Turbo Power Systems**

Examining Committee Members:

Assist. Prof. Dr. Emine Bostancı
Electrical and Electronics Eng., METU

Assist. Prof. Dr. Ozan Keysan
Electrical and Electronics Eng., METU

Assoc. Prof. Dr. Murat Göl
Electrical and Electronics Eng., METU

Assist. Prof. Dr. Emre Özkan
Electrical and Electronics Eng., METU

Assist. Prof. Dr. Taner Göktaş
Electrical-Electronics Eng. , İnönü Uni.

Date: 09.09.2019

I hereby declare that all information in this document has been obtained and presented in accordance with academic rules and ethical conduct. I also declare that, as required by these rules and conduct, I have fully cited and referenced all material and results that are not original to this work.

Name, Surname: Hakan Temiz

Signature:

ABSTRACT

GRID IMPEDANCE ESTIMATION BASED ADAPTIVE CONTROLLER DESIGN FOR BACK-TO-BACK WIND TURBINE POWER CONVERTERS FOR STABLE OPERATION IN DISTORTED AND WEAK GRID

Temiz, Hakan
Master of Science, Electrical and Electronics Engineering
Supervisor: Assist. Prof. Dr. Ozan Keysan
Co-Supervisor: Dr. Erhan Demirok

September 2019, 131 pages

This thesis involves grid impedance estimation based adaptive controller design for back-to-back wind turbine power converters for stable operation in distorted and weak grid. The study focuses on the low frequency harmonic elimination of injected current to the grid under distorted grid conditions and maintaining system stability under wide range of grid impedance values for Voltage Source Inverters (VSIs) connected to the grid via *LCL* filter. To eliminate 5th and 7th harmonics of the injected current, a current controller with harmonic compensator is developed on the grid side controller. The system stability is evaluated by means of several control methods and ensured by adjusting the parameters of Phase Locked Loop (PLL) based on real-time estimated grid impedance. The control design is analyzed by detailed computer simulations. Obtained results are verified by laboratory experiments with a 300 kW wind turbine system which consists of squirrel cage induction generator, IGBT based back-to-back converter and *LCL* filter. Different operating conditions are considered to provide a through performance evaluation of the designed system.

Keywords: grid-connected inverter, adaptive control, weak grid, distorted grid, PRBS injection

ÖZ

SIRT SIRTA RÜZGAR TÜRBİNİ GÜÇ ÇEVİRİCİLERİNİN BOZUK VE ZAYIF ŞEBEKEDA DENGELİ ÇALIŞTIRILABİLMESİ İÇİN ŞEBEKE EMPEDANSI TAHMİNİNE DAYALI UYARLAMALI KONTROLCÜ TASARIMI

Temiz, Hakan
Yüksek Lisans, Elektrik ve Elektronik Mühendisliği
Tez Danışmanı: Dr. Öğr. Üyesi Ozan Keysan
Ortak Tez Danışmanı: Dr. Erhan Demirok

Eylül 2019, 131 sayfa

Bu tez, sırt sırta rüzgar türbini güç çeviricilerinin bozuk ve zayıf şebeke koşulları altında dengeli çalıştırılabilmesi için şebeke empedansı tahminine dayalı uyarlamalı kontrolcü tasarımı içermektedir. Bu çalışma, şebekeye LCL filtreye bağlı gerilim kaynaklı eviriciler için zayıf şebeke koşulları altında şebekeye basılan akımın düşük frekans harmoniklerini gidermeye ve geniş şebeke empedansı aralığında sistem dengesini sürdürmeye odaklanmaktadır. Şebekeye basılan akımın 5. ve 7. harmoniklerini gidermek için şebeke tarafı kontrolcüsünde harmonik gidericili akım kontrolcüsü geliştirilmiştir. Sistem kararlılığı çeşitli kontrol yöntemleriyle değerlendirilir ve gerçek zamanlı şebeke empedansı tahminine dayanarak faz kilitlemeli döngü parametrelerinin ayarlanmasıyla sağlanır. Tasarım çalışmaları, ayrıntılı bilgisayar benzetimleri aracılığıyla analiz edilmektedir. Elde edilen sonuçlar sincap kafesli asenkron generatör, IGBT tabanlı sırt sırta çevirici ve LCL filtre içeren 300 kW güç değerli bir rüzgar türbini sisteminde laboratuvar deneyleriyle doğrulanmaktadır. Bu çalışmada, tasarımı yapılan sistemin tamamıyla eksiksiz ve kapsamlı bir başarımlı değerlendirilmesini sunabilmek amacıyla farklı çalışma koşulları göz önünde bulundurulmaktadır.

Anahtar Kelimeler: Şebekeye bađlı evirici, uyarlamalı kontrol, zayıf şebeke, bozuk şebeke, PRBS enjeksiyonu

To my beloved wife Pakize and my family

ACKNOWLEDGEMENTS

I would like to thank my supervisors, Assist. Prof. Dr. Ozan Keysan and Dr. Erhan Demirok for their support, encouragement, guidance and critiques on this study throughout my graduate education.

I would like to express my sincere gratitude to my beloved wife Pakize for her endless love, support, patience and encouragements in all aspects of my life.

I express my deepest gratitude to my brother and parents for their support and patience throughout my life.

I would like to acknowledge thanks to my collages Ali Türkay, Serhat Emir Ogan and Burak Çetinkaya for their help and support.

I would like to thank to ASELSAN Inc. for its valuable support throughout my graduate studies. Outstanding laboratory and component resources have benefited my work greatly.

I wish to thank to Middle East Technical University Department of Electrical and Electronics Engineering faculty and staff for their help throughout my graduate studies.

TABLE OF CONTENTS

ABSTRACT	v
ÖZ.....	vii
ACKNOWLEDGEMENTS	x
TABLE OF CONTENTS	xi
LIST OF TABLES	xv
LIST OF FIGURES	xvi
LIST OF ABBREVIATIONS	xxi
LIST OF SYMBOLS	xxiii
CHAPTERS	
1. INTRODUCTION	1
1.1. Background and Motivation	2
1.2. Scope of the Thesis.....	3
1.3. Main Contributions.....	5
1.4. Outline of the Thesis	10
2. SYSTEM DESCRIPTION.....	11
2.1. Grid Code Overview	15
2.1.1. Fault Ride Through Capability	15
2.1.2. Active Power Control	17
2.1.3. Reactive Power Control	17
2.1.4. Power Quality	19
2.2. Back to Back Converter Design	20
2.3. Generator Side Control.....	21

2.3.1. Squirrel Cage Induction Machine Model	22
2.3.2. Rotor Flux Oriented Control	23
2.3.3. SCIG Control.....	24
2.4. Grid Side Control	25
2.4.1. Synchronous Reference Frame Control	26
2.4.2. Stationary Reference Frame Control	27
2.4.3. Natural Frame Control.....	27
2.5. PWM Modulation	28
2.6. Summary	32
3. GRID SIDE CONTROLLER AND LCL FILTER	33
3.1. LCL Filter	35
3.2. DC Link Voltage Controller	44
3.3. Current Controller	45
3.4. Harmonic Compensation.....	52
3.5. Phase Locked Loop.....	55
3.6. Summary	60
4. IMPEDANCE BASED STABILITY ANALYSIS	61
4.1. Impedance Based Stability Criterion	61
4.2. Analytical Inverter Model.....	63
4.2.1. Small Signal Model	64
4.2.2. Controller Transfer Functions	67
4.3. Inverter Output Impedance	68
4.3.1. Impedance d Component	69
4.3.2. Impedance q Component	71

4.4. Grid Impedance	73
4.4.1. Pseudo Random Binary Sequence Injection.....	73
4.4.2. Estimation of Grid Impedance.....	77
4.5. Analysis of the System under Weak Grid Conditions.....	78
4.5.1. Impedance d Component Stability.....	78
4.5.2. Impedance q Component Stability.....	80
4.6. Stability Analysis with the Nonlinear Simulation Model	83
4.7. Summary	88
5. EXPERIMENTAL RESULTS	89
5.1. Harmonic Compensation under Distorted Grid Condition.....	92
5.1.1. 5th Harmonic Compensation.....	93
5.1.2. 7th Harmonic Compensation.....	94
5.2. Estimation of Grid Inductance.....	96
5.2.1. Grid Current Distortions Caused by MLBS Signal	96
5.2.2. Accuracy of the Estimated Grid Inductance	99
5.3. Sudden Grid Inductance Change.....	101
5.4. Adaptive Control	104
5.5. Operation under Stiff and Weak Grid Conditions.....	111
5.6. Summary	117
6. CONCLUSIONS	119
6.1. Summary	119
6.2. Contributions to the Field.....	120
6.3. Future Work	121
REFERENCES.....	123

APPENDICES.....	131
A. Transformations Between <i>abc</i> , <i>αβ</i> and <i>dq</i> Reference Frames.....	131

LIST OF TABLES

TABLES

Table 2.1. Capabilities of Wind Power Concepts [7].....	14
Table 2.2. Switching States and Corresponding Output Voltages	30
Table 2.3. Working Sequence of the Basic Vectors for Each Sector.....	30
Table 3.1. System Parameters	38
Table 3.2. Current Distortion Limits Determined by IEEE 519-2014 [50]	52
Table 4.1. Truth Table of Exclusive OR (XOR) Function.....	74
Table 4.2. State of Each Shift Register While Generating the 7 bits MLBS Signal ..	75
Table 5.1. System Parameters of the Experimental Setup	92
Table 5.2. THD Values of Grid Currents for without and with 5 th Harmonic Compensation.....	94
Table 5.3. THD Values of Grid Currents for without and with 7 th Harmonic Compensation.....	94
Table 5.4. THD Values for without and with MLBS Signal under Stiff and Weak Grid Conditions	96
Table 5.5. Current References for the Given Regions in Following Figures.....	111

LIST OF FIGURES

FIGURES

Figure 1.1. The Share of Renewable Energy Resources in Europe Electricity Generation.....	1
Figure 1.2. Nonlinear Simulation Model in MATLAB/Simulink	7
Figure 1.3. Controller of the Inverter.....	8
Figure 1.4. Experimental Setup	9
Figure 2.1. Power Conversion in a Wind Turbine [6]	11
Figure 2.2. Technological Roadmap for Wind Turbine’s Technology [7].....	12
Figure 2.3. Wind Turbine Concepts: Fixed Speed Wind Turbine (Type A), Partial Variable Speed Wind Turbine (Type B), Variable Speed Wind Turbine with Partial-Scale Converter (Type C) and Variable Speed Wind Turbine with Full-Scale Power Converter (Type D) [7].....	13
Figure 2.4. Fault Ride Through Requirements Determined by TWTNR [10]	16
Figure 2.5. Active Power Control Requirements Determined by TWTNR [10].....	17
Figure 2.6. Reactive Power Control Requirements Determined by TWTNR [10] ...	18
Figure 2.7. Reactive Power against Utility Voltage Requirements Determined by TWTNR [10]	18
Figure 2.8. Reactive Power Support Requirements Determined by TWTNR [10]...	19
Figure 2.9. Harmonic Standards for Grid Integration of WECS [5]	20
Figure 2.10. Control Scheme of a WECS [14]	21
Figure 2.11. A variable speed wind turbine with a full scale power converter and SCIG [17].....	22
Figure 2.12. Complex Vector Equivalent Circuit of Induction Machines [18].....	22
Figure 2.13. Control Scheme of Generator Side Converter [17].....	24
Figure 2.14. General Structure of Synchronous Reference Frame Control [22].....	26
Figure 2.15. General Structure of Stationary Reference Frame Control [22]	27

Figure 2.16. General Structure of Natural Frame Control [22].....	28
Figure 2.17. The Structure of Two Level Three Phase Inverters [38]	29
Figure 2.18. Voltage Vector, Vector Summation Method and PWM Waveforms in Six Sectors [39]	31
Figure 3.1. The Scope of the Thesis [40].....	33
Figure 3.2. Control Scheme of the Grid Side Converter	34
Figure 3.3. Per Phase Equivalent Circuits of Undamped (a), Series R Damped (b) and Shunt R-C Damped (c) LCL Filters	35
Figure 3.4. Measured Frequency Responses of Undamped and Damped LCL Filters	40
Figure 3.5. Pole Zero Maps of Series R (a) and Shunt R-C (b) Damped LCL Filters for Various R_d	42
Figure 3.6. Grid Voltage (a) and Current Waveforms for Undamped (b) and Shunt R-C damped (c) LCL Filters	43
Figure 3.7. Outer DC Link Voltage Loop	44
Figure 3.8. The Current Control Loop of Grid Connected Inverter.....	45
Figure 3.9. Closed Loop Current Control with Plant.....	46
Figure 3.10. Double Update PWM Method [40]	47
Figure 3.11. Bode Plot of Open Loop PR+HC Current Control System Under Varying K_p	49
Figure 3.12. Root Locus Plots of Undamped LCL Filter with CCF (a) and GCF (b), Series R Damped LCL Filter with CCF (c) and GCF (d), Shunt R-C Damped LCL Filter with CCF (e) and GCF (f)	50
Figure 3.13. Grid Currents at Stability Limits	51
Figure 3.14. Grid Voltage (a), Grid Currents without (b) and with (c) HC, FFT Analysis of Grid Currents without (d) and with (e) HC.....	54
Figure 3.15. Block Diagram of a Basic PLL [60]	55
Figure 3.16. Structure of DSOGI-PLL [61]	56
Figure 3.17. Structure of the SOGI [60]	56

Figure 3.18. Step Response of the PLL System with Damping Factors ζ from 0.5 to 1	59
Figure 3.19. Bode Plots of the PLL System with Settling Times T_s from 0.1 to 0.5	59
Figure 4.1. Equivalent Circuit of the Grid Connected Inverter System [69]	62
Figure 4.2. Grid Connected Three-Phase Voltage Source Inverter System	64
Figure 4.3. Block Diagram of the SRF-PLL [69]	68
Figure 4.4. The d Component Open Loop Transfer Functions with Current Control [69]	69
Figure 4.5. The d Component Closed Loop Transfer Functions with DC Voltage Control [69]	70
Figure 4.6. The q Component Open Loop Transfer Functions with Current Control and PLL [69]	72
Figure 4.7. 7-bits Shift Register with XOR Feedback for MLBS Generation	74
Figure 4.8. Generated 7 bits MLBS Signal	75
Figure 4.9. Power Spectrum of 7-bits MLBS Signal Generated at 10 kHz	76
Figure 4.10. Estimation of Grid Inductance	77
Figure 4.11. Frequency Responses of Inverter Output Impedance d Component and Grid Impedance	79
Figure 4.12. Ratio of Impedance d Components $Z_g/Z_s - d$ on the Complex Plane	80
Figure 4.13. Frequency Responses of Inverter Output Impedance q Component and Grid Impedance	81
Figure 4.14. Ratio of Impedance q Components $Z_g/Z_s - q$ on the Complex Plane under Stiff Grid	82
Figure 4.15. Ratio of Impedance q Components $Z_g/Z_s - q$ on the Complex Plane under Weak Grid	83
Figure 4.16. PCC Voltage (a), Injected Grid Current (b), Estimated Frequency (c), Active (d) and Reactive (e) Power at Sudden Grid Inductance Change with $T_s = 0.1$ s	85

Figure 4.17. PCC Voltage (a), Injected Grid Current (b), Estimated Frequency (c), Active (d) and Reactive (e) Power at Sudden Grid Inductance Change with $T_s = 0.3$ s	87
Figure 5.1. Block Diagram of the Experimental Setup	89
Figure 5.2. Experimental Setup	90
Figure 5.3. Inductor Block with a Circuit Breaker	91
Figure 5.4. DC Link Voltage (CH1), PCC Voltage (CH2), Grid Current (CH3) and FFT of Grid Current (Math) without (a) and with (b) 5th Harmonic Compensator	93
Figure 5.5. DC Link Voltage (CH1), PCC Voltage (CH2), Grid Current (CH3) and FFT of Grid Current (Math) without (a) and with (b) 7th Harmonic Compensator	95
Figure 5.6. DC Link Voltage (CH1), PCC Voltage (CH2), Grid Current (CH3) and FFT of Grid Current (Math) without (a) and with (b) MLBS Signal under Stiff Grid	97
Figure 5.7. DC Link Voltage (CH1), PCC Voltage (CH2), Grid Current (CH3) and FFT of Grid Current (Math) without (a) and with (b) MLBS Signal under Weak Grid	98
Figure 5.8. Estimated Grid Inductance Value under Stiff (a) and Weak (b) Grid Conditions	100
Figure 5.9. The Transient of the Averaged Estimated Inductance from 0.3 to 3 mH	100
Figure 5.10. The Change of DC Link Voltage (CH1,a), PCC Voltage (CH2,a), Injected Grid Current (CH3,a) and Estimated Frequency (b) at Sudden Grid Inductance Change with $T_s = 0.1$	102
Figure 5.11. The Change of DC Link Voltage (CH1,a), PCC Voltage (CH2,a), Injected Grid Current (CH3,a) and Estimated Frequency (b) at Sudden Grid Inductance Change with $T_s = 0.3$	103
Figure 5.12. DC Link Voltage (CH1,a), PCC Voltage (CH2,a), Grid Current (CH3,a), PLL Settling Time (b), Estimated Grid Inductance (c) and Frequency (d) when Grid Inductance is suddenly changed from 0.3 to 3mH	106

Figure 5.13. DC Link Voltage (CH1,a), PCC Voltage (CH2,a), Grid Current (CH3,a), PLL Settling Time (b), Estimated Grid Inductance (c) and Frequency (d) with Improved Method when Grid Inductance is changed from 0.3 to 3mH 108

Figure 5.14. DC Link Voltage (CH1,a), PCC Voltage (CH2,a), Grid Current (CH3,a), PLL Settling Time (b), Estimated Grid Inductance (c) and Frequency (d) with Improved Method when Grid Inductance is changed from 3 to 0.3mH 110

Figure 5.15. DC Link Voltage (CH1), PCC Voltage (CH2), Grid Current (CH3) under Stiff (a) and Weak (b) Grid Conditions 112

Figure 5.16. PCC Voltage (a), Grid Current (b), Injected Power (c), Power Factor (d) and THD of the Injected Grid Current under Stiff Grid Conditions..... 114

Figure 5.17. PCC Voltage (a), Grid Current (b), Injected Power (c), Power Factor (d) and THD of the Injected Grid Current under Weak Grid Conditions 116

LIST OF ABBREVIATIONS

AC	Alternating Current
CAN	Controller Area Network
CCF	Converter Current Feedback
DC	Direct Current
DDSRF	Decoupled Double Synchronous Reference Frame
DFIG	Double Fed Induction Generator
DSOGI	Double Second Order Generalized Integrator
DTC	Direct Torque Control
EPLL	Enhanced Phase Locked Loop
FFT	Fast Fourier Transform
FOC	Field Oriented Control
GCF	Grid Current Feedback
HC	Harmonic Compensator
ICU	Inverter Control Unit
IGBT	Integrated Gate Bipolar Transistor
MLBS	Maximum Length Binary Sequence
PCC	Point of Common Coupling
PD	Passive Damping
PI	Proportional Integral
PLL	Phase Locked Loop
PMSG	Permanent Magnet Synchronous Generator
PRBS	Pseudo-Random Binary Sequence
PR	Proportional Resonant
PWM	Pulse Width Modulation
QSG	Quadrature Signal Generation
RHP	Right Hand Plane
RMS	Root Mean Square
SCIG	Squirrel Cage Induction Generator

SCR	Short Circuit Ratio
SOGI	Second Order Generalized Integrator
SRF	Synchronous Reference Frame
SVPWM	Space Vector Pulse Width Modulation
TDD	Total Demand Distortion
THD	Total Harmonic Distortion
TSO	Transmission System Operator
TWTNR	Turkish Wind Turbine Network Regulations
UPS	Uninterruptible Power Supplies
VOC	Voltage Oriented Control
VSI	Voltage Source Inverters
WECS	Wind Energy Conversion System
WRIG	Wound Rotor Induction Generator
WRSG	Wound Rotor Senkron Generator
XOR	Exclusive OR

LIST OF SYMBOLS

SYMBOLS

a	Amplitude of MLBS
A	Current-to-current transfer function
C_{DC}	DC Link capacitance
C_d	Damping capacitance
C_f	Filter capacitance
d	Duty ratio
D	Steady-state of the duty ratio
f_g	Grid frequency
f_{gen}	Generating frequency
f_{res}	Resonance frequency
f_{samp}	Sampling frequency
f_{sw}	Switching frequency
G	System transfer function
G_{PI}	PI controller transfer function
$G(\omega)$	Frequency domain grid impedance
i	Current
I	Steady-state of the current
i_g	Grid current
i_{in}	Input current
I_L	Demand load current
i_{R_n}	Damping resistor current at n^{th} harmonic frequency
i_s	Source current
I_S	Steady-state of source current
I_{SC}	Short-circuit current

j	Imaginary component
J	Moment of inertia
k_a	Current ripple on the inverter side inductor
K_p	Proportional gain
K_i	Integral gain
L	Inductance
L_1	Inverter side inductance
L_2	Grid side inductance
L_{ext}	Extra inductance
L_{in}	DC-voltage control loop gain
L_{iso}	Isolation transformer inductance
L_{out}	Current control loop gain
L_{PLL}	PLL loop gain
L_T	Total inductance
n	Number of shift register
N	MLBS length
p	d/dt
P	Number of excitation periods
pp	Number of pole pairs
P_{loss}	Power loss of damping resistors
P_n	Rated active power
r	Resistance
R_d	Damping resistance
s	Laplace variable
S_n	Nominal power
T	Voltage-to-voltage transfer function
T_e	Electromechanical torque
t_{meas}	Measurement time
T_s	Settling time

T_{samp}	Sampling time
T_{sw}	Switching period
U_s	Target voltage vector
v	Voltage
V	Steady-state of the voltage
V_{DC}	DC link voltage
V_g	Grid voltage
v_{in}	Input voltage
$x(t)$	Injected current signal
$X(\omega)$	Frequency domain excitation signal
Y	Admittance
Y_c	Filter capacitor branch admittance
$y(t)$	System voltage response
$Y(\omega)$	Frequency domain response signal
Z	Impedance
Z_g	Grid impedance
Z_o	Inverter output impedance
Z_s	Source impedance
ζ	Damping factor
δ	Harmonic attenuation
θ	Angle
ω	Angular mechanical speed
Φ_{MLBS}	Power spectrum of MLBS
ψ	Phase margin
λ	Magnetic flux
Δi	Current ripple
Δt	Clock pulse interval

UPPER INDEX

x^*	Reference value
x'	Sensed value
\hat{x}	Averaged value
x^t	Transpose
\vec{x}	Space vector

LOWER INDEX

x_c	Control based
x_{-cl}	Closed loop
x_d	D component
x_{-dc}	Variable based on DC link
x_i	Input
x_{in}	Input of the inverter
x_{max}	Maximum value
x_{min}	Minimum value
x_o	Output
x_{-o}	Open loop
x_{-pll}	Variable based on PLL
x_q	Q component
x_r	Variable based on rotor
x_s	Variable based on stator
x_{sr}	Variable based on magnetization
x_α	α component
x_β	β component

CHAPTER 1

INTRODUCTION

The share of renewable power generation systems such as wind and solar systems in energy generation is increasing day by day because renewable energy resources are environment friendly and have infinite supply capacity. Recent results given in Figure 1.1 from Agora Energiewende shows that in 2018, 32.3% of the Europe's electricity consumption is provided by renewable energy resources [1]. If the hydro power plants are excluded, the energy generated by solar, wind and biomass systems forms 22% of the whole energy generation. The share of wind and solar power generation increase every year from 2010 to 2018 and reach 12% and 4% of the generated energy in Europe respectively. For the grid integration of renewable power generation systems, most commonly power electronics based Voltage Source Inverters (VSIs) are used. The increase in the amount of power electronics based components connected to the grid brings some changes about grid dynamics, power quality and stability issues.

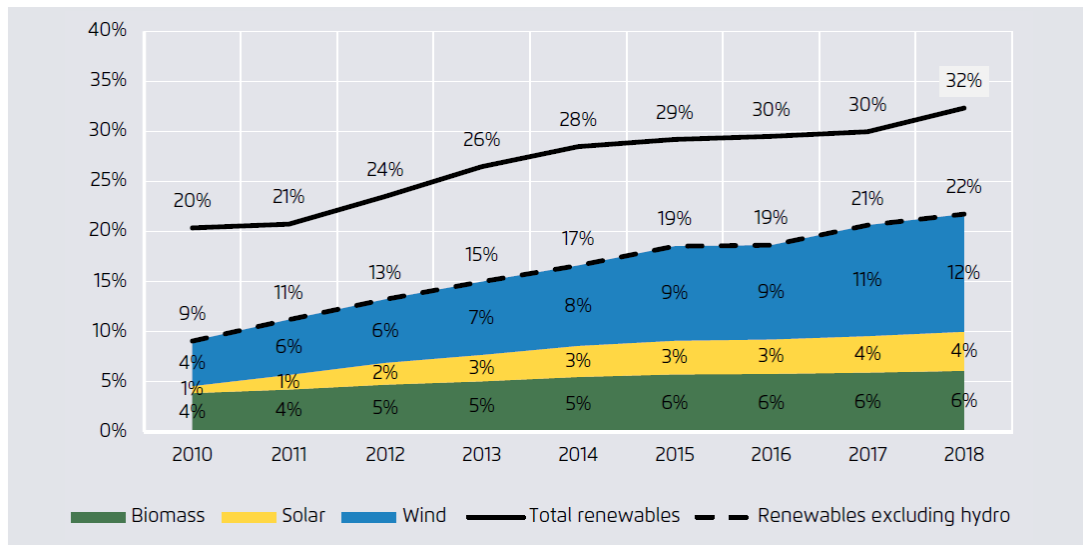


Figure 1.1. The Share of Renewable Energy Resources in Europe Electricity Generation

1.1. Background and Motivation

The performance of VSIs are dependent on the grid conditions at the Point of Common Coupling (PCC). When the voltage of the PCC includes low frequency harmonic contents like 3th, 5th or 7th harmonics, the grid injected current can contain these harmonics also. In addition to voltage distortions, the impedance of the grid has an impact on the stability of the grid connected inverter system. Unstable operations of the system can cause high amount of grid currents and so undesired tripping of safety devices can be observed.

When the grid impedance is relatively high, the grid is considered as weak. The weakness of a grid is evaluated by Short Circuit Ratio (SCR) which is defined in terms of line to line rms grid voltage V_g , grid impedance Z_g and nominal inverter power P_n as in Eq. (1.1). A grid is typically considered as weak when $SCR < 3$ [2].

$$SCR = \frac{V_g^2}{Z_g P_n} \quad (1.1)$$

Weak grids are generally observed in remote or rural areas powered through long feeder lines. When wind or solar power generation systems are located in remote areas, overextended medium voltage transmission lines are used and large inductive grid impedances appear. In addition to overextended lines, low power rating transformers contribute to inductive grid impedance. Increased penetration of wind or solar power generation systems in a distribution network or microgrid causes lower system inertia and the grid becomes more sensitive against sudden changes [3].

In order to provide stable operation under weak grid conditions, several solutions are presented in [4] using a small signal state-space model in the synchronously rotating dq reference frame. First one is that when the grid side inductance is increased stable operation is provided but additional voltage drop occurs on the inductor and utilization of a larger inverter unit can be required. Increasing damping resistance of the LCL filter is another solution with the cost of more power loss. Increasing control delay is also has a positive impact on system stability but the system response deteriorates in

transient conditions. In addition to these solutions, decreasing controller gain parameters is offered but decreased proportional gains cause slower dynamic response. Therefore, redesigning the system parameters of the VSIs for stable operation under weak grid conditions brings some costs. Besides that grid is a dynamic system and its parameters are changing continuously. At the end, the necessity of an automated system which adapt its parameters based on instantaneous grid conditions is seen.

1.2. Scope of the Thesis

In this study, real time grid impedance estimation based adaptive controller design is discussed, which provides a stable operation to VSIs under both stiff and weak grids. This method presents a control system which updates its controller parameters according to real time grid impedance measurements. For grid impedance measurement, an excitation signal called as Pseudo Random Binary Sequence (PRBS) is injected to the grid with current and its voltage response is measured. The PRBS is a signal easy to generate and includes harmonic contents at a wide frequency range. This provides estimation of grid impedance in a broad range. To estimate the grid inductance, measured voltage and current signal are transformed to frequency domain by using Fast Fourier Transform (FFT). By dividing voltage and current at the PCC, the impedance of the grid is estimated. The inductance of the grid is generated by using magnitude and phase response of the impedance.

By considering stiff grid conditions, a cascaded controller is designed for grid connected VSI system. A current controller is used to control the injected grid current. Active and reactive components of the injected grid current is controlled separately. Injected reactive current is determined to compensate the reactive power drawn by the capacitor block of the LCL filter and so unity power factor is satisfied at the PCC. Injected active current is determined by an outer DC voltage control loop. Generation side of the renewable energy power system is modeled as a current source which charges the DC link capacitors. DC voltage control loop tries to keep the DC link

voltage constant. A Phase Locked Loop (PLL) block is used to extract the phase and frequency information of the grid voltage at the PCC. The generated phase information is used for synchronization of injected current to the voltage signal. Also, an LCL filter is designed to attenuate the high frequency contents of the voltage and current signals caused by the Pulse Width Modulation (PWM) switching.

The current controller parameters are determined by applying root locus analysis to the system by considering series R and shunt R-C passive damping methods with converter and grid current feedbacks. Double Second Order Generalized Integrator (DSOGI) PLL is used to synchronize with the grid because DSOGI-PLL provide less oscillations during transients thanks to its extra filtering feature.

The filtering performance of the PLL has an extensive impact on the operation of system under different grid conditions. PLL with a small control bandwidth provides stable operation under weak grid conditions but dynamic response of the system becomes slower. In this study, a system which provides fast response under stiff grid and stable operation under weak grid, is designed by adaptively changing PLL parameters.

The impedance based stability analysis presented in [5] is used for the stability analysis of the overall system. This method is mainly focuses on the impedance interactions between the grid and inverter. By using small signal model of the inverter an output impedance model is derived. The impedance of the grid is estimated by measuring the injected grid current and voltage. Nyquist and Bode stability criterions are considered to determine the stability limit under stiff and weak grid conditions. Based on analyses, controller parameters of the PLL is adaptively updated according to estimated grid impedance during the operation.

A control system is designed in MATLAB/Simulink environment and operation of the system is analyzed. The required c-code for the microprocessor used in experimental setup is automatically generated from the model in MATLAB/Simulink by using

embedded coder tool. While doing experiments sudden inductance changes are performed in order to simulate weak grid conditions.

1.3. Main Contributions

Contributions of the thesis are listed in the order they appear in the study.

- Step-by-step design procedure for LCL filters is given by considering most commonly used two passive damping methods. Selections of the passive component values are explained in detail by considering power losses and stability of the system. Pole zero maps of the designed filters are plotted for series R and shunt R-C damped LCL filters with converter and grid current feedbacks. The optimum values of damping resistances are determined based on the place of high frequency poles on the unity circles.
- Current controller gain parameters are determined based on the root locus plot of the plant by considering the PWM and control delays and LCL filter transfer functions. Open loop transfer function of the plant is derived and discretized by the sampling time of the controller. By using discrete transfer function, root locus plots are drawn and maximum values of gain parameters are determined for both damping types and current feedback methods.
- Design of DSOGI-PLL structure is explained for weak and stiff grid conditions. Proportional gain parameters of the loop filter are determined based on the damping ratio, settling time and natural frequency. The relation between settling time and bandwidth of the PLL is given and two different PLLs are proposed for weak and stiff grid conditions.
- Impedance based stability analysis is performed based on Bode plots and Nyquist stability criterion by evaluating grid and output inverter impedances. The inverter output impedance is derived based on small signal model of the inverter at a certain steady state operating point. PRBS injection method is proposed in order to estimate grid impedance in real time.

- The nonlinear simulation model given by Figure 1.2 is prepared in MATLAB/Simulink environment and used in different parts of the thesis. The controller of the inverter given by Figure 1.3 is designed in discrete domain and used to generate the required c-codes for the microprocessor. The model contains a two level VSI which is connected between DC and AC voltage sources. For the simulations, DC voltage loop is omitted and only inner current control loop is considered for stability analysis because it has faster dynamic response than outer voltage loop. Shunt R-C damped LCL filter provides an interface between VSI and grid which is represented by AC voltage source. Proportional Resonant + Harmonic Compensator (PR+HC) current controller is performed in $\alpha\beta$ reference frame to set the injected active and reactive power. The designed DSOGI-PLL is used in order to synchronize with the grid. PRBS injection block is added to estimate the grid inductance.

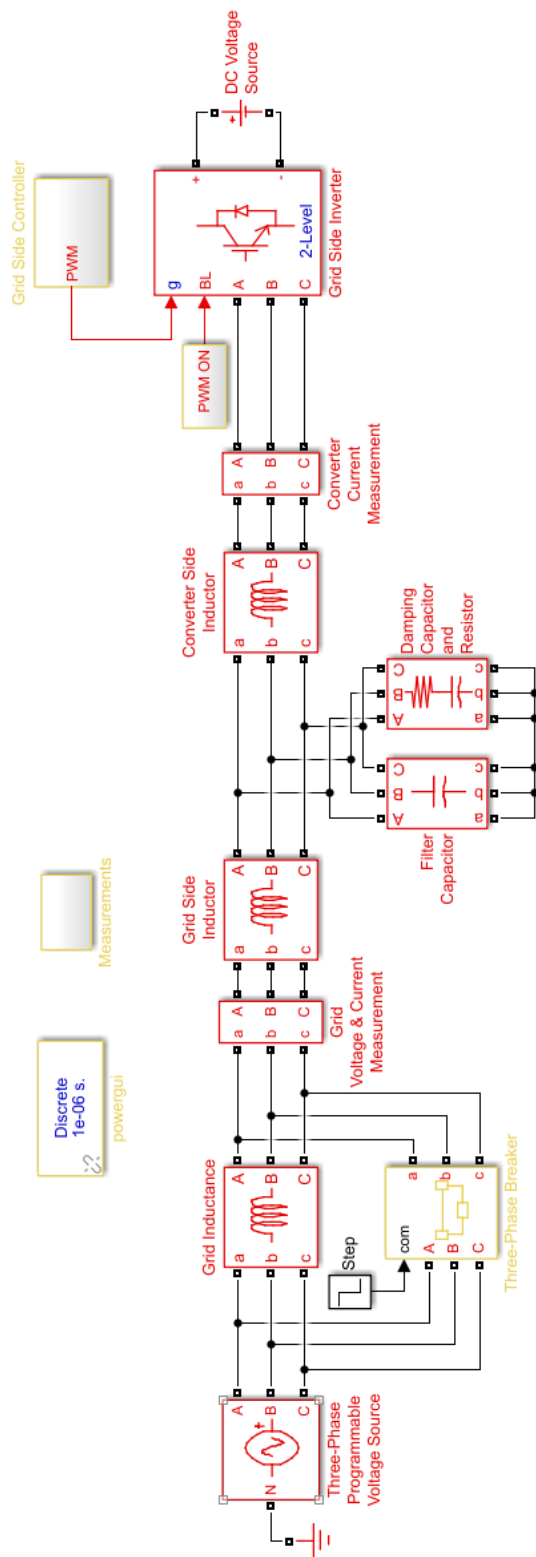


Figure 1.2. Nonlinear Simulation Model in MATLAB/Simulink

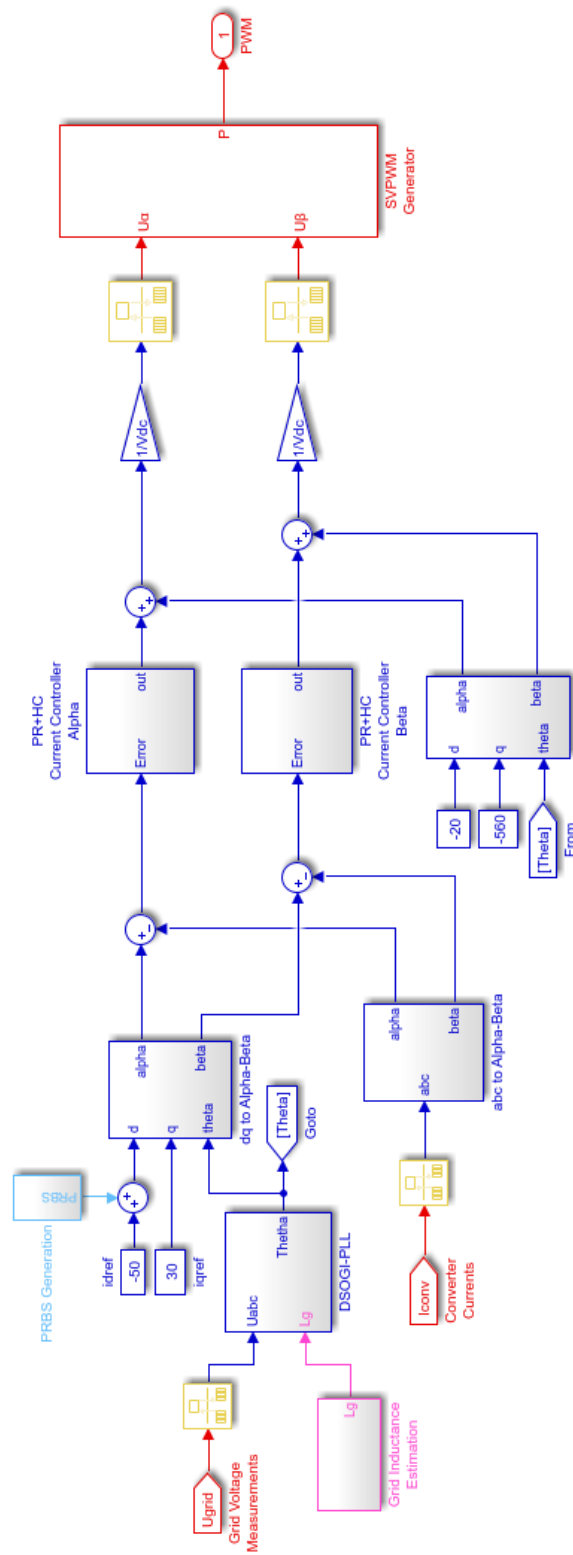


Figure 1.3. Controller of the Inverter

- The experimental setup given in Figure 1.4 is used in order to verify the obtained analytical and simulation results.

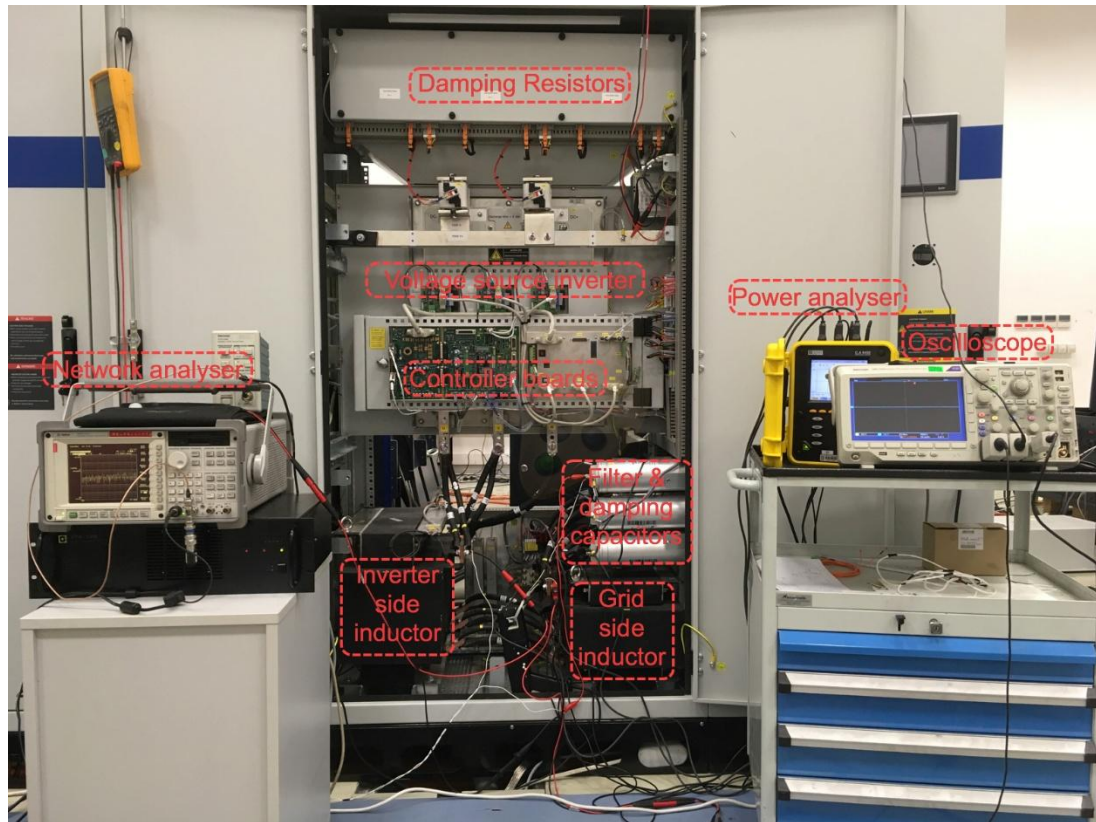


Figure 1.4. Experimental Setup

The setup is composed of the grid side of a 300 kW back-to-back wind turbine converter. The designed adaptive controller is implemented with the given setup. Power analyzer and oscilloscope are used to analyze the injected grid current and grid voltage. Frequency response of the LCL filter is measured by using network analyzer. The simulated control loop is converted to c-codes by using the embedded code generation toolbox of the Simulink. Parallel connected circuit breaker and inductor block is used to model the weak and stiff grid conditions. The details of the setup and circuit parameters are given in Chapter 5.

1.4. Outline of the Thesis

In Chapter 1, a brief introduction about the thesis is presented by considering background, motivation, contributions and scope of the thesis.

In Chapter 2, the overall system description of a variable speed wind turbine with a full scale power converter is introduced. Grid code requirements determined by Turkish Wind Turbine Network Regulations (TWTNR) and international standards are mentioned. Power and control structure of back-to-back converter are given in different reference frames by dividing into two parts as generator and grid side inverters. At the end, the modulation of inverters are investigated in detail.

In Chapter 3, the main topics are controller design of grid side converter and LCL filter design. Firstly, step-by-step LCL filter design procedure is given by considering series R and shunt R-C passive damping methods. After that, outer DC link voltage controller and inner current controller design are presented. The gain parameters of the current controller are determined by applying Root Locus analysis to the system. The relation between harmonic compensation and proportional gain is analyzed. Lastly, a robust PLL design for stiff and weak grid conditions is explained.

In Chapter 4, impedance based stability analysis is performed by considering whole system. The criterion for the stability is presented and analytical small signal model of the inverter is derived. Inverter output impedance required for stability analysis is calculated by using derived equations. Grid impedance estimation method by using PRBS signal injection is explained and stability analysis is performed for different grid conditions. The obtained results are verified by nonlinear simulation models.

In Chapter 5, obtained analytical results are verified by the experiments. Performances of harmonic compensation and adaptive controller are investigated in detail. Different operating conditions are considered for the experiments.

In Chapter 6, summary, contributions and future works of the study are given.

CHAPTER 2

SYSTEM DESCRIPTION

Power conversion in a wind turbine can be seen in Figure 2.1. Kinetic power of the wind is captured by means of turbine blades and converted to mechanical power. Rated rotational speed of multi-MW wind turbines is generally around 10-15 *rpm*. To convert low-speed, high-torque power to high-speed, low-torque power, gearboxes are used commonly. Mechanical to electrical power conversion is performed by the help of generators.

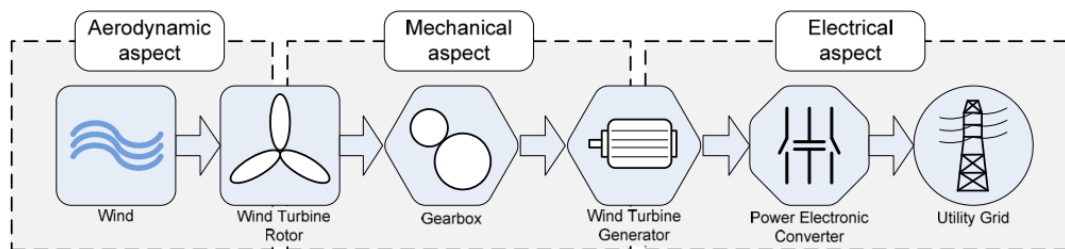


Figure 2.1. Power Conversion in a Wind Turbine [6]

Generators with high number of poles are used to eliminate the gearboxes but such special machines are generally expensive and heavy. A power converter is used as interface to the grid in modern systems. There are many possible technical solutions of converting wind power to the electrical power and a technological roadmap is given in Figure 2.2.

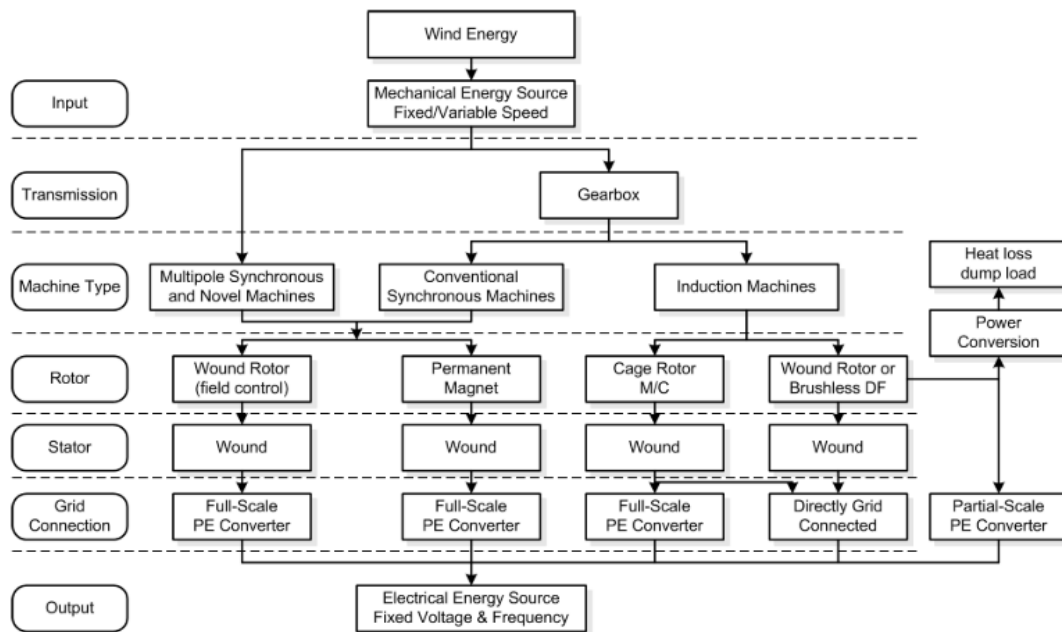


Figure 2.2. Technological Roadmap for Wind Turbine's Technology [7]

Aim of the design of variable speed wind turbines is to achieve maximum aerodynamic efficiency over a wide range of wind speed. In variable speed operation, wind speed fluctuations are absorbed by the change of generator speed. Thus, stress on the mechanical components such as gearbox and shaft is reduced. Also, captured power by the turbine is increased and acoustical noise is reduced. Besides that, the use of power converters provides control of injected active and reactive power which means frequency and voltage control. Additionally, thanks to the power converter, wind turbine may give quick response under transient and dynamic power system situations. Power converters have positive impact on network stability and improve power quality by reducing flicker level, filtering out low order harmonics and limiting in-rush and short circuit currents. As a price of all these advantages, power converters bring extra power losses on semiconductor devices and filtering components, cause some reliability issues and increase capital cost due to more electrical components [8].

Based on the speed control and power conversion criteria, wind turbines are classified into four groups as seen in Figure 2.3: fixed speed wind turbine, partial variable speed

wind turbine, variable speed wind turbine with partial-scale converter and variable speed wind turbine with full-scale power converter [7].

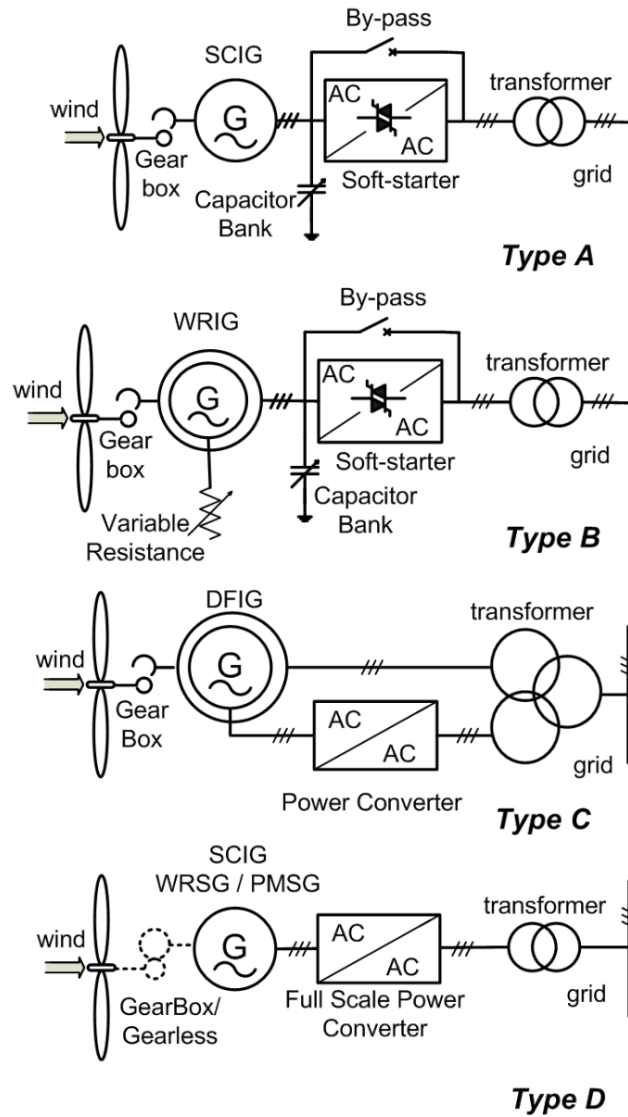


Figure 2.3. Wind Turbine Concepts: Fixed Speed Wind Turbine (Type A), Partial Variable Speed Wind Turbine (Type B), Variable Speed Wind Turbine with Partial-Scale Converter (Type C) and Variable Speed Wind Turbine with Full-Scale Power Converter (Type D) [7]

Wind turbine concepts are compared in Table 2.1 in terms of technical performances such as: grid control, cost, maintenance, internal turbine performances, voltage control, reactive power control and fault ride through capabilities.

Table 2.1. *Capabilities of Wind Power Concepts* [7]

System	Type A	Type B	Type C	Type D
Variable speed	No	No	Yes	Yes
Control active power	Limited	Limited	Yes	Yes
Control active power	No	No	Yes	Yes
Short circuit (fault-active)	No	No	No/Yes	Yes
Short circuit power	contribute	contribute	contribute	limit
Control bandwidth	1-10 s	100 ms	1 ms	0.5-1 ms
Standby function	No	No	Yes +	Yes ++
Flicker (sensitive)	Yes	Yes	No	No
Softstarter needed	Yes	Yes	No	No
Rolling capacity on grid	Yes, partly	Yes, partly	Yes	Yes
Reactive compensator (C)	Yes	Yes	No	No
Island operation	No	No	Yes/No	Yes
Investment	++	++	+	0
Maintenance	++	++	0	+

Type A wind turbines were widely used by Suzlon, Nordex, Siemens Bonus and Ecotènia in 80s. The concept is based on Squirrel Cage Induction Generator (SCIG). Its rotor is driven by turbine and its stator is directly connected to grid. Its rotation speed is fixed and can only vary between 1-2% [9].

Type B wind turbines were used by Vestas (V27, V34, V47) in 80s and 90s. The concept is based on Wound Rotor Induction Generator (WRIG). Thanks to electrical resistance of the rotor which is controlled by power electronics, the rotor and generator speed vary $\pm 10\%$ during wind gusts. By the expense of some energy losses, power quality is maximized and mechanical loading of turbine components is reduced [9].

Type C wind turbines are the most popular system and used by GE (1.5 series and 3.6), Repower, Vestas, Nordex, Gamesa, Ecotènia, Ingetur, Suzlon. The concept is based on WRIG. Its rotor is connected to the grid through a back-to-back voltage source converter and its stator is directly connected to the grid. Back-to-back converter

decouple the mechanical and electrical rotor frequency and thus match the grid and rotor frequency. Generally 40% of the rated power flows through the back-to-back converter and turbine speed can vary $\pm 40\%$ of the synchronous speed. The power electronics provides active and reactive power flows, active voltage control and fault ride through capabilities [9].

Type D wind turbines are used by Enercon, MEG (Multibrid M5000), GE (2.x series), Zephyros, Winwind, Siemens (2.3 MW), Made, Leitner, Mtorres and Jeumont. Various type of generators such as: Permanent Magnet Senkron Generator (PMSG), Wound Rotor Senkron Generator (WRSG) and SCIG may be used in this type of wind turbines and whose stators are connected to the grid through a full scale power converter. It provides a wider operation speed, reactive power and voltage control range than type C [9].

2.1. Grid Code Overview

In order to ensure that the wind farms do not adversely affect the power system operation in terms of security of supply, reliability and power quality, some specific requirements are being developed by system operators [9]. Requirements about active and reactive power control, fault ride through capability, power quality and grid support during network disturbances are determined by the Turkish Wind Turbine Network Regulations (TWTNR) [10]. The requirements concern Wind Energy Conversion System (WECS) which is connected to the distribution system with an installed capacity of more than 10 MW.

2.1.1. Fault Ride Through Capability

The ability of generators to remain stable and connected to the grid when faults occur on the transmission or distribution system is known as fault ride through capability.

According to TWTNR, wind turbines connected to the grid should satisfy the demands given in Figure 2.4. In the case of voltage dips in one or all phases, wind turbines should stay connected to the grid in region 1 and 2. If the voltage dip is in region 1

during the fault, WECS should reach its maximum power by increasing its power at least 20% of rated power in every second after the fault is disappeared. On the other hand, if the voltage dip is in region 2 during the fault, WECS should reach its maximum power by increasing its power at least 5% of rated power in every second after the fault is disappeared.

Voltage fluctuations between 0.9-1.1 pu are accepted as normal operating conditions by TWTNR and WECS should satisfy the reactive power support requirements in this range.

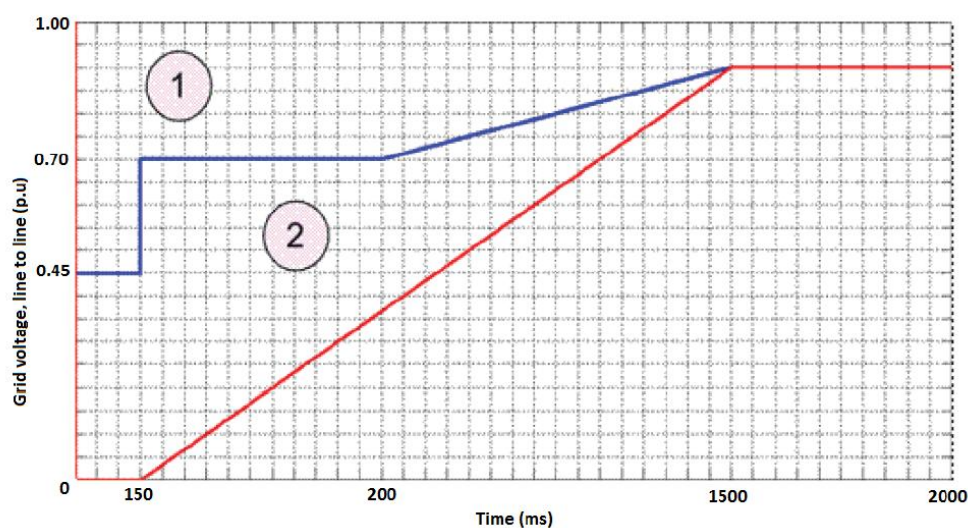


Figure 2.4. Fault Ride Through Requirements Determined by TWTNR [10]

During the fault on the grid connection point, if voltage fluctuations are greater than $\pm 10\%$, each wind turbine generator should provide maximum reactive current support in inductive or capacitive directions at levels up to 100% of the rated current, without exceeding the transient current ratings. The support should reach the maximum reactive current value within 60 ms with a 10% error margin and be maintained for 1.5 s.

2.1.2. Active Power Control

The active power output of WECS should be controllable by Transmission System Operator (TSO) between 20%-100% of the available power of the plant under the current conditions. For WECS rated up to 100 MW, load acceptance rate should not exceed 5% of the rated power per minute and load reduction rate should not be below 5% of the rated power per minute. For WECS rated above 100 MW, load acceptance rate should not exceed 4% of the rated power per minute and load reduction rate should not be below 4% of the rated power per minute.

The WECS frequency response should be within the limits of the power-frequency curve given in Figure 2.5. The WECS should be able to supply its rated power as long as the grid frequency is in the range of 47.5-50.3 Hz. If the frequency increase beyond 50.3 Hz, the WECS should reduce injected power to the grid by following Figure 2.5.

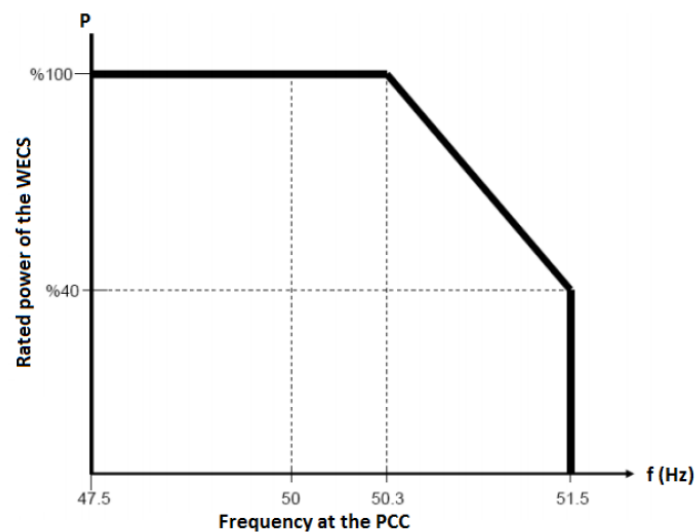


Figure 2.5. Active Power Control Requirements Determined by TWTNR [10]

2.1.3. Reactive Power Control

The WECS should continuously operate at each point within the limits indicated by dark lines in Figure 2.6 for the reactive power values at PCC of the transmission or distribution system.

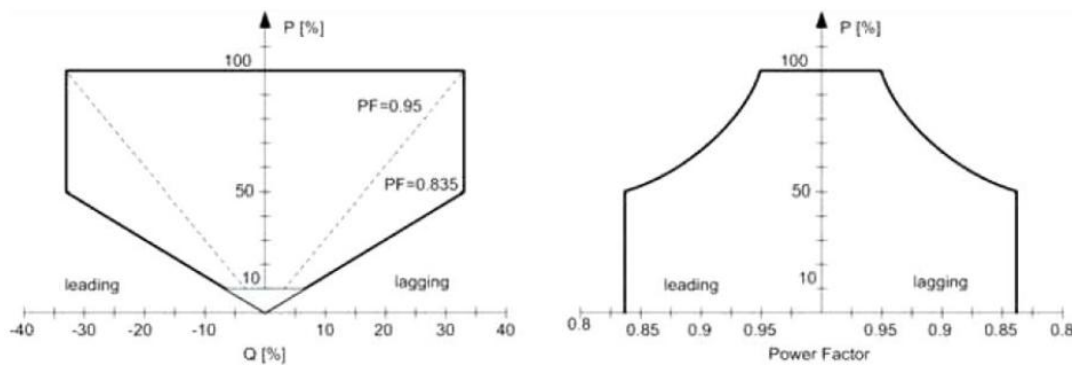


Figure 2.6. Reactive Power Control Requirements Determined by TWTNR [10]

The reactive power demands determined by TSO should be satisfied depending on the voltage as indicated in Figure 2.7.

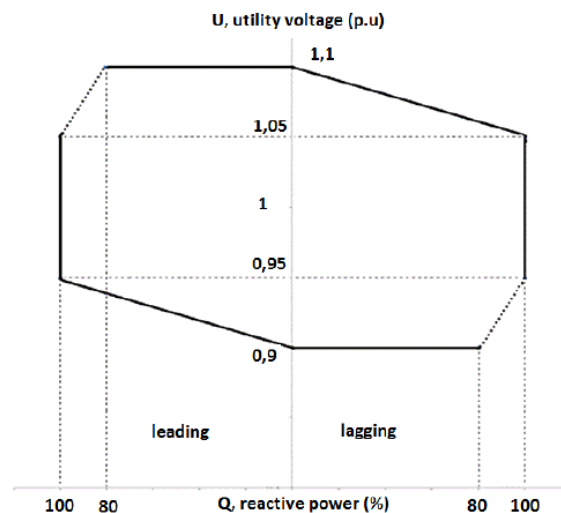


Figure 2.7. Reactive Power against Utility Voltage Requirements Determined by TWTNR [10]

Under normal operating conditions defined between 0.9-1.1 pu PCC voltage, WECS should continuously respond to voltage changes at PCC in accordance with the characteristics specified in Figure 2.8. “Droop” value is between 2-7% and is determined by TSO. The WECS should start to respond to a sudden step change at the PCC voltage within 200 ms and output reactive power should reach 90% of the balance value within 1 s. Balance should be achieved in 2 s and the peak value of the reactive power fluctuations should not exceed 2% of the actual change.

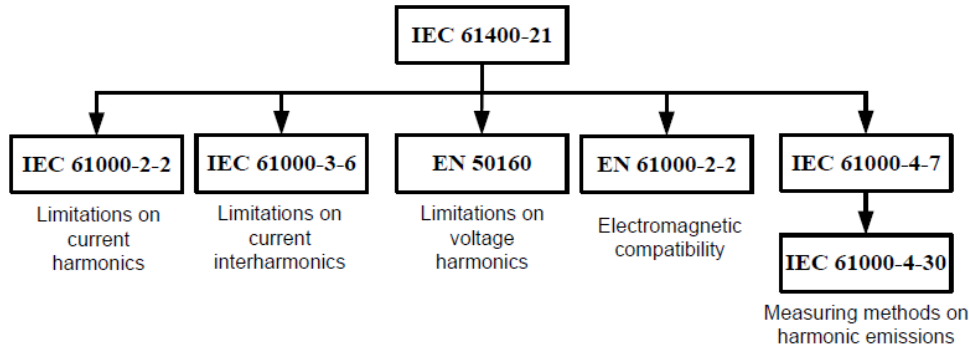


Figure 2.9. Harmonic Standards for Grid Integration of WECS [5]

2.2. Back to Back Converter Design

Wind turbine control requires both fast and slow dynamic control. Aerodynamic system controls the power flow based on a set-point given by TSO or locally with the aim of maximum available power generation. The power injected into the grid is controlled by electrical and mechanical subsystems. Electrical subsystem is responsible for control of the grid connection, active and reactive power flow and overload protection. The mechanical subsystem focuses on power limitation with the adjustment of yaw and pitch angles, capture of maximum power, speed limitation and acoustical noise reduction. The power may be limited via both electrical and mechanical braking systems because the redundancy is supported by standards. These subsystems are controlled independent of each other with different bandwidths. The general control scheme of a wind turbine is given in Figure 2.10.

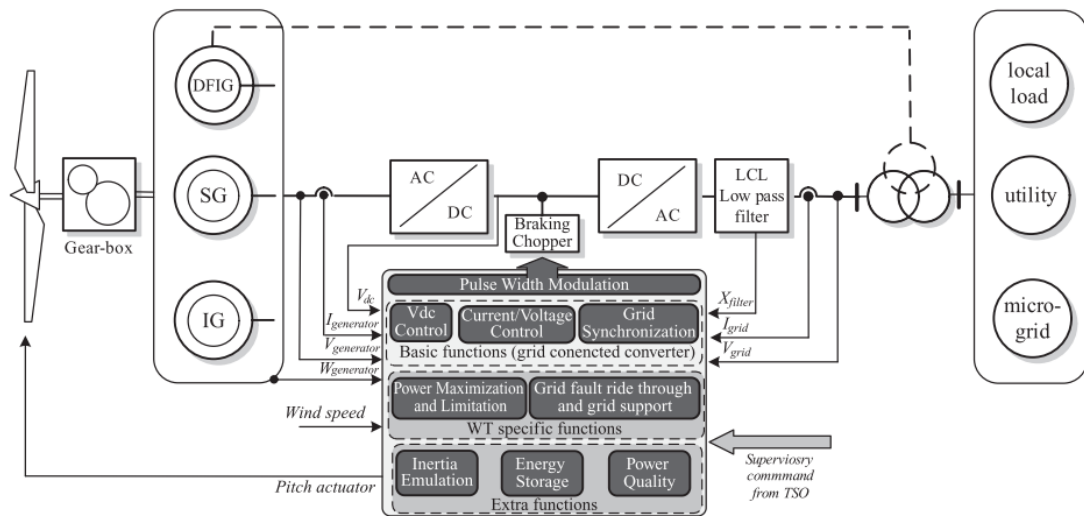


Figure 2.10. Control Scheme of a WECS [14]

Speed of the wind turbine typically varies in proportion to the wind speed and keep the pitch angle fixed below the rated turbine speed. If the wind speed exceeds the rated wind speed of the turbine, pitch angles should be limited in order to maintain nominal power generation. Generator side converter controller focuses on extracting maximum power from the wind. The aim of the grid side converter controller is keeping the DC link voltage constant. For this purposes, several internal current and voltage loops are used in both converter controllers [14]. A simple inductor or an LCL filter is used at the grid connection point as a low pass filter in order to meet standard and grid code requirements. The use of an LCL filter provides lower inductance values and so allows a more compact design with lower losses.

2.3. Generator Side Control

Several types of generators such as: Double Fed Induction Generator (DFIG), SCIG, PMSG and WRSG can be used with back to back converter in wind turbine configurations. When compared to other generator types, SCIG has advantages in terms of cost, reliability and robustness [15]. A variable speed wind turbine with a full scale power converter and SCIG is one of the most suitable option [16] and given in Figure 2.11.

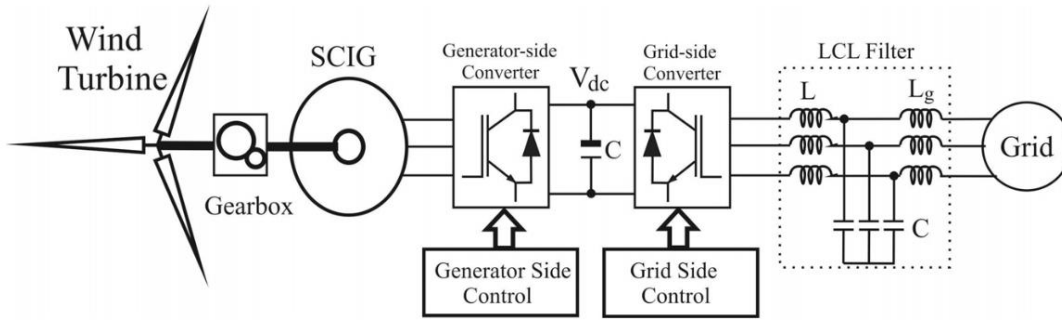


Figure 2.11. A variable speed wind turbine with a full scale power converter and SCIG [17]

The most widely used techniques for generator side control are classified as Field Oriented Control (FOC), Voltage Oriented Control (VOC) and Direct Torque Control (DTC). The main principle of these techniques is independent control of flux and torque through the control of independent stator current dq components [17].

2.3.1. Squirrel Cage Induction Machine Model

The complex vector equivalent circuit of an induction machine is given in Figure 2.12 where p represents the operator d/dt and $\vec{v}_{dqr} = 0$ since there is no voltage drop on the rotor of squirrel cage induction machines.

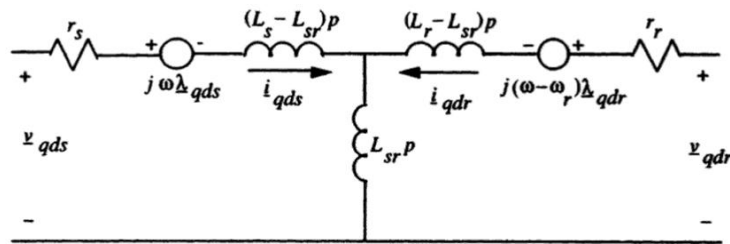


Figure 2.12. Complex Vector Equivalent Circuit of Induction Machines [18]

The induction machine can be represented in dq synchronous reference frame by Eq. (2.1) and (2.2) with the relationship between currents and fluxes are given by Eq. (2.3) and (2.4) where the quantities \mathbf{v} , \mathbf{i} and $\boldsymbol{\lambda}$ are the space vectors of voltage, current and magnetic flux respectively. r and L correspond to the per phase resistance and inductance of windings. The subscripts s , r and sr denote the stator, rotor and

magnetization respectively. pp and ω_r indicates the number of pole pairs and angular mechanical speed of the rotor [17].

$$\vec{v}_{qds} = r_s \vec{i}_{qds} + \frac{d\vec{\lambda}_{qds}}{dt} + j\omega \vec{\lambda}_{qds} \quad (2.1)$$

$$0 = r_r \vec{i}_{qdr} + \frac{d\vec{\lambda}_{qdr}}{dt} + j(\omega - pp\omega_r) \vec{\lambda}_{qdr} \quad (2.2)$$

$$\vec{\lambda}_{qds} = L_s \vec{i}_{qds} + L_{sr} \vec{i}_{qdr} \quad (2.3)$$

$$\vec{\lambda}_{qdr} = L_{sr} \vec{i}_{qds} + L_r \vec{i}_{qdr} \quad (2.4)$$

Mechanical dynamics of the machine is given by Eq. (2.5) where T_e and T_L correspond to electromechanic and mechanical torque.

$$J \frac{d\omega_r}{dt} = T_e - T_L \quad (2.5)$$

2.3.2. Rotor Flux Oriented Control

The idea of the rotor flux oriented control is fixing the direct axis of the synchronous coordinate system with the rotor flux vector expressed in the stationary frame. The expression is given in Eq. (2.6) where λ_r is the magnitude and θ_r is the instantaneous spatial position of the rotor flux vector.

$$\vec{\lambda}_{\alpha\beta r} = \lambda_r e^{j\theta_r} \quad (2.6)$$

When direct axis of the dq reference frame coincides with the rotor flux vector, the quadrature axis component will be zero ($\lambda_{qr} = 0$) and thus the direct axis component will be the actual rotor flux as in Eq. (2.7).

$$|\lambda_{qdr}| = \lambda_{dr} = \lambda_r \quad (2.7)$$

Electromagnetic torque becomes proportional with the multiplication of the rotor flux and quadrature axis component of the stator current thanks to rotor flux orientation. The mathematical expression of the electromechanical torque is given by Eq. (2.8)

As stated before, rotor flux oriented control uses d and q components of the SCIG stator currents to control the rotor flux and electromagnetic torque respectively. The performed transformations in the controller are given in Appendix A. In order to control current components, three phase two level VSI generates stator voltages by using PI controllers that process the error signals of torque and rotor flux. As seen in Figure 2.13, the current control loops are performed independently thanks to decoupling of the reference calculations of stator currents. Besides that, torque and rotor flux controllers are added as outer control loops [17]. Position (θ_r) and magnitude (λ_r) of the rotor flux are necessary for rotor flux operation and estimated as given in Eq. (2.11) and (2.12) by using Eq. (2.10) [17].

$$\vec{\lambda}_{\alpha\beta r} = \frac{L_r}{L_{sr}} \int (\vec{v}_{\alpha\beta s} - r_s \vec{i}_{\alpha\beta s}) dt + \frac{L_{sr}^2 - L_s L_r}{L_{sr}} \vec{i}_{\alpha\beta s} \quad (2.10)$$

$$\theta_r = tg^{-1} \left(\frac{\lambda_{\beta r}}{\lambda_{\alpha r}} \right) \quad (2.11)$$

$$\lambda_r = \vec{\lambda}_{dr} = |\lambda_{\alpha\beta r}| = \sqrt{\lambda_{\alpha r}^2 + \lambda_{\beta r}^2} \quad (2.12)$$

By using cascaded control scheme given in Figure 2.13, d and q components of the stator current are used to control the flux and torque of the SCIG respectively.

2.4. Grid Side Control

Grid side converter controller generally includes two cascaded loops. The inner one has a fast dynamic response and is used for the injected grid current control. The current control loop focuses on current protection and power quality issues and so harmonic compensation and dynamics of the system become important parameters. The outer loop has a relatively slower dynamic response and is responsible for the control of DC link voltage in order to balance power flow of the system [19]–[22]. The control strategies are classified as synchronous reference, stationary reference and natural frame control.

performance, low-order harmonic compensation capability of the PI controller is very poor in grid connected systems [22].

2.4.2. Stationary Reference Frame Control

In stationary reference frame control, grid current waveforms are transformed into stationary frame using abc to $\alpha\beta$ transformation. General structure of stationary reference frame control is given in Figure 2.15.

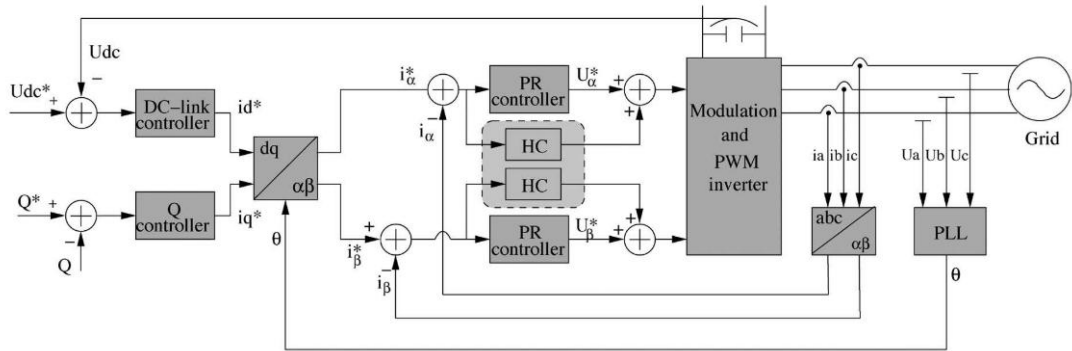


Figure 2.15. General Structure of Stationary Reference Frame Control [22]

Transfer function of a Proportional Resonant (PR) controller $G_{PR}(s)$ is given as in Eq. (2.14) where ω is the resonance frequency, K_p is the proportional gain and K_i is the integral gain of the controller.

$$G_{PR}(s) = K_p + \frac{K_i s}{s^2 + \omega^2} \quad (2.14)$$

PR controller has a very high gain around resonance frequency and thus, perform zero steady state error between the controlled signal and its reference. The width of the frequency band around resonance frequency is adjusted by integral time constant K_i [30]–[35]. This feature becomes PR controller more popular in grid connected systems.

2.4.3. Natural Frame Control

In natural frame control, each grid current is controlled individually. While designing the controller, connection type of the grid such as delta, star with or without isolated

neutral line should be considered. In natural frame control, also called *abc* control, hysteresis and dead beat controllers are preferred. The performance of these nonlinear controllers depend on sampling frequency because of their high dynamics. General structure of a natural frame control is given in Figure 2.16.

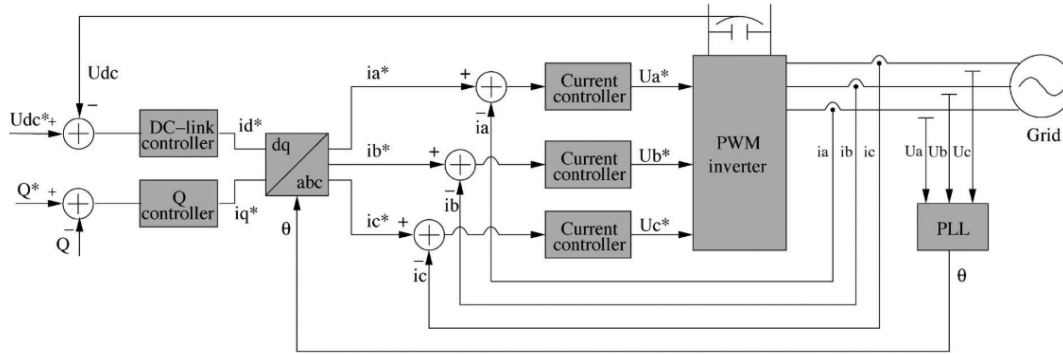


Figure 2.16. General Structure of Natural Frame Control [22]

Active and reactive current references are set by DC link voltage and reactive power controllers respectively. The current references for each phase is created by $dq \rightarrow abc$ transformation using the phase angle of the grid voltages generated by the PLL system. If a dead beat or hysteresis controller is used in current loop, a modulator is not necessary since these controllers generates the switching states of the power controller switches. Using of PI controller in current loop is more complex and requires a modulator to generate duty cycle of the PWM pattern [22].

2.5. PWM Modulation

The output voltage waveforms of the inverters depend on the switching states of the six switches. The harmonic contents, switching frequency and best utilization of DC link voltage are main requirements and limitations of inverters. In order to achieve lower harmonic contents and lower switching losses with best utilized DC link voltage, several Pulse Width Modulation (PWM) techniques such as sinusoidal, hysteresis and space vector PWM are used in the literature [36]. In this study, Space Vector Pulse Width Modulation (SVPWM) is applied and presented due to less harmonic content when compared with commonly used sinusoidal PWM method [37].

The structure of a two level three phase VSI is shown in Figure 2.17. Q_1 through Q_6 represent six switching devices which are controlled by a, a', b, b', c and c' . Switching devices in the same leg are used complementarily. For this reason, the states of a, b and c are sufficient to evaluate the output voltage waveform [38].

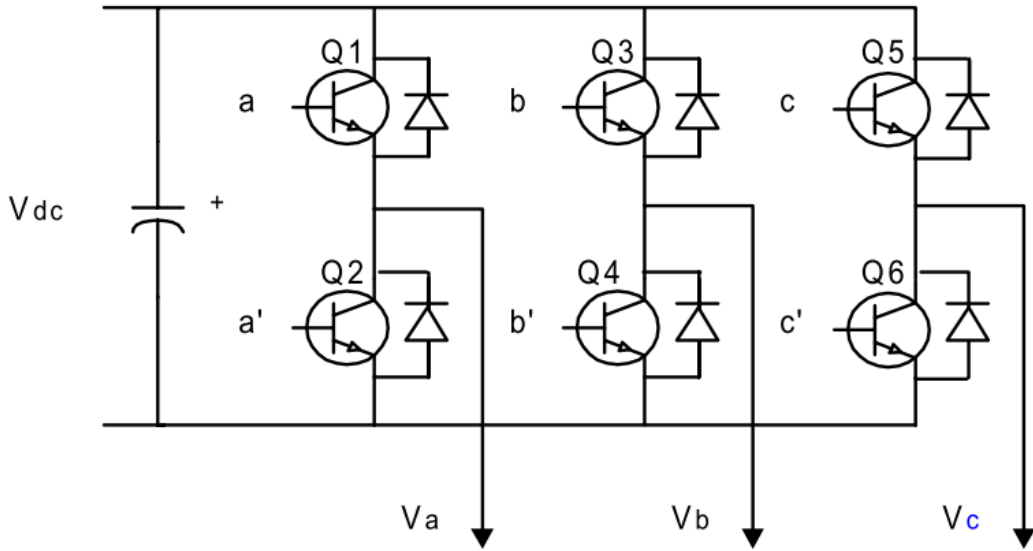


Figure 2.17. The Structure of Two Level Three Phase Inverters [38]

Line-to-line output voltage vector $[V_{ab} V_{bc} V_{ca}]^t$ and line-to-neutral output voltage vector $[V_a V_b V_c]^t$ are expressed in Eq. (2.15) and (2.16) in terms of switching variable vector $[a b c]^t$ where V_{dc} is the DC link voltage [38].

$$\begin{bmatrix} V_{ab} \\ V_{bc} \\ V_{ca} \end{bmatrix} = V_{dc} \begin{bmatrix} 1 & -1 & 0 \\ 0 & 1 & -1 \\ -1 & 0 & 1 \end{bmatrix} \begin{bmatrix} a \\ b \\ c \end{bmatrix} \quad (2.15)$$

$$\begin{bmatrix} V_a \\ V_b \\ V_c \end{bmatrix} = \frac{1}{3} V_{dc} \begin{bmatrix} 2 & -1 & -1 \\ -1 & 2 & -1 \\ -1 & -1 & 2 \end{bmatrix} \begin{bmatrix} a \\ b \\ c \end{bmatrix} \quad (2.16)$$

The combinations are shown in Table 2.2 by considering output phase and line-to-line voltages in terms of DC link voltage.

Table 2.2. *Switching States and Corresponding Output Voltages*

a	b	c	V_a	V_b	V_c	V_{ab}	V_{bc}	V_{ca}
0	0	0	0	0	0	0	0	0
1	0	0	2/3	-1/3	-1/3	1	0	-1
1	1	0	1/3	1/3	-2/3	0	1	-1
0	1	0	-1/3	2/3	-1/3	-1	1	0
0	1	1	-2/3	1/3	1/3	-1	0	1
0	0	1	-1/3	-1/3	2/3	0	-1	1
1	0	1	1/3	-2/3	1/3	1	-1	0
1	1	1	0	0	0	0	0	0

Assume that α and β are the fixed horizontal and vertical axis in the three phase plane. The transformation from abc to $\alpha\beta$ is done as given in Appendix. As seen by Figure 2.18, six active ($\vec{U}_1, \vec{U}_2, \vec{U}_3, \vec{U}_4, \vec{U}_5$ and \vec{U}_6) and two inactive (\vec{U}_0, \vec{U}_7) voltage vectors are formed by switching states. Active space vectors are separated from each other by 60 degrees and forms a hexagon which includes six sectors. The aim of the SVPWM technique is to express any voltage vector in terms of the summation of the basic space vectors. The commonly used working sequence of the basic vectors is given in Table 2.3 and corresponding signal waveforms of upper switches for each sector are shown in Figure 2.18.

Table 2.3. *Working Sequence of the Basic Vectors for Each Sector*

Sector Number	Working Sequence of the Basic Vectors
1	$\vec{U}_0 \rightarrow \vec{U}_1 \rightarrow \vec{U}_2 \rightarrow \vec{U}_7 \rightarrow \vec{U}_2 \rightarrow \vec{U}_1 \rightarrow \vec{U}_0$
2	$\vec{U}_0 \rightarrow \vec{U}_3 \rightarrow \vec{U}_2 \rightarrow \vec{U}_7 \rightarrow \vec{U}_2 \rightarrow \vec{U}_3 \rightarrow \vec{U}_0$
3	$\vec{U}_0 \rightarrow \vec{U}_3 \rightarrow \vec{U}_4 \rightarrow \vec{U}_7 \rightarrow \vec{U}_4 \rightarrow \vec{U}_3 \rightarrow \vec{U}_0$
4	$\vec{U}_0 \rightarrow \vec{U}_5 \rightarrow \vec{U}_4 \rightarrow \vec{U}_7 \rightarrow \vec{U}_4 \rightarrow \vec{U}_5 \rightarrow \vec{U}_0$
5	$\vec{U}_0 \rightarrow \vec{U}_5 \rightarrow \vec{U}_6 \rightarrow \vec{U}_7 \rightarrow \vec{U}_6 \rightarrow \vec{U}_5 \rightarrow \vec{U}_0$
6	$\vec{U}_0 \rightarrow \vec{U}_1 \rightarrow \vec{U}_6 \rightarrow \vec{U}_7 \rightarrow \vec{U}_6 \rightarrow \vec{U}_1 \rightarrow \vec{U}_0$

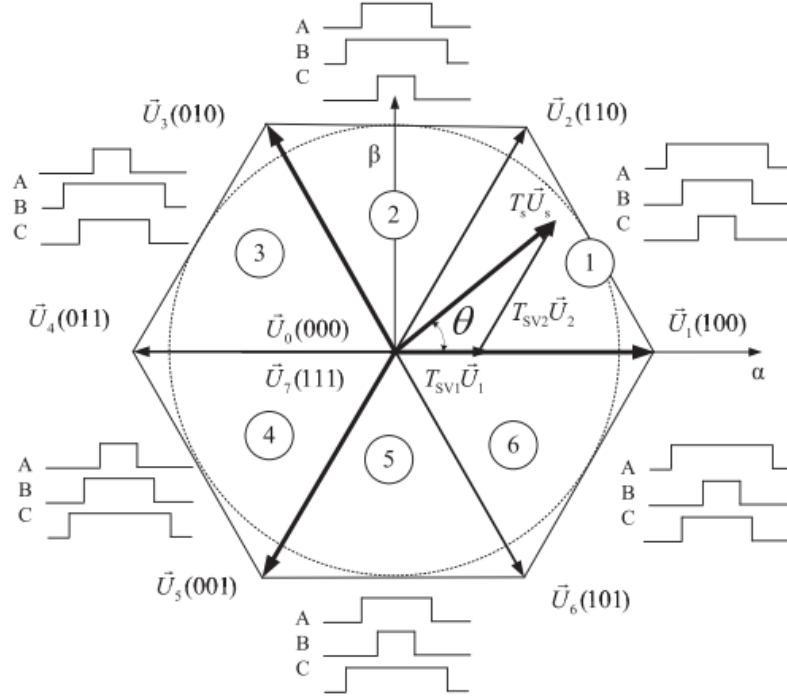


Figure 2.18. Voltage Vector, Vector Summation Method and PWM Waveforms in Six Sectors [39]

The vector summation method is given in the first sector where T_{sw} represents switching period, \vec{U}_s is the target voltage vector whose argument is θ and T_1, T_2 and T_0 are the duration times of \vec{U}_1, \vec{U}_2 and zero vector (\vec{U}_0 or \vec{U}_7) [39]. Assuming that, the change in reference vector U_s is small within the switching period T_{sw} , the relation between reference vector and space vector is given by Eq. (2.17) where switching period is expressed in terms of space vector durations by Eq. (2.18).

$$T_{sw}U_s = T_1U_1 + T_2U_2 + T_0(U_0 \text{ or } U_7) \quad (2.17)$$

$$T_{sw} = T_1 + T_2 + T_0 \quad (2.18)$$

In addition, switching times of the space vectors can be determined from Figure 2.18 as given by Eq. (2.19) and (2.20).

$$T_1 = \frac{2}{\sqrt{3}} \frac{U_s}{U_1} \cos(\theta + 30) \quad (2.19)$$

$$T_2 = \frac{2}{\sqrt{3}} \frac{U_s}{U_2} \sin(\theta) \quad (2.20)$$

By depending on the application either Eq. (2.19) or (2.20) can be used. Eq. (2.19) is sector dependent and useful when U_s is given in the form of $\alpha\beta$. In this implementation, the matrix inverse of each sector is calculated before and used as a look up table during online calculations. Eq. (2.20) is sector independent and useful when U_s is given in the form of magnitude and phase angle [38].

2.6. Summary

This chapter focuses on the overall description of a full scale back-to-back wind turbine converter. Types of wind turbines are presented and compared in terms of technical performances. Grid code requirements determined by TWTNR and international standards about active and reactive power control, fault ride through capability, power quality and grid support during network disturbances are mentioned. General control schemes and power circuits of wind turbines for different topologies are given. A back-to-back converter are divided into two parts as generator and grid side which are connected at a common DC link. The control scheme of generator side converter is given for rotor flux oriented control. In this control structure, d and q components of the stator currents are used to control flux and torque as independent of each other. In addition to generator side, grid side controller is presented in three reference frames as synchronous, stationary and natural. All control schemes have a cascaded structure and DC voltage controller sets the reference of current controllers. At the last part, as a modulation technique, SVPWM is offered and explained in detail for VSIs.

CHAPTER 3

GRID SIDE CONTROLLER AND LCL FILTER

Back to back converters are mostly utilized in modern wind turbines in order to control active and reactive power flow completely and improve the quality of the injected power. This study focuses on the grid side control of the WECS and the generator side is simply modeled as a current source as given in Figure 3.1.

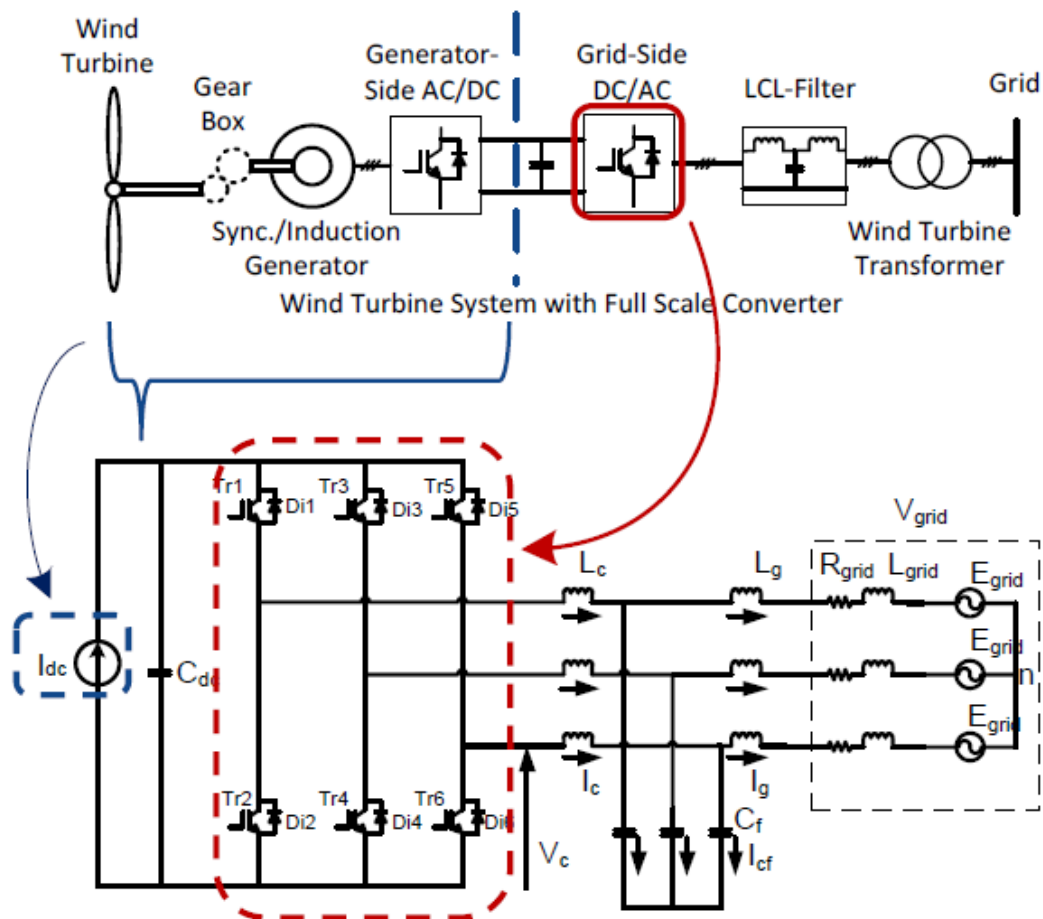


Figure 3.1. The Scope of the Thesis [40]

Three phase two level VSI is composed of six IGBTs with antiparallel diodes and connected to the grid via a low pass LCL filter. DC link capacitors are charged by the generator side converter and discharged through the grid by VSI. Control scheme of the grid side converter is given in Figure 3.2.

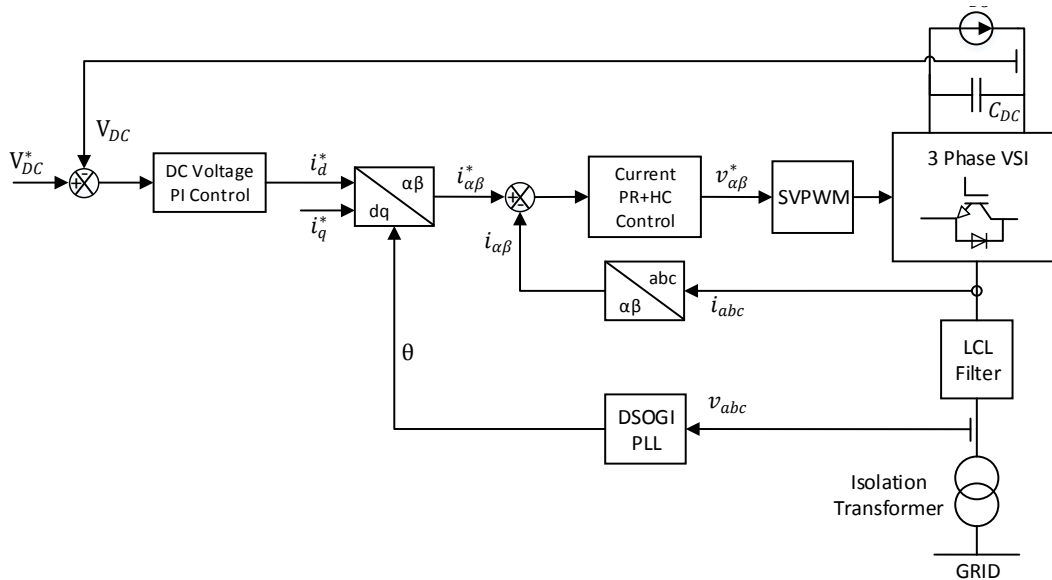


Figure 3.2. Control Scheme of the Grid Side Converter

LCL filters are generally preferred at the grid interface for the purpose of eliminating high frequency contents of voltage and current waveforms. However, LCL filters brings the system some stability problems because of the resonance effect. In the literature, there are two methods called as active and passive damping. Passive damping methods provides hardware solutions like insertion of a serial resistor to filter capacitors. Passive damping is easy to implement but causes additional power losses on the passive elements. Active damping method is performed by modifying control algorithms. There are several different active damping implementations in the literature which requires additional sensors and more complex controller algorithms [41]–[44]. Despite the papers show that active damping methods can enlarge the stability margins, these methods are too complicated and sensitive against parameter

variations [45]. For this reason, passive damped LCL filters are generally used in the industry especially high power application in spite of the additional power losses.

3.1. LCL Filter

Design of LCL filters have a crucial importance for grid-connected PWM based inverters. A filter which is not well designed can cause instabilities because of insufficiently damped resonance effects. Also, it can be inadequate to attenuate high frequency ripples at switching frequency and its sideband harmonics. In addition, high power losses can occur on damping circuits and get worse overall efficiency of the system. Per phase equivalent circuits of passive damped LCL filter topologies are given in Figure 3.3.

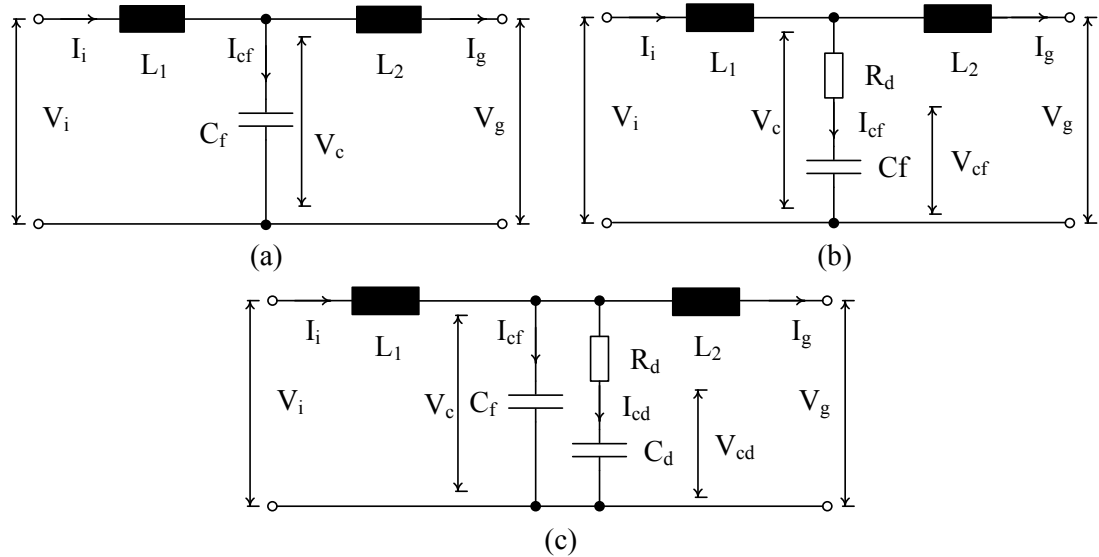


Figure 3.3. Per Phase Equivalent Circuits of Undamped (a), Series R Damped (b) and Shunt R-C Damped (c) LCL Filters

In this part, a systematic optimum design procedure of LCL filters is given for grid-connected inverters [46].

- Total inductor value should be limited at 0.1 pu to not have a large voltage drop on the inductors [47]. Then, maximum total inductor value can be found by Eq. (3.1) where V_{gmax} represents maximum grid voltage, f_g is the grid frequency and P_n is the rated power.

$$L_{Tmax} = 10\% \frac{V_g^2}{2\pi f_g P_n} \quad (3.1)$$

- Maximum filter capacitance C_{fmax} can be selected by Eq. (3.2) where x is the percentage of the base capacitance at rated conditions.

$$C_{fmax} = x\% \frac{P_n}{2\pi f_g V_g^2} \quad (3.2)$$

Reactive power consumed by the capacitors should not exceed 5% of the rated active power in order not to decrease power factor. In low power applications, choosing capacitor value as half of the maximum capacitance value is recommended to decrease reactive power consumed by capacitor. However, inductor values should be increased to have a similar attenuation performance with lower capacitor value. For this reason, capacitor value is selected with upper limit in high power applications.

- Converter side inductor value L_1 can be selected by Eq. (3.3) where Δi_{1max} is the maximum current ripple in the inductor defined by Eq. (3.4) where k_a is the desired current ripple on the inductor current at switching frequency [48].

$$L_{1min} = \frac{V_{dc}}{24f_s \Delta i_{1max}} \quad (3.3)$$

$$\Delta i_{1max} = k_a \frac{\sqrt{2}P_n}{\sqrt{3}V_g} \quad (3.4)$$

Current ripple limit in the converter side inductor is generally determined as 10%. Improved attenuation performance requires larger inductor value and causes larger size and cost. Selecting close inductor values can provide optimum cost and size for design. Inverter side inductor value L_1 can be selected 3 times grid side one L_2 as a reference value. If the system is connected to the grid by an isolation transformer, inverter side inductor value L_1 can be selected 2 times grid side one L_2 [49].

- Grid side inductor value L_2 is determined using the relation between L_1 by Eq. (3.5) where a is given by Eq. (3.6) and the condition given by Eq. (3.7) should be satisfied.

$$\delta = \left| \frac{i_{gsw}}{i_{csw}} \right| = \frac{1}{|1+a(1-L_1.C_f.\omega_{sw}^2)|} \quad (3.5)$$

$$a = \frac{L_2}{L_1} \quad (3.6)$$

$$0 \leq a \leq \frac{L_{Tmax}}{L_1} - 1 \quad (3.7)$$

Also, δ represents harmonic attenuation of the grid side inductor. Upper value for grid side inductance L_2 is limited by the voltage drop for unity power factor operation. Lower value is determined to satisfy IEEE 519-2014 high-frequency grid current harmonic specifications [50]. To ensure this requirement, current ripple attenuation at switching frequency should be lower than 2%.

- When the reactive filter components are determined, resonance frequency of the LCL filter is calculated by Eq. (3.8) and the condition given by Eq. (3.9) should be satisfied to avoid from resonance at high and low frequencies.

$$f_{res} = \frac{1}{2\pi} \sqrt{\frac{L_1+L_2}{L_1L_2C_f}} \quad (3.8)$$

$$10f_g \leq f_{res} \leq \frac{f_{sw}}{2} \quad (3.9)$$

- With the aim of avoiding resonance problem, a series resistor can be added to filter capacitor as shown in Figure 3.3. Series R damped is the simplest passive damping solution and it provides nearly 40 dB/decade current attenuation after resonance frequency. Disadvantage of the method is that large amount of power loss occurs on the damping resistor R_d . The value of the damping resistor should be limited by Eq. (3.10) considering power loss where i_{R_n} is the current goes through the resistor at n^{th} harmonic frequency.

$$P_{loss} = 3R_d \sum_n i_{R_n}^2 \quad (3.10)$$

Power loss on the resistors should be limited at most 1% of the rated power [51].

- In order to improve attenuation performance and decrease the damping resistor losses of the LCL filter passive shunt R-C damped whose per phase equivalent

circuit is given in Figure 3.3 can be utilized instead of series R damped. Shunt R-C damped filter can provide approximately 60 dB/decade current attenuation at frequencies larger than resonance frequency. The predetermined capacitor value is divided between filter and damping capacitors. Larger damping capacitor provides better attenuation performance but increases current goes through the resistor and larger power loss occurs on the damping circuit. Therefore, there is a trade-off between attenuation capability at high frequencies and power losses of the LCL filter [52].

Stability analysis of grid connected VSI with passive damped LCL filter is performed by carrying out discrete z-domain root locus and nonlinear model. While doing the analysis passive series R and shunt R-C damped LCL filters are considered with converter and grid current feedbacks [53]. The analysis also considers PWM and computational time delays [54], [55]. The analyzed system is given by Figure 3.2. VSI is connected to the grid through the LCL filter which is shown as a black box. By following design procedure an LCL filter is designed and whose parameters are given in Table 3.1 with other system parameters.

Table 3.1. *System Parameters*

Symbol	Quantity	Value	Unit
V_g	Nominal line-to-line grid voltage	400	V_{rms}
f_g	Grid frequency	50	Hz
S_n	Nominal power	300	kVA
f_{sw}	Switching frequency	5	kHz
f_{samp}	Sampling frequency	10	kHz
V_{DC}	DC link voltage	700	V
L_1	Converter side inductance	125	μH
L_2	Grid side inductance	60	μH
C_f	Filter capacitance for shunt R-C damped	100	μF
C_d	Damping capacitance for shunt R-C damped	200	μF
C_f	Filter capacitance for undamped and series R damped	300	μF
R_d	Damping resistance	0.9	Ω

The voltages at the PCC is measured in order to synchronize with the grid. Besides, DC link voltage and converter or line currents are measured to complete the controller loops.

While performing stability analysis, parasitic effects of the passive components such as equivalent series resistances of the capacitors, copper and core losses of the inductors are neglected. Thus, worst case scenarios are considered because these parasitic effects have positive impact on the damping of the resonances. By considering ideal conditions, admittance transfer functions of the undamped LCL filter with converter and grid current feedbacks are given in Eq. (3.11) and (3.12) respectively.

$$\frac{I_c(s)}{V_c(s)} = \frac{L_2 C_f s^2 + 1}{L_1 L_2 C_f s^3 + (L_1 + L_2)s} \quad (3.11)$$

$$\frac{I_g(s)}{V_c(s)} = \frac{1}{L_1 L_2 C_f s^3 + (L_1 + L_2)s} \quad (3.12)$$

In order to prevent the system controller against instabilities, the resonance should be damped. As stated before, several active and passive damping methods were presented in the literature. In this study, passive damping methods will be investigated because in high power application, switching frequency of the converter is limited in order to reduce power losses and active damping implementation becomes difficult. Also, passive damping does not require additional sensors and it is robust against parameter variations. Most popular passive damping method in the literature is addition of a series resistors to filter capacitors and called as series R damping. Single phase equivalent circuit of series R damped LCL filter is shown in Figure 3.3. Frequency domain transfer functions of series R damped LCL filters with converter and grid current feedbacks are given by Eq. (3.13) and (3.14) respectively.

$$\frac{I_c(s)}{V_c(s)} = \frac{L_2 C_f s^2 + C_f R_d s + 1}{L_1 L_2 C_f s^3 + C_f R_d (L_1 + L_2) s^2 + (L_1 + L_2)s} \quad (3.13)$$

$$\frac{I_g(s)}{V_c(s)} = \frac{C_f R_d s + 1}{L_1 L_2 C_f s^3 + C_f R_d (L_1 + L_2) s^2 + (L_1 + L_2)s} \quad (3.14)$$

Another passive damping method performed in this study is shunt R-C damping. Shunt R-C damping provides better current ripple attenuation at high frequencies than series R damping with less power losses on damping resistors. The single phase equivalent circuit of the shunt R-C damped LCL filter is shown in Figure 3.10-c and transfer functions are given by Eq. (3.15) and (3.16) for converter and grid current feedbacks respectively.

$$\frac{I_c(s)}{V_g(s)} = \frac{L_2 C_f C_d R_d s^3 + L_2 (C_f + C_d) s^2 + C_d R_d s + 1}{L_1 L_2 C_f C_d R_d s^4 + L_1 L_2 (C_f + C_d) s^3 + C_d R_d (L_1 + L_2) s^2 + (L_1 + L_2) s} \quad (3.15)$$

$$\frac{I_g(s)}{V_g(s)} = \frac{C_d R_d s + 1}{L_1 L_2 C_f C_d R_d s^4 + L_1 L_2 (C_f + C_d) s^3 + C_d R_d (L_1 + L_2) s^2 + (L_1 + L_2) s} \quad (3.16)$$

For the given systems, the measured frequency responses of the LCL filters are shown in Figure 3.4. The measurements are taken by short circuiting the grid sides of the LCL filters. Small signal voltage is applied from converter sides by network analyzer and grid currents are measured.

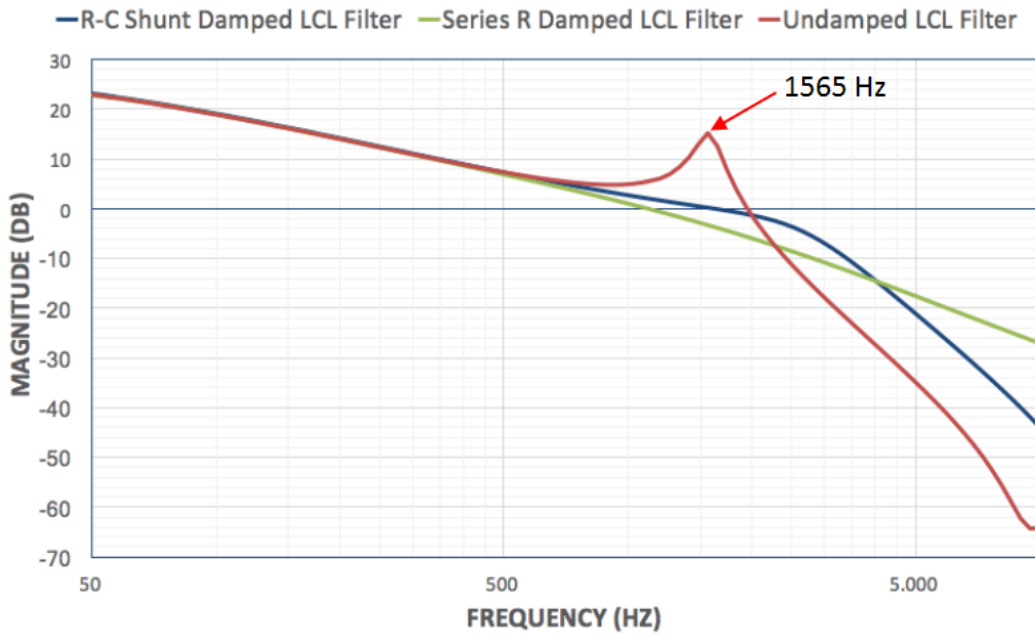


Figure 3.4. Measured Frequency Responses of Undamped and Damped LCL Filters

As seen from the Figure 3.4, undamped LCL filter has 15 dB resonance peak at the resonance frequency which equals to 1565 Hz. Actually, the calculated resonance frequency by using Eq. (3.8) equals to 1443 Hz. There is a small difference between calculated and measured resonance frequency caused by tolerances of the passive components. Both of the damping methods have sufficient attenuation at resonance frequency but at higher frequencies, attenuation performance of the shunt R-C damping is better than series R one.

In both damping methods, increase of damping resistance value brings additional losses. In Figure 3.5, pole zero maps of both damping methods are presented against damping resistance variations. The pole zero map is achieved by discretization of the LCL filter transfer functions according to current controller sampling time.

In both damping methods, absence of the damping resistance represents the undamped case and high frequency poles of the LCL filter are placed on the unity circle. The red arrows on the root locus plots shows the direction of high frequency poles with increasing damping resistance. High frequency poles of series R damped case are attracted towards to the circle center by increasing the damping resistance. However, shunt R-C damped high frequency poles turn back and start closing to the stability limits after 0.8Ω . Thus, 0.9Ω seems the optimum value for damping resistance of shunt R-C LCL filter.

Some analyses were also made by using nonlinear model which is given in Chapter 1. Discrete implementation of the controller is used in this model. Rated power of the converter is injected to the grid through undamped and shunt R-C damped LCL filter. The grid voltage and current waveforms for both methods are given in Figure 3.6. As seen that, the harmonics at resonance frequency are amplified by undamped filter and huge amount of oscillating current ripple is observed. This shows the importance of the effective filter damping.

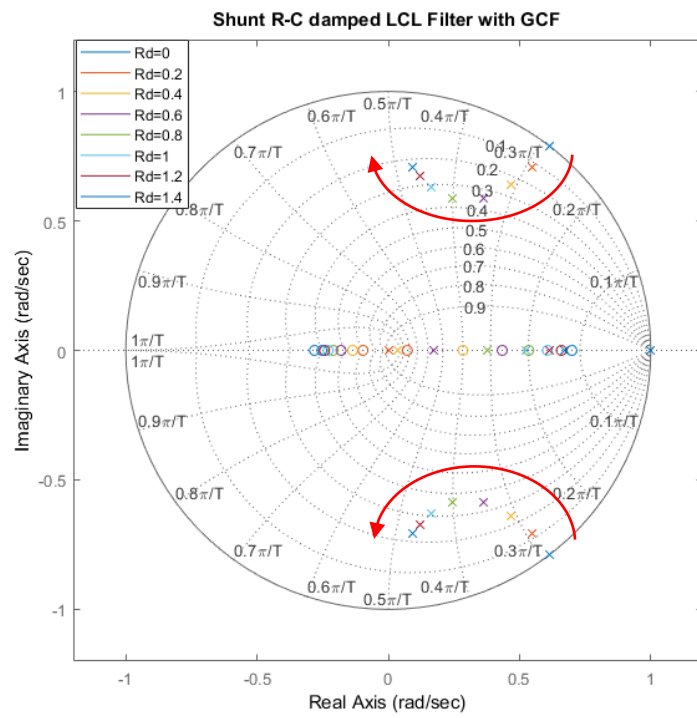
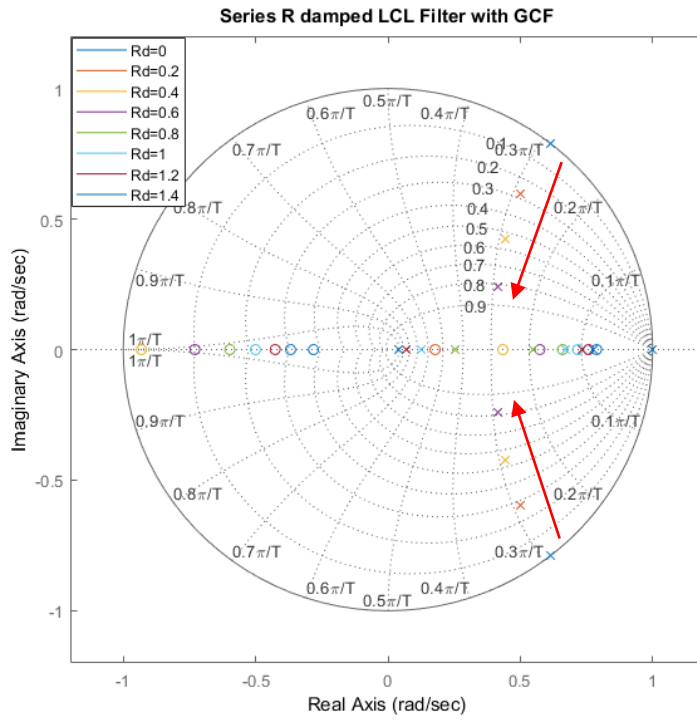
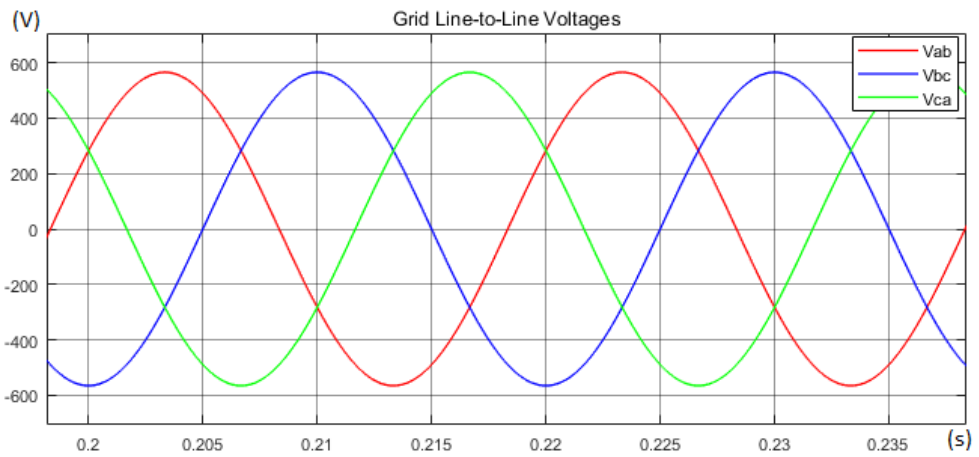
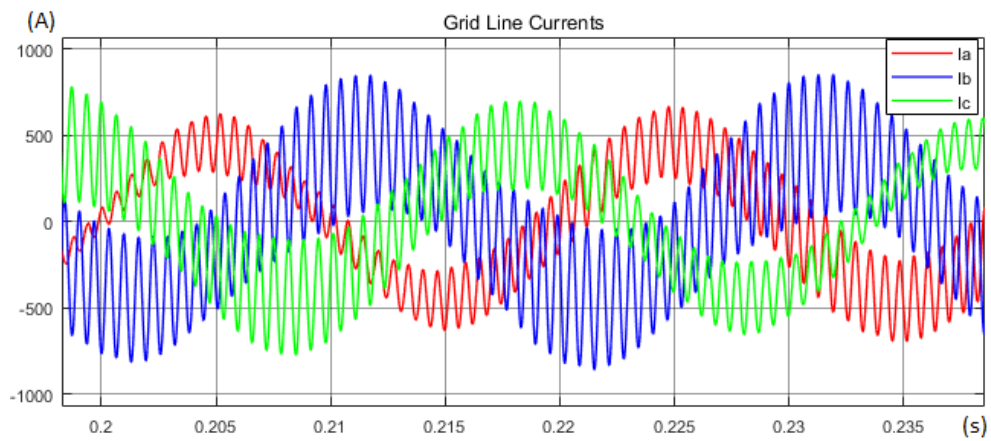


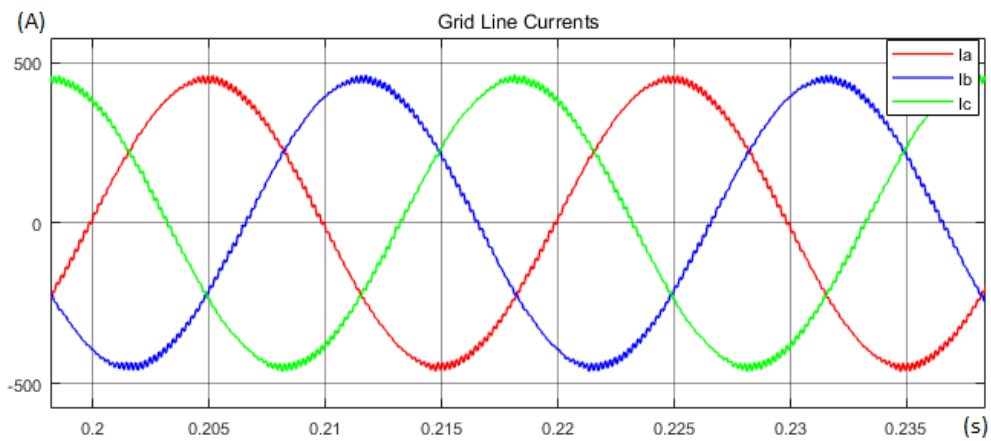
Figure 3.5. Pole Zero Maps of Series R (a) and Shunt R-C (b) Damped LCL Filters for Various R_d



(a)



(b)



(c)

Figure 3.6. Grid Voltage (a) and Current Waveforms for Undamped (b) and Shunt R-C damped (c) LCL Filters

3.2. DC Link Voltage Controller

The DC link voltage controller is mainly responsible for the balance of DC link voltage by adjusting power flow between the generator and grid side converters. Injected power from the generator side charges DC link capacitor and increases DC link voltage. As a result, active current reference of the current controller is raised by the output of the DC link voltage controller in order to maintain voltage balance. The dynamics of the DC link voltage is expressed as in Eq. (3.17) where C_{DC} is the DC link capacitance, i_s is the source current, V_{gd} is d component of the grid voltage and i_{gd} is d component of the injected grid current [54].

$$C_{DC} \frac{dV_{DC}}{dt} = i_s - i_{DC} = i_s - \frac{3V_{gd}i_{gd}}{2V_{DC}} \quad (3.17)$$

In cascaded control, outer voltage loop aims optimum regulation and stability while inner current loop focuses on minimum settling time and unity gain. Therefore, outer voltage loop can be designed 5-20 times slower than the input current loop. In order to decouple inner and outer loops, inner should have larger control bandwidth from the outer one [40]. By considering Eq. (3.17), block diagram of the outer voltage loop is shown in Figure 3.7.

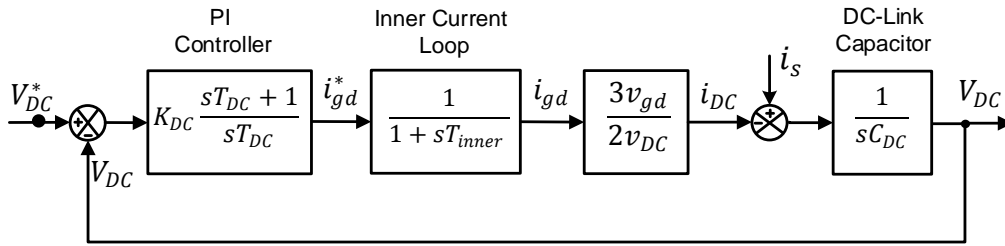


Figure 3.7. Outer DC Link Voltage Loop

DC link voltage PI controller parameters proportional gain K_{DC} and integral time constant T_{DC} are determined by considering symmetrical optimum and given in Eq. (3.18) and (3.19) where the relation between the period of inner loop T_{inner} and sample time T_{samp} are given in Eq. (3.20) [45].

$$K_{DC} = \frac{2}{3} \frac{V_{DC} C_{DC}}{\alpha T_{inner} V_{gd}} \quad (3.18)$$

$$T_{DC} = \alpha^2 T_{inner} \quad (3.19)$$

$$T_{inner} = 4T_{samp} \quad (3.20)$$

As it can be seen from Eq. (3.19) that outer voltage loop is α^2 times slower than inner loop. In order to have a proper decoupling, $\alpha = 3$ is suggested in [54].

3.3. Current Controller

In this study, Proportional Resonant and Harmonic Compensator (PR+HC) is performed as a current controller in stationary $\alpha\beta$ reference frame. The gain of PR is infinite in a narrow bandwidth at resonance frequency and almost zero outside of the bandwidth. In other words, PR controller works like a notch filter and can track a sinusoidal reference signal even at low switching frequencies [20]. The current control loop of a grid connected inverter for PR+HC is given in Figure 3.8 where u_i^* and i_i^* correspond to the inverter voltage and current reference respectively.

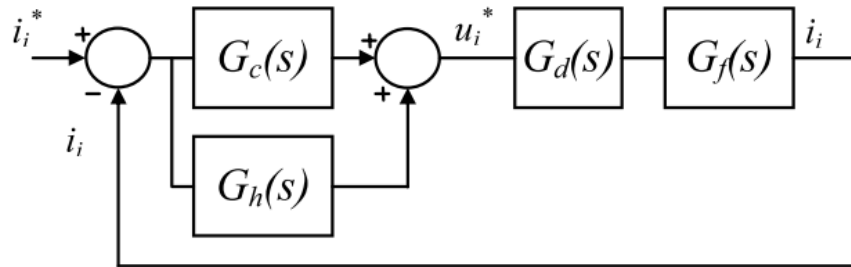


Figure 3.8. The Current Control Loop of Grid Connected Inverter

PR and HC controllers are defined by $G_c(s)$ and $G_h(s)$ whose transfer functions are given by Eq. (3.21) and (3.22) respectively [30], [56].

$$G_c(s) = K_p + K_i \frac{s}{s^2 + \omega_0^2} \quad (3.21)$$

$$G_h(s) = \sum_{h=5,7} K_{ih} \frac{s}{s^2 + (\omega_0 h)^2} \quad (3.22)$$

HC is performed to eliminate the most prominent harmonics of current spectrum. 5th and 7th harmonics are generally compensated by this method in three phase systems. A processing delay $G_d(s)$ which equals to sample time T_s for PWM inverters is added to control scheme. $G_f(s)$ represents the transfer function of the LCL filter.

The classical PR+HC current control strategy with grid voltage feedforward is given in Figure 3.9.

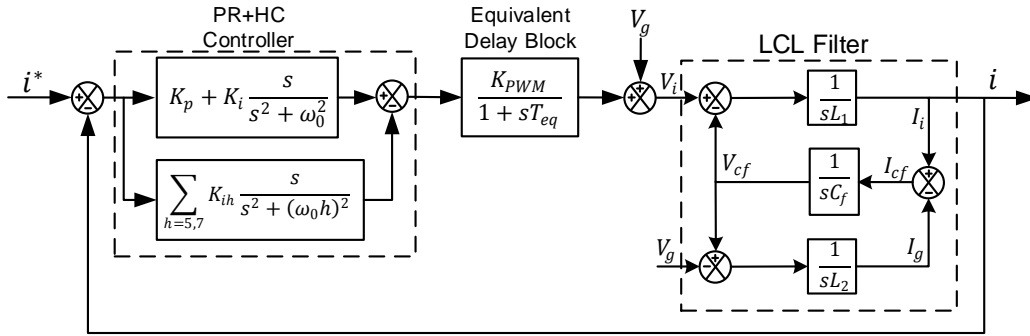


Figure 3.9. Closed Loop Current Control with Plant

In order to design current controller, LCL filter is considered as single L filter by neglecting filter capacitors because LCL filter behaves like an L filter at low frequencies that depends on current controller bandwidth [42]. Thus, the controller can be considered as a first order delay element with the transfer function which is given by Eq. (3.23) [45].

$$\frac{i_c(s)}{V_c(s)} = \frac{1}{s(L_1+L_2)} \quad (3.23)$$

By assuming that both α and β current dynamics are decoupled and so same controller parameters can be used for both current controllers. Also, control loops include several delay elements such as algorithm processing time, analog to digital conversion time and converter time delays which should be considered while designing controllers. Generally, the delays are considered together as a first order delay element with a time constant which depends on sampling time and PWM pattern. In this study, double update PWM method whose illustration is given in Figure 3.10, is performed.

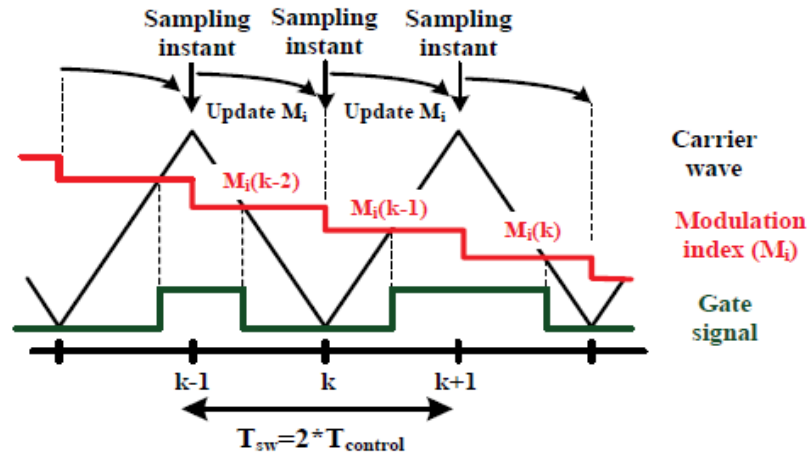


Figure 3.10. Double Update PWM Method [40]

The bandwidth of the current controller is doubled by this method with the cost of decrease in phase margin and larger overshoots. Sampling method has different impacts on the controller based on current feedback methods. If the measured current has unfiltered high frequency ripples like in the CCF, the controller bandwidth is degraded considerably. On the other hand, when GCF is used, the current ripples are attenuated by filter capacitors and controller bandwidth is less affected [40]. In each switching cycle, the sampling and modulation index updating is done twice at the both triangle peaks. Thus, the delay time of the current controller T_{eq} equals to control cycle period which is half of the switching period [57].

Assuming that DC link voltage kept constant by the outer voltage loop controller, variations in the grid voltage becomes the only disturbance signal. The bandwidth and stability phase margin of the PR current controller are determined by the size of the proportional gain K_p as in PI controller. For this reason, while determining the controller parameters, technical or symmetrical optimum methods can be used. The controller parameters designed based on technical optimum provides an optimal response to the step change of reference but can be insufficient while disturbance rejection. For this reason, symmetrical optimum method is used while determining current controller parameters by using simplified LCL filter transfer function. By this

way proportional gain K_p and integral K_i parameters can be evaluated based on Eq. (3.24) and (3.25) where α_i is expressed in terms phase margin ψ in Eq. (3.26) [41].

$$K_p = \frac{L_1+L_2}{\alpha_i T_s} \quad (3.24)$$

$$K_i = \frac{K_p}{\alpha_i^2 T_s} \quad (3.25)$$

$$\alpha_i = \frac{1+\cos\psi}{\sin\psi} \quad (3.26)$$

The phase margin should be maximized in order to have a satisfactory disturbance rejection while providing an acceptable overshoot to the step change of reference [40]. Typically, α_i satisfies the condition given by Eq. (3.27) for a stable operation [45]. For a phase margin larger than 45° , α_i should be 2.4 at least [58]. When α_i equals to 3, the step response settles at 3-4 sampling periods with 4% overshoots [59].

$$2 \leq \alpha_i \leq 3 \quad (3.27)$$

As seen from Figure 3.11, the bandwidth of the current controller can be improved by increasing proportional gain K_p . While analyzing current controller response, LCL filter is considered only L filter because it behaves like a simple inductor at low frequencies. Continuous transfer functions of the filter and current controllers are used while drawing the bode plot. The figure also shows that phase response of the open loop system does not affect from proportional gain change.

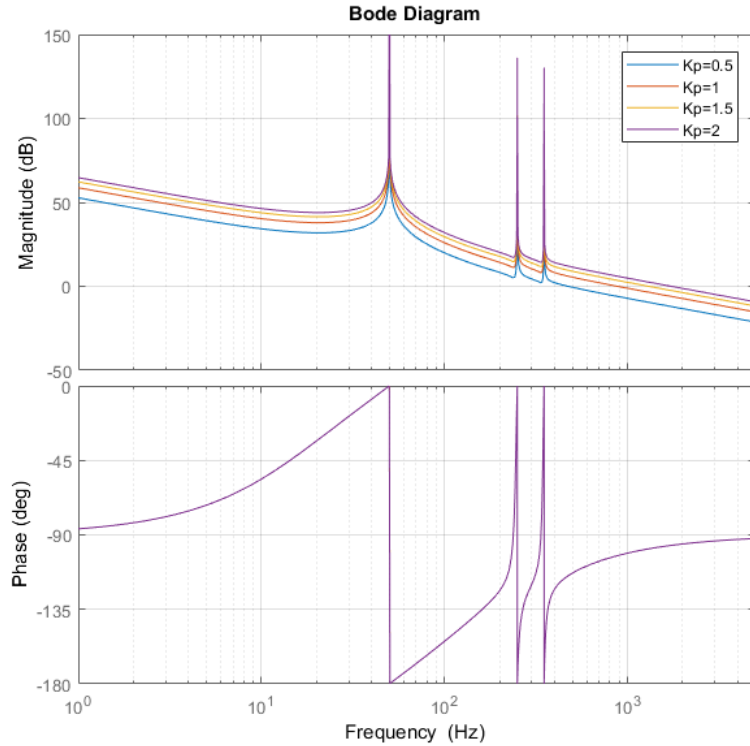
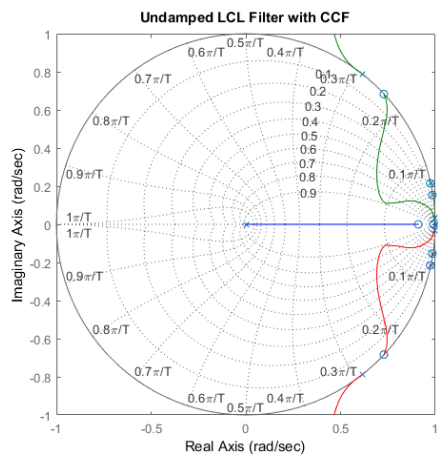
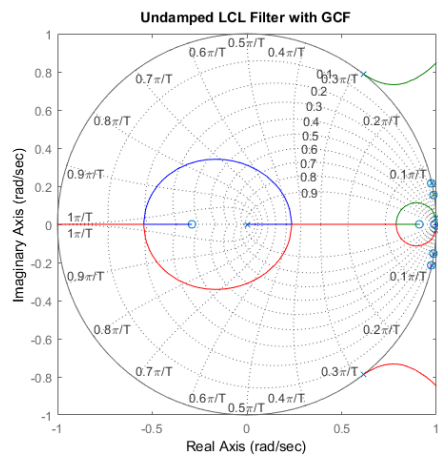


Figure 3.11. Bode Plot of Open Loop PR+HC Current Control System Under Varying K_p

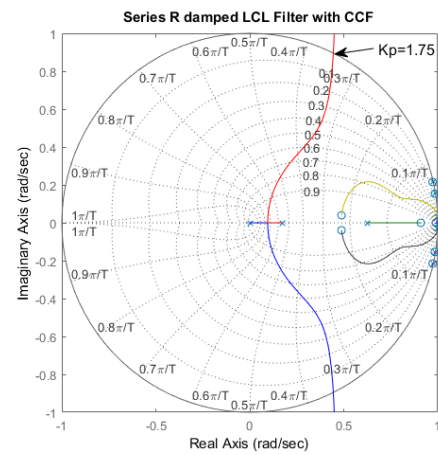
In order to have a stable operation with harmonic compensators, compensation required resonance frequencies should be inside the controller bandwidth. For this reason, larger current controller bandwidth provides better compensation performance. However, increasing current controller gain can cause instabilities because of the high frequency poles of the LCL filter. The root locus analyses are performed based on open loop transfer function of the current controller loop. The analyzed transfer function includes PR+HC current controller, one sample delay element and LCL filter. Discrete z-domain analysis is used to determine the upper limit of the proportional gain. LCL filter and current controller transfer functions are transformed to discrete-time transfer functions by using zero order hold method and one sample delay is considered [45]. The performed root locus graphs are shown in Figure 3.12 for undamped, series R damped and shunt R-C damped LCL filters with grid and converter current feedbacks.



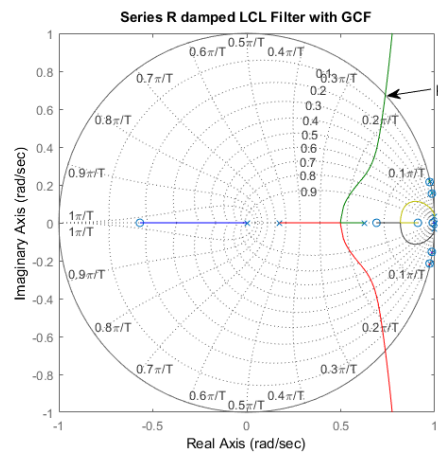
(a)



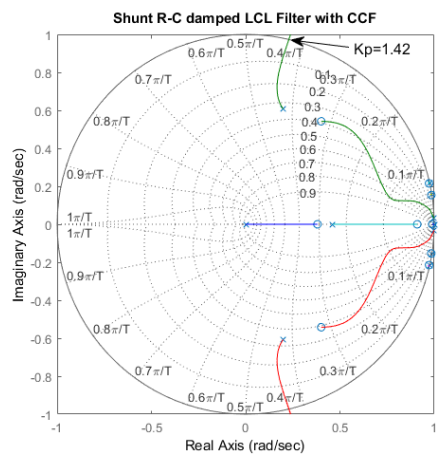
(b)



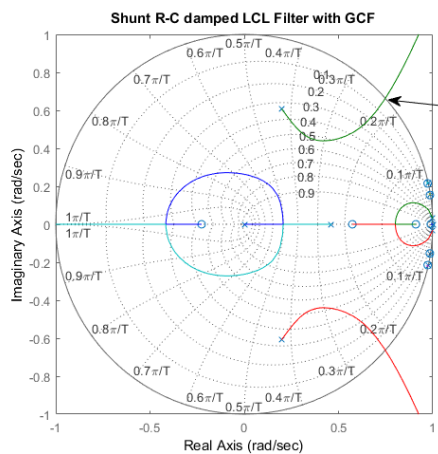
(c)



(d)



(e)



(f)

Figure 3.12. Root Locus Plots of Undamped LCL Filter with CCF (a) and GCF (b), Series R Damped LCL Filter with CCF (c) and GCF (d), Shunt R-C Damped LCL Filter with CCF (e) and GCF (f)

As seen from the root locus plots of undamped cases, the system is always unstable for both current feedbacks. High frequency resonance poles of the LCL filter are placed outside of the unity circle for all gains. When a damping resistor is inserted to filter capacitor, the high frequency poles are attracted inside the unity circle. For both current feedback methods the stability can be provided until a certain K_p value. When converter current feedback is used larger controller bandwidth is provided. Also, it seems that series R damped method is better in terms of controllability but when considered its power losses, shunt R-C damped method can be a better choice. In this study, shunt R-C damped LCL filter will be performed beyond this point. Besides that converter current feedback will be used for current controller. In order to verify the obtained results by root locus and bode plots, nonlinear model which is given in Chapter 1, is used. In the model, a two level three phase IGBT inverter is connected to the grid via shunt R-C damped LCL filter. Outer DC link voltage controller is omitted for stability analysis and a DC voltage source is connected to the DC link by assuming a constant voltage. By keeping the ratio constant between the current controller parameters, K_p is increased until the resonances occur. When K_p is increased from 2.5 to 2.7, current harmonics start to seen at resonance frequency as seen in Figure 3.13. The stability limit obtained by the root locus method was 1.4 for proportional gain K_p . In nonlinear model, all components and conditions are considered as ideal so the stability limit of the system is larger than real one.

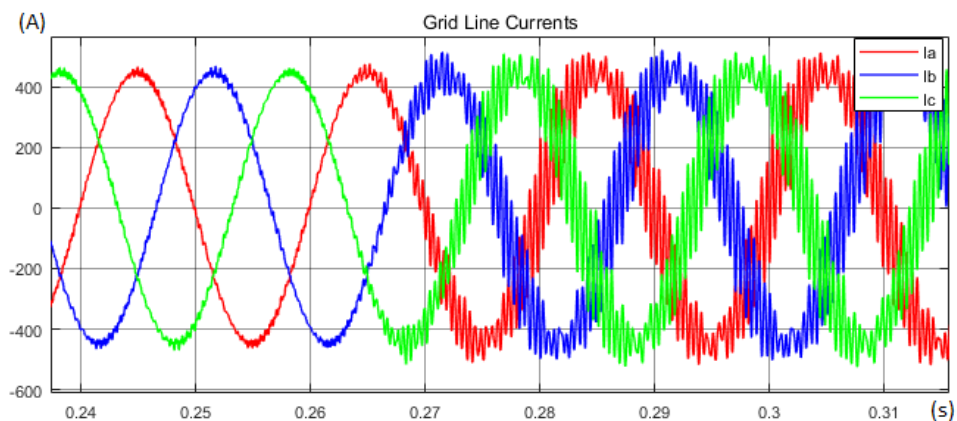


Figure 3.13. Grid Currents at Stability Limits

3.4. Harmonic Compensation

The voltage distortion at PCC and injected grid current distortion are limited by several international standards in order to ensure power system operation with nonlinear loads. IEE519-2014 [50] involves the voltage and current distortion limits of distributed power generation systems. As seen by Table 3.2, distortion limits of individual and total current harmonics are provided for the system from 120 V to 69 kV.

Table 3.2. Current Distortion Limits Determined by IEEE 519-2014 [50]

Maximum harmonic current distortion in percent of I_L						
Individual harmonic order (odd harmonics) ^{a,b}						
I_{SC}/I_L	$3 \leq h < 11$	$11 \leq h < 17$	$17 \leq h < 23$	$23 \leq h < 35$	$35 \leq h \leq 50$	TDD
$< 20^c$	4.0	2.0	1.5	0.6	0.3	5.0
$20 < 50$	7.0	3.5	2.5	1.0	0.5	8.0
$50 < 100$	10.0	4.5	4.0	1.5	0.7	12.0
$100 < 1000$	12.0	5.5	5.0	2.0	1.0	15.0
> 1000	15.0	7.0	6.0	2.5	1.4	20.0

^aEven harmonics are limited to 25% of the odd harmonic limits above.

^aCurrent distortions that result in a dc offset, e.g., half-wave converters, are not allowed.

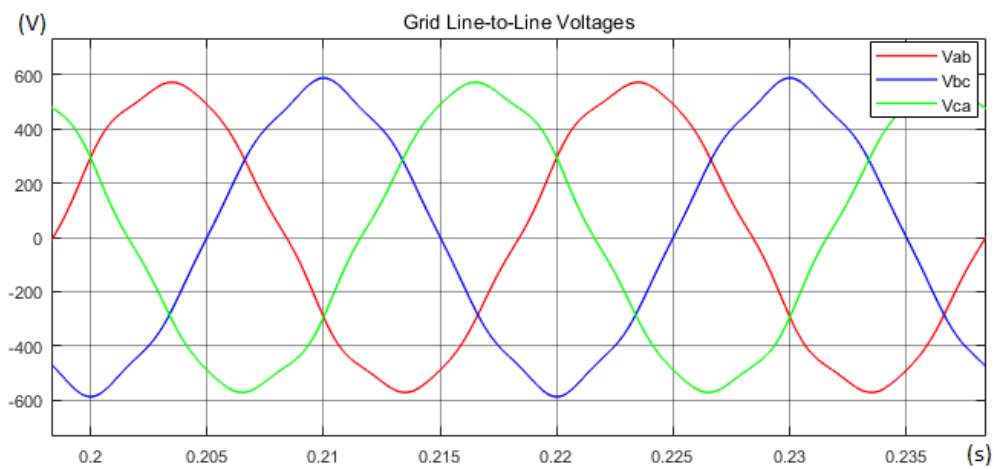
^cAll power generation equipment is limited to these values of current distortion, regardless of actual I_{SC}/I_L where

I_{SC} = maximum short-circuit current at PCC

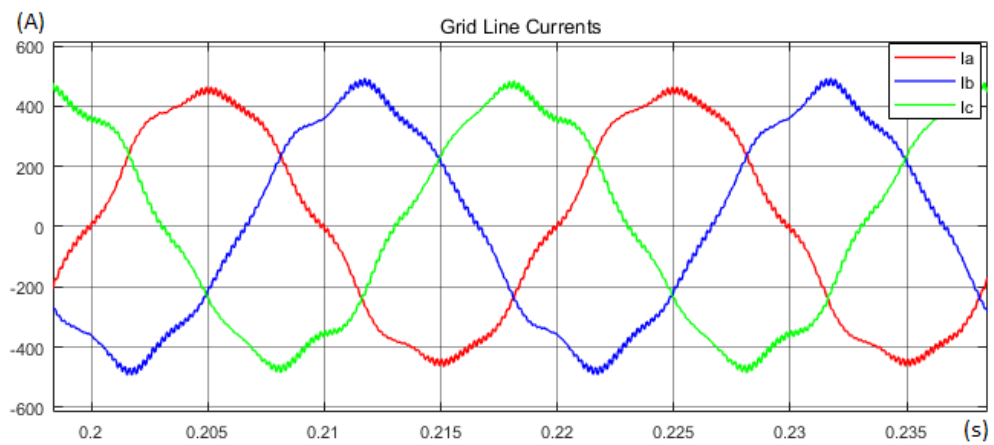
I_L = maximum demand load current (fundamental frequency component) at the PCC under normal load operating conditions

Total Demand Distortion (TDD) is identified as the ratio of root mean square of the harmonic content as a percent of the maximum demand current in IEEE 519-2014. While evaluating harmonic content, harmonic components up to 50th order are considered by excluding interharmonics [50]. According to same standard, Total Harmonic Distortion (THD) is expressed as the ratio of root mean square of the harmonic content as a percent of the fundamental. It can be concluded from these definitions that THD refers to same situation with TDD at full load condition. By considering this situation, the simulations are performed at rated condition by using nonlinear model.

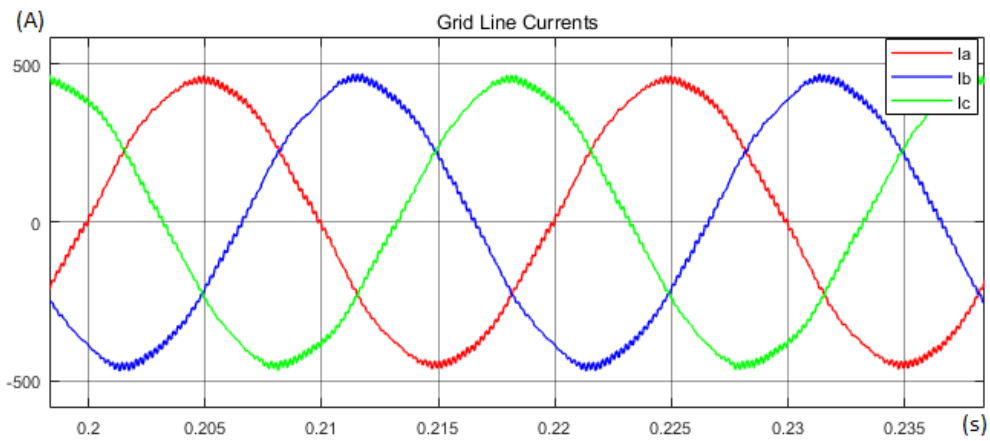
Based on the Table 3.2, it can be said that the TDD of the injected grid current should be smaller than 5%. Also, low frequency harmonics between 3rd and 11th order should be limited at 4% individually. In order to evaluate the performance of the designed controller under distorted grid conditions, the nonlinear model which is given in Appendix B, is used. 5th and 7th harmonic components are added to grid voltage with the amount of 2% of the fundamental voltage. The obtained grid voltages, injected grid currents and Fast Fourier Transform (FFT) analysis results are given in Figure 3.14 for without and with harmonic compensation respectively.



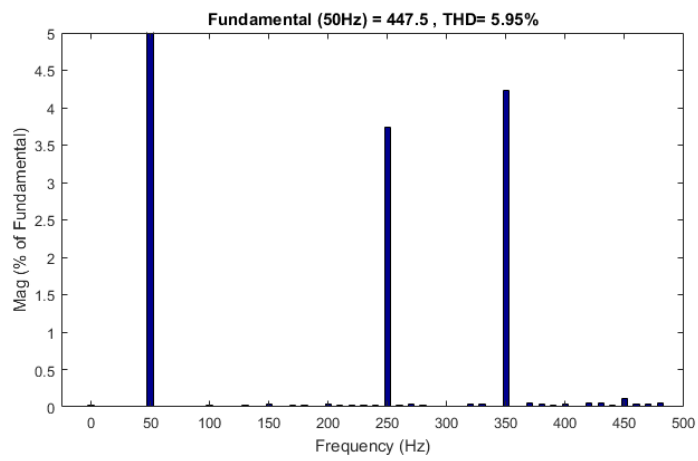
(a)



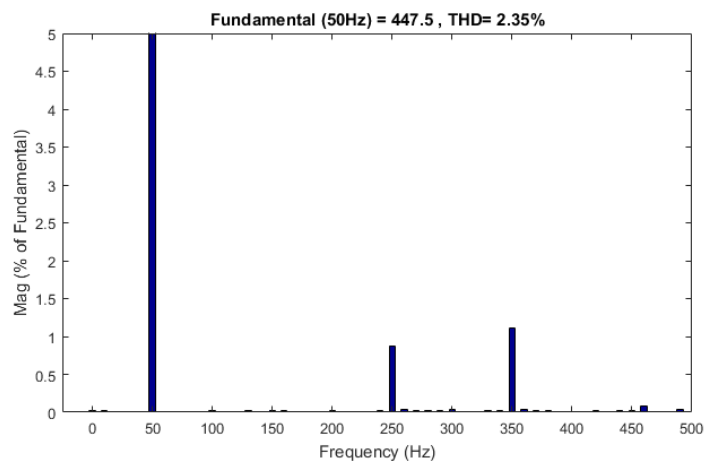
(b)



(c)



(d)



(e)

Figure 3.14. Grid Voltage (a), Grid Currents without (b) and with (c) HC, FFT Analysis of Grid Currents without (d) and with (e) HC

As seen from Figure 3.14, when the grid has 2% voltage distortions at 5th and 7th harmonics and harmonic compensation is not used, the injected grid current THD equals to 5.95% and exceeds the stated limits. Besides that, the individual current distortions of 5th and 7th harmonics are 3.74% and 4.23% of the fundamental voltage and very close to the given limits. By enabling 5th and 7th harmonic compensation, THD of the injected grid current decreased to 2.35%. Individual 5th and 7th harmonic distortions of the grid current improved to 0.88% and 1.1% relative to fundamental component.

3.5. Phase Locked Loop

In order to synchronize with the grid voltage, Phase Locked Loop (PLL) methods are used generally in grid connected VSIs. The phase angle and frequency information of the grid are required for stable operation. Block diagram of a basic PLL is given in Figure 3.15.

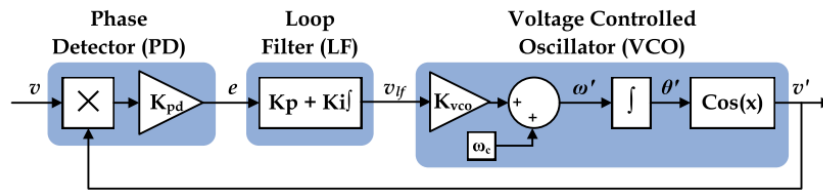


Figure 3.15. Block Diagram of a Basic PLL [60]

The phase detector block generates an error signal based on the phase difference between the input signal v and the output signal v' by using a multiplier. The loop filter focuses on elimination of the phase error and provides a reference signal for voltage controlled oscillator. Due to the multiplier based PD, oscillations occur at twice of the input signal frequency. These oscillations passed through the system and seen at the output signal too [14].

In order to remove the double frequency oscillations, more advanced phase detectors which include adaptive filtering or quadrature signal generation is required. Three phase PLL structures like three phase enhanced PLL (EPLL), Double Second Order Generalized Integrator PLL (DSOGI-PLL) and Decoupled Double Synchronous

Reference Frame PLL (DDSRF-PLL) are developed in [60] with extracting positive sequence to improve the performance. In this study DSOGI-PLL is performed and its structure is shown in Figure 3.16. Thanks to extra filtering feature, DSOGI-PLL provides less oscillations during transients but it can cause some overshoots.

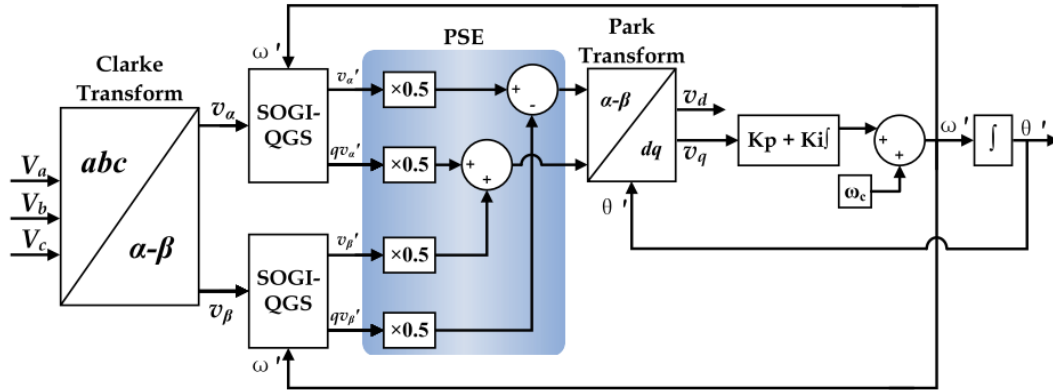


Figure 3.16. Structure of DSOGI-PLL [61]

A pair of SOGI based adaptive filters whose structure is shown in Figure 3.17, generates the in-quadrature signals of the $\alpha\beta$ stationary reference frame voltages.

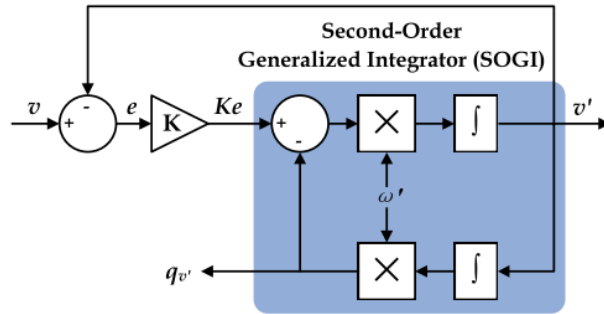


Figure 3.17. Structure of the SOGI [60]

The transfer functions of the SOGI structure is derived in [60] as in Eq. (3.28)-(3.33).

$$SOGI(s) = \frac{v'}{v}(s) = \frac{\omega's}{s^2 + \omega^2} \quad (3.28)$$

$$DSOGI(s) = \frac{qv'}{v}(s) = \frac{K\omega's}{s^2 + K\omega's + \omega^2} \quad (3.29)$$

$$Q_{SOGI}(s) = \frac{q_{v'}}{v}(s) = \frac{K\omega'^2}{s^2 + K\omega's + \omega^2} \quad (3.30)$$

$$\angle D_{SOGI} = \tan^{-1}\left(\frac{\omega'^2 - \omega^2}{K\omega'\omega}\right) \quad (3.31)$$

$$\angle Q_{SOGI} = \tan^{-1}\left(\frac{-K\omega'\omega}{\omega'^2 - \omega^2}\right) \quad (3.32)$$

$$\Rightarrow \angle Q_{SOGI} = \angle D_{SOGI} - \pi/2 \quad (3.33)$$

It is concluded from Eq. (3.33) that v' and $q_{v'}$ are in-quadrature signals and thus adaptive filter based SOGI may be used to perform Quadrature Signal Generation (QSG). From Eq. (3.29) and (3.30), it can be said that bandwidth of the SOGI based adaptive filter is only dependent to gain K . Besides, when the input frequency ω matches with the center frequency ω' , the magnitude of v' and $q_{v'}$ match the with magnitude of the input signal v and thus, implementation of the Park Transform becomes possible [60]. Positive sequence components of the in-quadrature signals are extracted and transformed to dq synchronously rotating reference frame. The transformations between reference frames (Park, Clarke, Inverse Park and Inverse Clarke Transforms) are given in Appendix A. Either v_d or v_q can be given to loop filter for different alignments at steady state. As seen in Figure 3.16, v_q is chosen and connected to loop filter so θ is equal to θ' at steady state and virtual input vector \vec{V} is aligned with the d axis. At this condition, PLL detected phase is synchronized with the virtual input vector \vec{V} whose amplitude is provided by v_d . In other words, sinusoidal input signal phase is 90° ahead of the PLL detected phase. Therefore, active and reactive power control become possible [14].

The performance of the synchronization system is effected from the utility network distortions [62]–[65]. The dynamic of the synchronization algorithm is directly related to filter bandwidth of the PLL. If the synchronization time is kept minimum in order to achieve fast dynamic response, distortions in the input signal is not filtered well and reflected to output signal. Increasing settling time provides a more filtered and stable output signal. Thus, while designing the system, the purpose should be considered

well. A fast dynamic system is required for grid monitoring and fault detection. On the other hand, a slow dynamic system should be employed to synchronize the control variables with grid voltage vectors [27].

A loop filter was introduced at the output of DSOGI-PLL. At this part, design of this filter is given by considering weak grid conditions. In order to determine PI gain parameters, input error signal should be normalized. Otherwise, the determined parameters should be divided to the amplitude of input error signal [14].

The frequency domain transfer function of the second order output filter is given by Eq. (3.34) where K_p and K_i represent gain and integral time constants [27].

$$H(s) = \frac{K_p s + \frac{K_p}{T_i}}{s^2 + K_p s + \frac{K_p}{T_i}} \quad (3.34)$$

A standard second order transfer function with a zero is given by Eq. (3.35) where ζ is damping factor and ω_n is natural frequency.

$$G(s) = \frac{2\zeta\omega_n s + \omega_n^2}{s^2 + 2\zeta\omega_n s + \omega_n^2} \quad (3.35)$$

Thus, the controller parameters of the filter can be derived as Eq. (3.36) and (3.37) where T_s represents settling time of the filter response. The relation between settling time T_s , damping factor ζ and natural frequency ω_n is given by Eq. (3.38). Bandwidth of the PLL system is given by Eq. (3.39) based on damping factor ζ and natural frequency ω_n [14].

$$K_p = \frac{9.2}{T_s} \quad (3.36)$$

$$T_i = \frac{T_s \zeta^2}{2.3} \quad (3.37)$$

$$\omega_n = \frac{4.6}{\zeta T_s} \quad (3.38)$$

$$\omega_{bw} = \omega_n \sqrt{1 + 2\zeta^2 + \sqrt{(1 + 2\zeta)^2 + 1}} \quad (3.39)$$

Step responses of the PLL system with damping factors ζ from 0.5 to 1 are shown in Figure 3.18. Lower values of damping factor ζ cause higher overshoots and higher values of damping factor ζ bring larger settling times. According to [66], damping factor $\zeta = 0.707$ gives optimum step response with 20% overshoot.

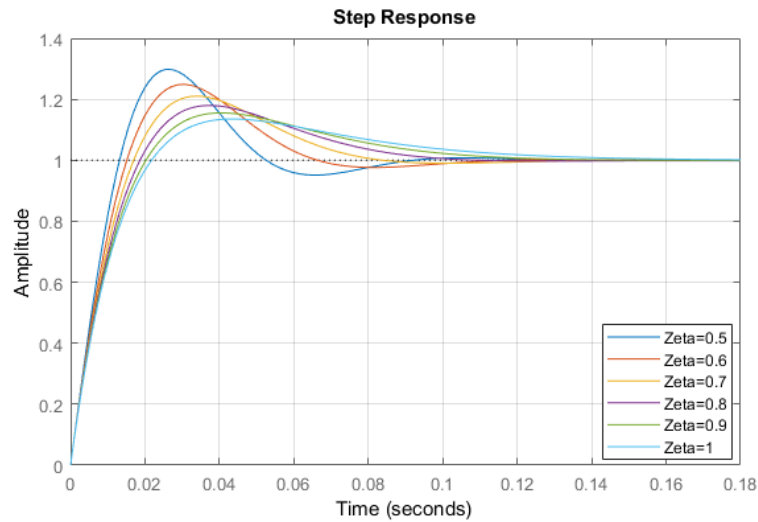


Figure 3.18. Step Response of the PLL System with Damping Factors ζ from 0.5 to 1

Bode plots of the PLL system with settling times T_s from 0.1 to 0.5 are shown in Figure 3.19.

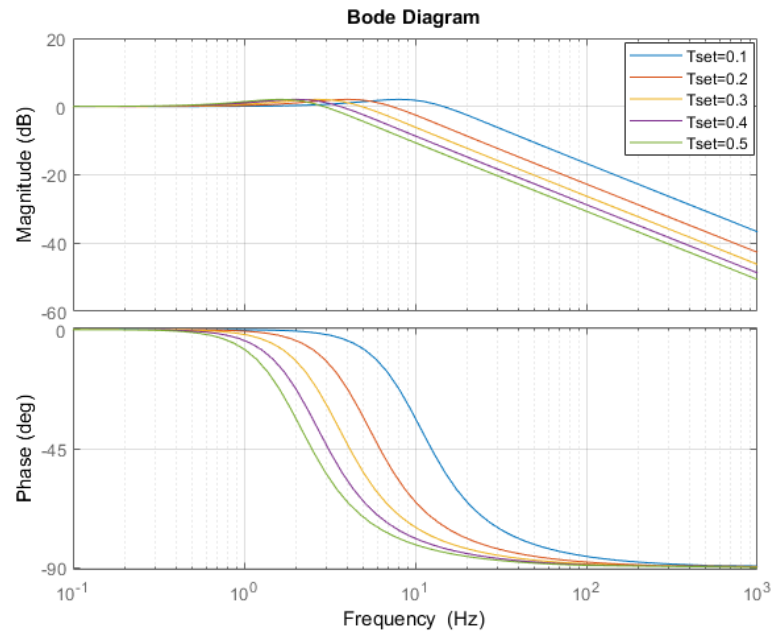


Figure 3.19. Bode Plots of the PLL System with Settling Times T_s from 0.1 to 0.5

Based on Figure 3.19 and Eq. (3.39), it is seen that higher values of settling time provide lower controller bandwidths and better filtering performance at high frequencies for PLL systems. Besides that, bandwidth of the PLL should be high enough in order to have a fast transient response. However, instabilities occur at very low PLL bandwidths under weak grid conditions. Settling time T_s is recommended as 0.1 s in [14] in order to have optimum PLL response under ideal grid conditions.

3.6. Summary

In this chapter, overall controller design of grid side converter and LCL filter structures are explained in detail. Firstly, design procedure of LCL filter is given by analyzing pole zero map in order to determine optimum damping resistance value. Secondly, outer DC voltage loop is investigated and its controller parameter selection is explained. After that, PR current controller with HC is designed by considering the stability of the plant. While determining appropriate parameter values discrete root locus analysis is performed. The open loop transfer function of the plant is derived by considering the responses of LCL filter, current controller and delays caused by PWM and controller. Obtained transfer function is discretized by using the sampling time of the controller and stability limits are determined on the unit circle. Lastly, DSOGI-PLL structure is given and its parameters are selected. DSOGI-PLL provides less oscillations during transients than regular PLL structures thanks to the loop filter placed at the output. Bandwidth of the filter determines the response behavior of the PLL. Lower PLL bandwidth provides more filtering feature and causes slower system response. Thus, the system provides stable operation under weak grid condition.

CHAPTER 4

IMPEDANCE BASED STABILITY ANALYSIS

The amount of distributed power generation systems which are connected to the grid is increasing day by day. These generation systems produce high frequency voltage and current signals and require more attention than conventional generation systems for stable operation. The renewable energy resources are generally located in remote areas and requires long cables for the connection with the grid which bring a significant amount of grid impedance and creates impedance mismatches between grid and inverter [67].

Impedance based stability analysis focuses on the stable operation of grid connected inverter by considering grid and inverter output impedances [68]. According to the method, the ratio of the inverter output impedance to the grid impedance must satisfy the Nyquist stability criterion to maintain a stable operation. The method requires a detailed analysis by using controller model and steady state operating points.

4.1. Impedance Based Stability Criterion

In order to perform impedance based stability analysis, equivalent circuit of the grid connected inverter system is considered as given in Figure 4.1. In this circuit, grid connected inverter is modeled with Norton equivalent as a current source with parallel impedance. On the other side, the grid is modeled with Thevenin equivalent as a voltage source with series impedance [5].

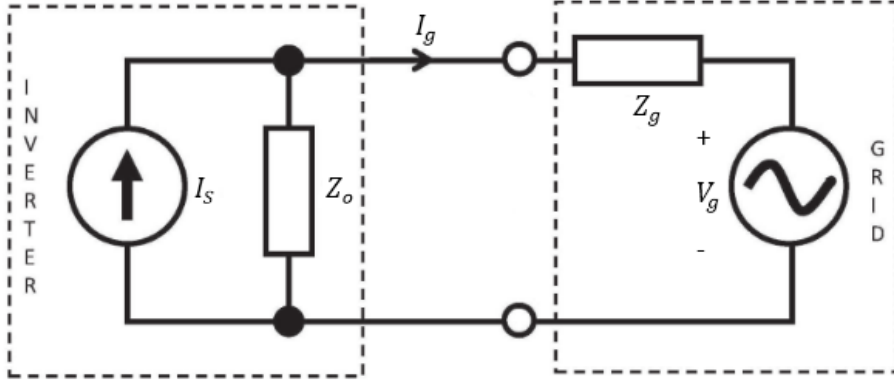


Figure 4.1. Equivalent Circuit of the Grid Connected Inverter System [69]

The grid current I_g determines the stability of the system and evaluated as given in Eq. (4.1) where Z_o represents inverter output impedance as a source impedance, Z_g is grid impedance as a load impedance with source current I_s and grid voltage V_g [69], [70].

$$I_g = \frac{I_s Z_o - V_g}{Z_g + Z_o} = \left(I_s - \frac{V_g}{Z_o} \right) * \frac{1}{1 + \frac{Z_g}{Z_o}} \quad (4.1)$$

Inverter output impedance is calculated from the developed model and the grid impedance is measured at real time. While performing analysis, some assumptions are made [70]:

- The grid is stable without inverter and so V_g/Z_o is always stable.
- The inverter is stable when the grid impedance is zero so I_s is always stable.

With these assumptions, $1/(1 + Z_g/Z_o)$ is the last term of Eq. (4.1) and considered for impedance based stability analysis. Nyquist stability criterion or Bode plot can be used while performing the stability analysis. Nyquist stability criterion states that if the Nyquist curve of Z_g/Z_o does not encircle the point (-1,0) in the complex plane, the system is stable [71]. If the Bode plot is preferred for stability analysis, frequency responses of the Z_g and Z_o is plotted. If the phase difference between the source and load impedance is smaller than 180° at the overlap point of the magnitude responses, the system is stable [69].

For stability analysis, the system is transformed from three-phase natural frame to stationary dq domain by using the transformations which are given in Appendix A. The transformation introduces cross-coupling terms (dq and qd) between the individual components. However, they are small when compared with individual components and so can be neglected for unity power factor operation [72], [73]. At lower power factor values the cross-coupling terms should be considered to avoid inaccuracy.

The impedance of the grid is modeled by using resistance and inductance at frequencies lower than 1 kHz [74]. For both d and q reference frames, the grid impedance is assumed as given by Eq. (4.2) where Z_g is measured grid impedance, R_g and L_g represent the resistance and inductance of the grid respectively [73].

$$Z_g(s) = Z_{g-dd}(s) = Z_{g-qq}(s) = R_g + sL_g \quad (4.2)$$

The transfer functions which are used for stability analysis are given by Eq. (4.3) and (4.4) for d and q reference frames where Z_{o-dd} and Z_{o-qq} represent the output impedance of the inverter in d and q reference frames.

$$G_{dd}(s) = \frac{1}{1+Z_g(s)/Z_{o-dd}(s)} \quad (4.3)$$

$$G_{qq}(s) = \frac{1}{1+Z_g(s)/Z_{o-qq}(s)} \quad (4.4)$$

4.2. Analytical Inverter Model

Grid connected three-phase voltage source inverter system fed by a current source is given by Figure 4.2. In order to simplify the equations while deriving average model, the inverter is considered with only inverter side inductance and output admittance of the inverter is derived. After that admittance of the capacitor branch is taken into account and output admittance of the whole inverter system is achieved analytically.

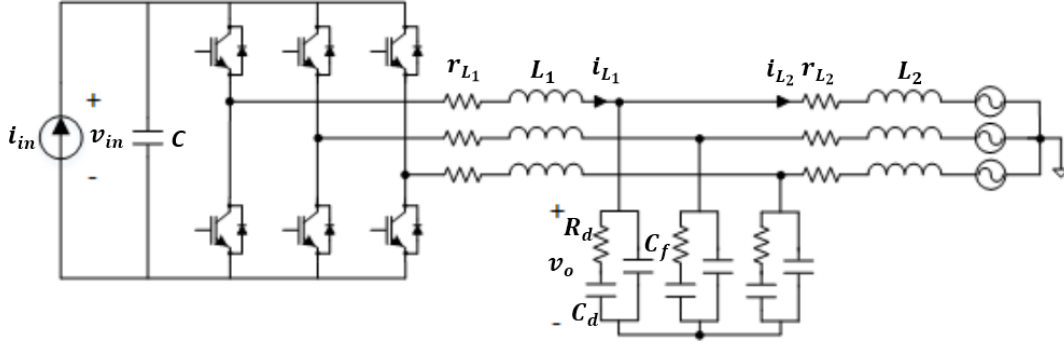


Figure 4.2. Grid Connected Three-Phase Voltage Source Inverter System

4.2.1. Small Signal Model

The average model of the inverter system is derived as given by Eq. (4.5), (4.6) and (4.7) where d represents the duty ratio of the switching devices over the one period, r_{L1} is the resistance of the phase inductor L_1 , C represents DC link capacitor, ω_s is the angular frequency of the fundamental grid voltage, i_{in} and v_{in} are the DC current and voltage. AC voltages and currents are expressed in dq reference frame. v_{od} and v_{oq} represent the voltage of filter capacitor, i_{L1d} and i_{L1q} are used for currents of phase inductor [5], [69].

$$\frac{d\langle i_{L1d} \rangle}{dt} = \frac{1}{L_1} (-r_{L1} \langle i_{L1d} \rangle + \omega_s L_1 \langle i_{L1q} \rangle + d_d \langle v_c \rangle - \langle v_{od} \rangle) \quad (4.5)$$

$$\frac{d\langle i_{L1q} \rangle}{dt} = \frac{1}{L_1} (-\omega_s L_1 \langle i_{L1d} \rangle - r_{L1} \langle i_{L1q} \rangle + d_q \langle v_c \rangle - \langle v_{oq} \rangle) \quad (4.6)$$

$$\frac{d\langle v_c \rangle}{dt} = \frac{1}{C} \left(\langle i_{in} \rangle - \frac{3}{2} (d_d \langle i_{L1d} \rangle + d_q \langle i_{L1q} \rangle) \right) \quad (4.7)$$

Steady-state operating point of the inverter system is solved by using the average model equations. For this purpose, the derivative terms in the equations are set to zero and capital letters are used for the values of variables in steady-state. Duty ratio q component D_q is derived as given by Eq. (4.10) using Eq. (4.6). The obtained duty ratio q component D_q is substituted in Eq. (4.7) and d component of the phase inductor current I_{L1d} is obtained as given by Eq. (4.9). Lastly, the obtained I_{L1d} value is

substituted in Eq. (4.5) and a second order polynomial is obtained as given by Eq. (4.8) [5].

$$V_{in}^2 D_d^2 + V_{in}(2\omega_s L_1 I_{L1q} - V_{od})D_d + (r_{L1}^2 + \omega_s^2 L_1^2)I_{L1q}^2 + r_{L1}(V_{oq}I_{L1q} - \frac{2}{3}V_{in}I_{in}) - \omega_s L_1 V_{od}I_{L1q} = 0 \quad (4.8)$$

$$I_{L1d} = \frac{(2/3)V_{in}I_{in} - V_{oq}I_{L1q} - r_{L1}I_{L1q}^2}{D_d V_{in} + \omega_s L_1 I_{L1q}} \quad (4.9)$$

$$D_q = \frac{V_{oq} + r_{L1}I_{L1q} + \omega_s L_1 I_{L1d}}{V_{in}} \quad (4.10)$$

Steady state value of the phase inductor current q component I_{L1q} does not depend on the injected power from the generator side and equals to reference value given by Eq. (4.11) in order to compensate the reactive power drawn by the filter capacitors and operate unity power factor at PCC [5]. While determining the reference value I_{L1q}^* , it is assumed that steady-state q component of the output voltage V_{oq} is set equals zero by PLL and damping resistor R_d is neglected because it is relatively small when compared with filter capacitor impedance at the natural frequency of the grid voltage.

$$I_{L1q} = I_{L1q}^* \cong \omega_s (C_d + C_f) * V_{od} \quad (4.11)$$

When the given conditions are considered, the steady-state operating point at unity power factor is determined by solving Eq. (4.8), (4.9) and (4.10) [5]. V_{in} and I_{in} are the inputs for equations and determined from the source. The other input V_{od} is obtained from the grid voltage. Eq. (4.8) is a second order polynomial and has two solutions. The solution which satisfies the condition given by Eq. (4.12) is used for the further equations.

$$0 < D_d < 1 \quad (4.12)$$

First order partial derivatives of each input and state variable are performed in order to linearize the average model of the system. The obtained equations are given by Eq. (4.13), (4.14) and (4.15) [5].

$$\frac{d\hat{i}_{L1d}}{dt} = -\frac{r_{L1}}{L_1}\hat{i}_{L1d} + \omega_s\hat{i}_{L1q} + \frac{D_d}{L_1}\hat{v}_c - \frac{1}{L_1}\hat{v}_{od} + \frac{V_c}{L_1}\hat{d}_d \quad (4.13)$$

$$\frac{d\hat{i}_{L1q}}{dt} = -\omega_s \hat{i}_{L1d} - \frac{r_{L1}}{L_1} \hat{i}_{L1q} + \frac{D_q}{L_1} \hat{v}_c - \frac{1}{L_1} \hat{v}_{oq} + \frac{V_{in}}{L_1} \hat{d}_q \quad (4.14)$$

$$\frac{d\hat{v}_c}{dt} = -\frac{3}{2} \frac{D_d}{C} \hat{i}_{L1d} - \frac{3}{2} \frac{D_q}{C} \hat{i}_{L1q} + \frac{1}{C} \hat{i}_{in} - \frac{3}{2} \frac{I_{L1d}}{C} \hat{d}_d - \frac{3}{2} \frac{I_{L1q}}{C} \hat{d}_q \quad (4.15)$$

Input, output and state variables are expressed as \mathbf{u} , \mathbf{y} and \mathbf{x} vectors while the constants are given as \mathbf{A} , \mathbf{B} , \mathbf{C} and \mathbf{D} matrices in Eq. (4.16) and (4.17) [5], [69].

$$\frac{d}{dt} \begin{bmatrix} \hat{i}_{L1d} \\ \hat{i}_{L1q} \\ \hat{v}_c \end{bmatrix} = \begin{bmatrix} \frac{-r_{L1}}{L_1} & \omega_s & \frac{D_d}{L_1} \\ -\omega_s & \frac{-r_{L1}}{L_1} & \frac{D_q}{L_1} \\ -\frac{3}{2} \frac{D_d}{C} & -\frac{3}{2} \frac{D_q}{C} & 0 \end{bmatrix} \begin{bmatrix} \hat{i}_{L1d} \\ \hat{i}_{L1q} \\ \hat{v}_c \end{bmatrix} + \begin{bmatrix} 0 & -\frac{1}{L_1} & 0 & \frac{V_{in}}{L_1} & 0 \\ 0 & 0 & -\frac{1}{L_1} & 0 & \frac{V_{in}}{L_1} \\ \frac{1}{C} & 0 & 0 & -\frac{3}{2} \frac{I_{L1d}}{C} & -\frac{3}{2} \frac{I_{L1q}}{C} \end{bmatrix} \begin{bmatrix} \hat{i}_{in} \\ \hat{v}_{od} \\ \hat{v}_{oq} \\ \hat{d}_d \\ \hat{d}_q \end{bmatrix} \quad (4.16)$$

$$\frac{d}{dt} \begin{bmatrix} \hat{v}_{od} \\ \hat{v}_{oq} \\ \hat{v}_{in} \end{bmatrix} = \begin{bmatrix} 1 & 0 & 0 \\ 0 & 1 & 0 \\ 0 & 0 & 1 \end{bmatrix} \begin{bmatrix} \hat{i}_{L1d} \\ \hat{i}_{L1q} \\ \hat{v}_c \end{bmatrix} + \begin{bmatrix} 0 & 0 & 0 & 0 & 0 \\ 0 & 0 & 0 & 0 & 0 \\ 0 & 0 & 0 & 0 & 0 \end{bmatrix} \begin{bmatrix} \hat{i}_{in} \\ \hat{v}_{od} \\ \hat{v}_{oq} \\ \hat{d}_d \\ \hat{d}_q \end{bmatrix} \quad (4.17)$$

Eq. (4.16) and (4.17) are transformed to frequency domain by using Laplace transform and the input to output transfer matrix \mathbf{G} is obtained as given by Eq. (4.18) where \mathbf{I} represents identity matrix [71].

$$\mathbf{Y}(s) = \mathbf{G}\mathbf{U}(s) = [\mathbf{C}(s\mathbf{I} - \mathbf{A})^{-1}\mathbf{B}]\mathbf{U}(s) \quad (4.18)$$

The input to output transfer matrix \mathbf{G} includes 15 different open loop transfer functions as given by Eq. (4.19) where Z and Y represent impedance and admittance, T and A are voltage to voltage and current to current transfer functions. G shows the effect of duty ratio. Subscripts ‘-o’ is used for open-loop functions, ‘i’ and ‘o’ represent input and output, ‘c’ means control, ‘d’ and ‘q’ shows dq frame components and lastly ‘dq’ and ‘qd’ are used for cross coupling terms [69].

$$\underbrace{\begin{bmatrix} \hat{i}_{od} \\ \hat{i}_{oq} \\ \hat{v}_{in} \end{bmatrix}}_{\mathbf{Y}} = \underbrace{\begin{bmatrix} A_{iod-o} & -Y_{d-o} & -Y_{dq-o} & G_{cod-o} & G_{codq-o} \\ A_{ioq-o} & -Y_{qd-o} & -Y_{q-o} & G_{coqd-o} & G_{coq-o} \\ Z_{in-o} & T_{iod-o} & T_{ioq-o} & G_{cid-o} & G_{ciq-o} \end{bmatrix}}_{\mathbf{G}} \cdot \underbrace{\begin{bmatrix} \hat{i}_{in} \\ \hat{v}_{od} \\ \hat{v}_{oq} \\ \hat{d}_d \\ \hat{d}_q \end{bmatrix}}_{\mathbf{U}} \quad (4.19)$$

4.2.2. Controller Transfer Functions

The controller design of the grid connected inverter system was performed at Chapter 3. In this part, transfer functions of current controller, DC voltage controller and PLL system are evaluated in dq reference frame for the stability analysis.

DC voltage controller design was presented at Section 3.2. PI controller whose transfer function G_{PI-dc} is given by Eq. (4.20) is used to stabilize the DC link voltage at a determined value. For this purpose, active current reference of the current controller is set by the outer DC voltage loop.

$$G_{PI-dc} = K_{p-dc} + \frac{K_{i-dc}}{s} \quad (4.20)$$

In the grid connected inverter system, PR controller is used as a current controller in $\alpha\beta$ stationary reference frame. However, current controller is expressed as a PI controller for stability analysis, because PI and PR controllers show same performance at steady state in their reference frames [75]. The effects of harmonic compensators are ignored for the analysis. The transfer function of the current controller G_{PI} is given by Eq. (4.21).

$$G_{PI} = K_p + \frac{K_i}{s} \quad (4.21)$$

As presented in Section 3.4 DSOGI-PLL is used in the designed controller. For the stability analysis, basic synchronous reference frame PLL (SRF-PLL) whose block diagram is shown by Figure 4.3, will be considered.

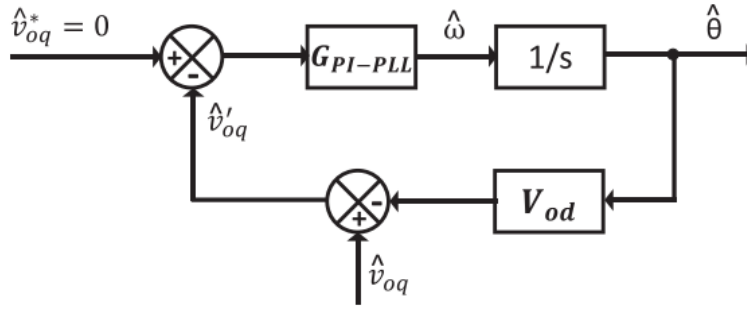


Figure 4.3. Block Diagram of the SRF-PLL [69]

Basically, the measured grid voltages are transformed to dq reference frame and PI controller is performed by the PLL in order to generate the angular frequency of the grid. An integrator is used to develop the phase angle information from the angular frequency. The reference for the q component of the grid voltage is set to zero for ideal grid synchronization. The transfer function of the PI controller used for PLL G_{PI-PLL} is given by Eq. (4.22).

$$G_{PI-PLL} = K_{p-pll} + \frac{K_{i-pll}}{s} \quad (4.22)$$

The loop gain of PLL is given by Eq. (4.23) for the given conditions.

$$L_{PLL} = \left(-\frac{V_{od}}{s}\right) G_{PI-PLL} \quad (4.23)$$

At the end, close loop transfer function of the PLL system is derived as Eq. (4.24) [69].

$$G_{PLL} = \frac{1}{V_{od}} \left(\frac{L_{PLL}}{1+L_{PLL}} \right) \quad (4.24)$$

4.3. Inverter Output Impedance

For stability analysis, d and q components of the output impedance are considered separately because they have different dynamic behaviours. DC voltage controller has an impact only on d component while grid synchronization is affecting only q component [5]. At this part, by using the generated analytical inverter model, transfer functions of the inverter output impedance will be derived.

4.3.1. Impedance d Component

A cascaded control scheme is performed to operate the grid connected inverter. Outer DC voltage control loop sets the d component of the inner current loop. In order to derive inverter impedance d component, cascaded control scheme should be analyzed in detail. First, the closed loop dynamics of the inner current control loop will be solved and secondly outer DC voltage loop will be added to the model [5].

Reduced order open loop transfer functions with current controller model is given by Figure 4.4. In this model, cross-coupling transfer functions Y_{oqd-o} and G_{coqd-o} are neglected and the gains for sensor and PWM modulator are assumed unity. Input dynamics mainly depend on real power so T_{ioq-o} and G_{ciq-o} are neglected also [76].

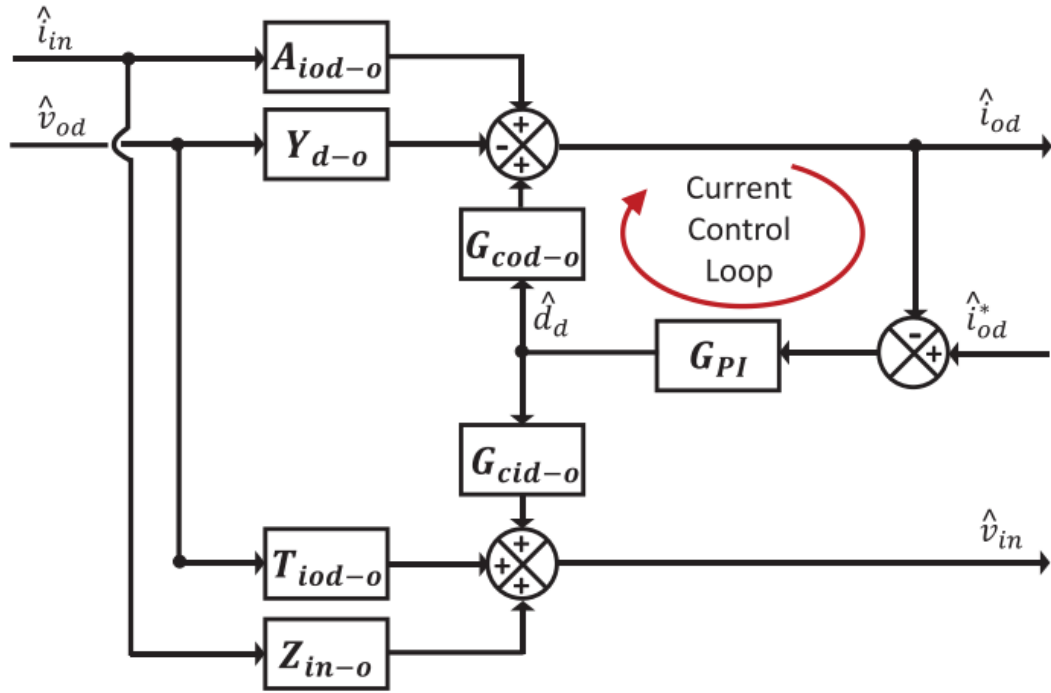


Figure 4.4. The d Component Open Loop Transfer Functions with Current Control [69]

Closed loop transfer functions are solved from Figure 4.4 and defined as in Eq. (4.25) – (4.31) where subscript ‘cl’ is used for the closed loop transfer functions [5].

$$L_{out-d} = G_{PI}G_{cod-o} \quad (4.25)$$

$$A_{iod-cl} = \frac{\hat{i}_{od}}{\hat{i}_{in}} = \frac{A_{iod-o}}{(1+L_{out-d})} \quad (4.26)$$

$$G_{cod-cl} = \frac{\hat{i}_{od}}{\hat{i}_{od}^*} = \frac{L_{out-d}}{(1+L_{out-d})} \quad (4.27)$$

$$Y_{d-cl} = -\frac{\hat{i}_{od}}{\hat{v}_{od}} = \frac{Y_{d-o}}{(1+L_{out-d})} \quad (4.28)$$

$$Z_{in-cl} = \frac{\hat{v}_{in}}{\hat{i}_{in}} = \frac{Z_{in-o}}{(1+L_{out-d})} + \frac{L_{out-d}}{(1+L_{out-d})} \left(Z_{in-o} - \frac{G_{cid-o}A_{iod-o}}{G_{cod-o}} \right) \quad (4.29)$$

$$T_{iod-cl} = \frac{\hat{v}_{in}}{\hat{v}_{od}} = \frac{T_{iod-o}}{(1+L_{out-d})} + \frac{L_{out-d}}{(1+L_{out-d})} \left(T_{iod-o} - \frac{G_{cid-o}Y_{d-o}}{G_{cod-o}} \right) \quad (4.30)$$

$$G_{cid-cl} = \frac{\hat{v}_{in}}{\hat{i}_{od}^*} = \frac{G_{cid-o}}{G_{cod-o}} \frac{L_{out-d}}{(1+L_{out-d})} \quad (4.31)$$

The derived closed loop transfer functions with current control are used as open loop transfer functions while analyzing the outer voltage loop. The control scheme with closed loop transfer functions and DC voltage control is given in Figure 4.5.

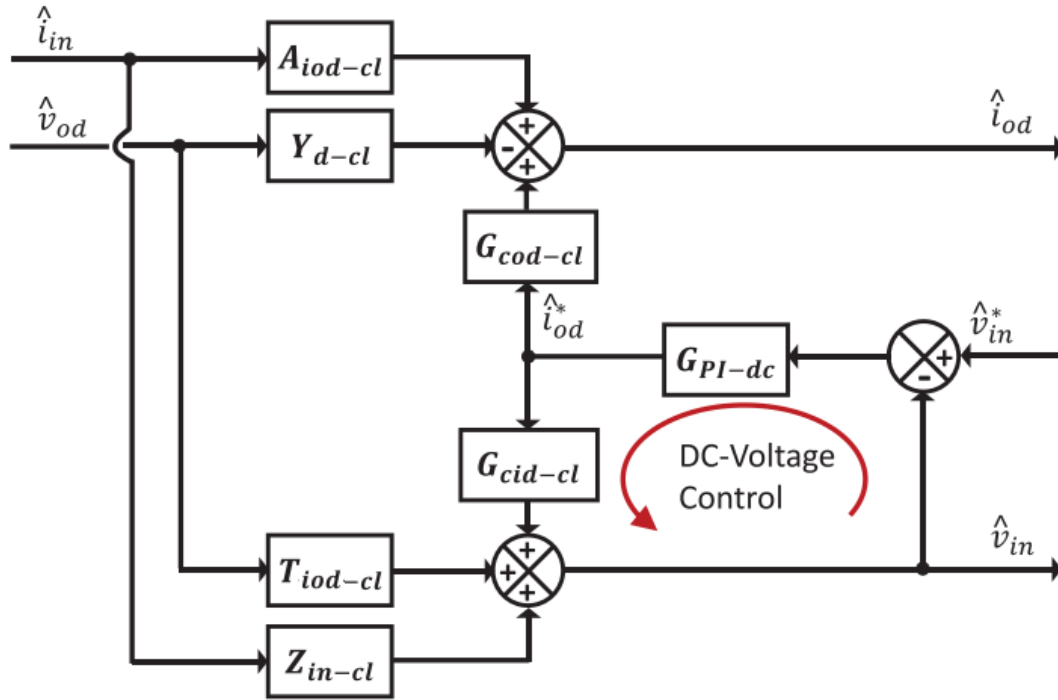


Figure 4.5. The d Component Closed Loop Transfer Functions with DC Voltage Control [69]

The DC voltage control loop gain and d component output admittance of the inverter are solved from Figure 4.5 as in Eq. (4.32) and (4.33) [5].

$$L_{in} = -G_{PI-dc}G_{cid-cl} = -\frac{G_{cid-o}}{G_{cod-o}}\frac{L_{out-d}}{(1+L_{out-d})}G_{PI-dc} \quad (4.32)$$

$$Y_{out-d} = -\frac{\hat{i}_{od}}{\hat{v}_{od}} = Y_{d-cl} + \frac{T_{iod-cl}G_{PI-dc}G_{cod-cl}}{(1+L_{in})} \quad (4.33)$$

By substituting the closed loop transfer functions from Eq. (4.25) to (4.31) into the Eq. (4.33), d component output admittance transfer function is simplified as in Eq. (4.34).

$$Y_{out-d} = \frac{Y_{d-o}}{(1+L_{in})(1+L_{out-d})} + \frac{L_{in}}{(1+L_{in})}\left(Y_{d-o} + \frac{G_{cod-o}T_{iod-o}}{G_{cid-o}}\right) \quad (4.34)$$

While deriving the transfer function given by Eq. (4.34), only inverter side inductor was considered. In order to find output admittance for overall system, admittance of the filter capacitor branch for R-C shunt damped LCL filter whose admittance Y_c is given by Eq. (4.35), must be taken into account.

$$Y_c = \frac{1}{\left(\frac{1}{sC_d} + R_d\right) // \frac{1}{sC_f}} = \frac{s^2C_dC_fR_d + s(C_d + C_f)}{sR_dC_d + 1} \quad (4.35)$$

At the end, the overall admittance and impedance of the inverter output d component are given as in Eq. (4.36) and (4.37).

$$Y_{s-d} = Y_{out-d} + Y_c \quad (4.36)$$

$$Z_{s-d} = 1/Y_{s-d} \quad (4.37)$$

4.3.2. Impedance q Component

The q component control system whose block diagram is given by Figure 4.6, has not a cascaded structure because DC voltage control set only d component reference of the control controller. In the control scheme, open loop transfer functions with current control and PLL are shown. PLL generates the phase angle θ based on grid voltage and current control regulates the q component of the line current i_{oq} [69].

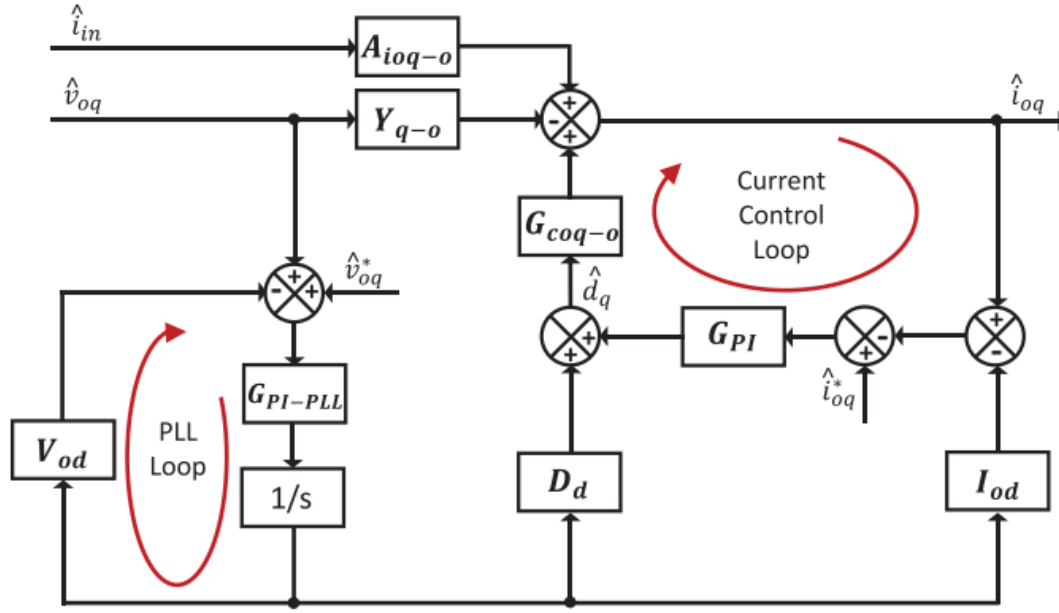


Figure 4.6. The q Component Open Loop Transfer Functions with Current Control and PLL [69]

In Figure 4.6, there are additional signal paths from the grid voltage q component to the duty cycle D_d and sensed current I_{od} because the signals going from the reference frame to another are equal in their state values not small signal content [5].

From Figure 4.6, gain of the current control is solved as in Eq. (4.38) by assuming PWM and sensor gains as unity.

$$L_{out-q} = G_{PI}G_{coq-o} \quad (4.38)$$

The inverter output q component admittance is derived as given by Eq. (4.39) which is the ratio of output current \hat{i}_{oq} to output voltage \hat{v}_{oq} .

$$Y_{out-q} = -\frac{\hat{i}_{oq}}{\hat{v}_{oq}} = \frac{Y_{q-o}}{(1+L_{out-q})} - \frac{I_{od}}{V_{od}} \frac{L_{out-q}}{(1+L_{out-q})} \frac{L_{PLL}}{(1+L_{PLL})} - \frac{D_d}{V_{od}} \frac{G_{coq-o}}{(1+L_{out-q})} \frac{L_{PLL}}{(1+L_{PLL})} \quad (4.39)$$

By considering the admittance of the LCL filter capacitor branch, overall output admittance and impedance is given by Eq. (4.40) and (4.41).

$$Y_{s-q} = Y_{out-q} + Y_c \quad (4.40)$$

$$Z_{s-q} = 1/Y_{s-q} \quad (4.41)$$

4.4. Grid Impedance

In order to design an adaptive controller, grid impedance must be measured continuously because the grid has a dynamic behavior and the impedance changes at any moment. There are several methods in the literature for measurement of the grid impedance [77]–[83]. Generally, a disturbance signal is injected to the grid and its response is measured by the system. In [77], sine sweeps are injected to the grid and Fourier analysis is applied to the measured voltage and current at the steady state. This method gives the most reliable and accurate solution but it is not useful due to required long measurement time [82]. The injection of an impulse [80] or Pseudo-Random Binary Sequence (PRBS) [81] signal provides the measurement at a broad frequency range.

The adaptive controller can be divided into two parts as PRBS injection and impedance estimation. Excitation signal is injected to the grid with the current and grid impedance is estimated by using measured voltage and current.

4.4.1. Pseudo Random Binary Sequence Injection

In this study, Maximum Length Binary Sequence (MLBS) injection is performed for online grid impedance measurement. The MLBS is an easy to generate type of PRBS and provides a deterministic and periodic signal with lowest possible peak factor [81]. The MLBS signal can be injected through multiple periods and averaging can be applied in order to determine the grid impedance. Thus, the amplitude of the MLBS signal can be kept at small values and less distortions occur at the injected grid current.

The PRBS signal is composed of two levels as 0 and 1. The signal value can change only at each clock pulse interval Δt . State change of the signal is determined by a function and the signal repeat itself by a period $T = N\Delta t$ where $N = 2^n - 1$ and n represents the number of registers [81]. In practice, logic binary values 0 and 1 are mapped to $-a$ and $+a$ where a represents the amplitude of the signal, to generate a symmetrical signal whose average is nearly 0.

In this study, MLBS signal is generated by using the system shown by Figure 4.7. Generated MLBS signal is added to d component current reference of the current controller for the grid current injection.

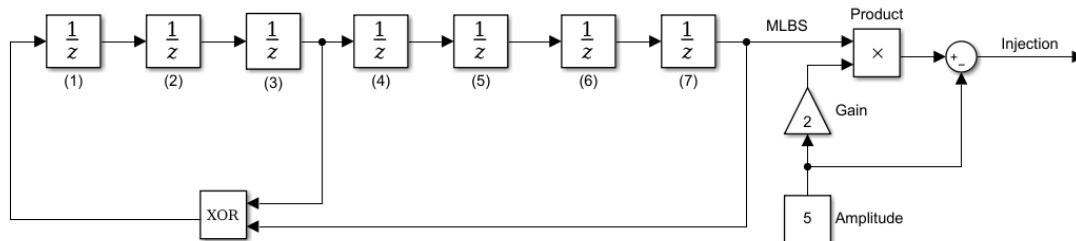


Figure 4.7. 7-bits Shift Register with XOR Feedback for MLBS Generation

For the generation of MLBS signal, the feedbacks of XOR function are taken from stage 3 and 7 to provide a periodic signal with constant power spectrum up to 1 kHz. The truth table of XOR function is given by Table 4.1.

Table 4.1. Truth Table of Exclusive OR (XOR) Function

Input 1	Input 2	Output
0	0	0
0	1	1
1	0	1
1	1	0

The generated 7 bits MLBS signal in time domain is given by Figure 4.8 and the states of each register are shown in Table 4.2. The signal whose amplitude changes between ± 5 is generated at 5 kHz and must be started at a state different than 0,0,0,0,0,0,0. In this study, the signal is started from 1,1,0,1,1,0,1 and repeats itself at every 127 clock cycle. The amplitude of the MLBS signal is determined as 10 % of the rated current. There is a trade of between measurement accuracy and current distortions. Increasing the amplitude of MLBS signal provides more accurate measurements and more distorted grid current.

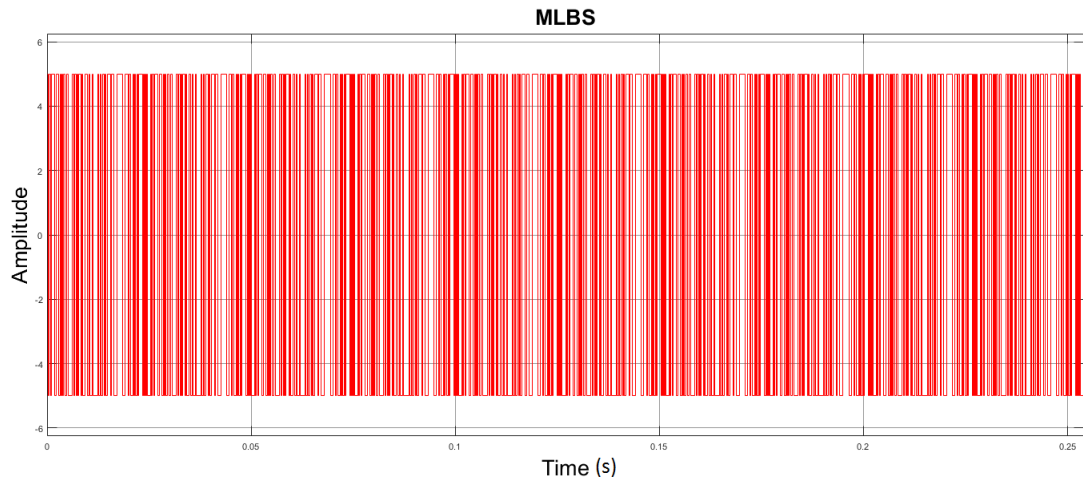


Figure 4.8. Generated 7 bits MLBS Signal

Table 4.2. State of Each Shift Register While Generating the 7 bits MLBS Signal

Shift	Stage 1	Stage 2	Stage 3	Stage 4	Stage 5	Stage 6	Stage 7
1	1	1	0	1	1	0	1
2	1	1	1	0	1	1	0
3	1	1	1	1	0	1	1
4	0	1	1	1	1	0	1
5	0	0	1	1	1	1	0
6	1	0	0	1	1	1	1
			.				
			.				
			.				
126	0	1	1	0	1	0	0
127	1	0	1	1	0	1	0
128	1	1	0	1	1	0	1
129	1	1	1	0	1	1	0
			.				
			.				
			.				

The power spectrum of a MLBS signal is calculated by Eq. 4.42 where q represents the sequence number, a is the signal amplitude and N is the signal length [81].

$$\Phi_{MLBS}(q) = \frac{a^2(N+1)}{N^2} \frac{\sin^2(\pi q/N)}{(\pi q/N)^2}, \quad q = \pm 1, \pm 2, \dots \quad (4.42)$$

Power spectrum of the generated 127 bit length MLBS signal is given by Figure 4.9.

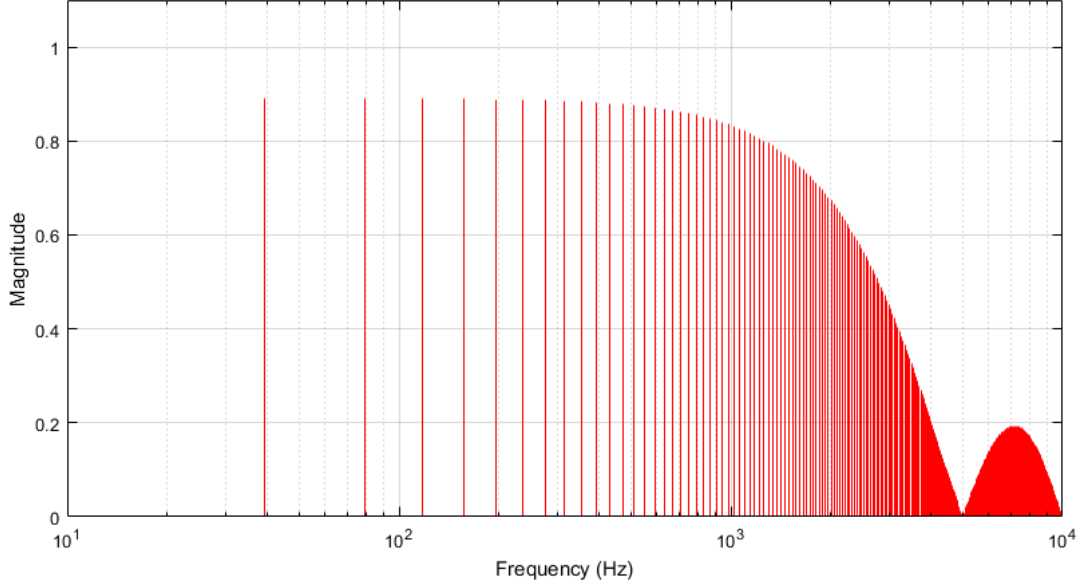


Figure 4.9. Power Spectrum of 7-bits MLBS Signal Generated at 10 kHz

In order to have reliable measurement results, amount of the energy should be nearly equal at the frequencies which the measurement are taken [69]. As seen from Figure 4.9, the energy of the signal is nearly constant up to 1 kHz and drops to zero at generation frequency f_{gen} and its harmonics. According to [69], the bandwidth of the measurement should be limited to $0.45f_{gen}$ because the energy of the signal drops to half of the energy of first harmonics. Thus, the generation frequency f_{gen} of the MLBS signal can be determined by considering measurement bandwidth [69].

Increasing the amplitude a of the MLBS signal provides more reliable and accurate results but causes more harmonic distortions at the injected grid current. Averaging the measurements reduces the effects of noise on the estimated result but requires longer time for the estimation. If the signal is averaged over P excitation periods,

effect of noise is reduced by $1/\sqrt{P}$ but the time required for the estimation increases to $t_{meas} = NP/f_{gen}$ [81].

4.4.2. Estimation of Grid Impedance

In order to estimate the grid impedance, the voltage and current are measured at the PCC while injecting the MLBS signal. The injected current signal is denoted as $x(t)$ and the voltage response of the system is represented by $y(t)$. For the measurement of grid impedance in a broad frequency band, these time domain signals are transformed to frequency domain by using Fourier transformation [69]. The transformed excitation and response signals are represented as $X(\omega)$ and $Y(\omega)$ respectively. At the end, frequency response of the grid impedance is estimated by using Eq. (4.43).

$$G(\omega) = Y(\omega)/X(\omega) \quad (4.43)$$

For the estimation of the grid inductance, the method given by Figure 4.10 is performed.

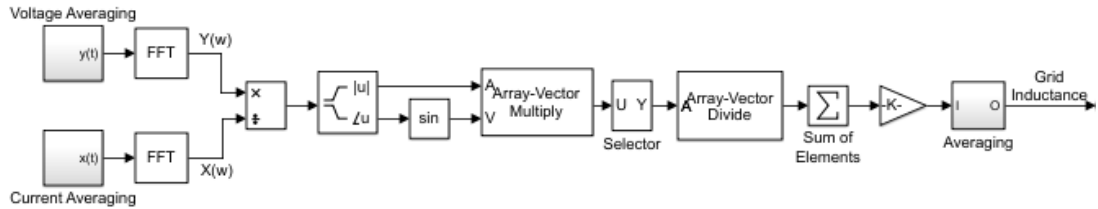


Figure 4.10. Estimation of Grid Inductance

Three phase voltage and currents are measured by the sensors. The measured signals are transferred to dq reference frame and q components are averaged over 5 injection periods to reduce the effects of noises. The averaged data are transformed to frequency domain by using Fast Fourier Transform. Frequency response of the grid impedance is determined by dividing voltage and current responses. The obtained complex data are computed to magnitude and phase angle information. By using Eq. (4.44), the grid inductance is estimated from the impedance at whole frequency range.

$$L_g(\omega) = \frac{Z_g(\omega)}{\omega} = \frac{|G(\omega)|\sin(\arctan(G(\omega)))}{\omega} \quad (4.44)$$

The estimated values up to 1 *kHz* are selected and averaged for each excitation cycle. At the end, there is also an averaging block which is used to increase the reliability and accuracy of the estimation.

4.5. Analysis of the System under Weak Grid Conditions

In this part, impedance based stability analysis is performed for *d* and *q* components of the grid connected system and effects of high grid impedance on the system stability is analyzed. In order to analyze the system stability Bode plots and Nyquist diagrams are used in this part.

4.5.1. Impedance *d* Component Stability

Frequency responses of inverter output impedance *d* component and grid impedance are shown in Figure 4.11. The blue line represents inverter output impedance *d* component based on Eq. (4.34) to (4.36), the red and green lines are used for grid impedance with 3 and 0.2 *mH* respectively. The *d* component of the inverter output impedance is not effected from PLL settings and has the same shape for both PLL bandwidths. DC voltage control introduce constant power source properties so the phase of the impedance is zero at low frequencies [5]. At stiff grid condition (when the grid inductance equals to 0.2 *mH*), magnitudes of inverter output impedance *d* component and grid impedance overlap at 725 *Hz*. with 154.1° phase difference. This means that the system is stable with 25.9° phase margin. At weak grid condition (when the grid inductance equals to 3 *mH*), magnitudes of inverter output impedance *d* component and grid impedance overlap at 170 *Hz*. with 170.7° phase difference. Thus, the system is still stable with 9.3° phase margin.

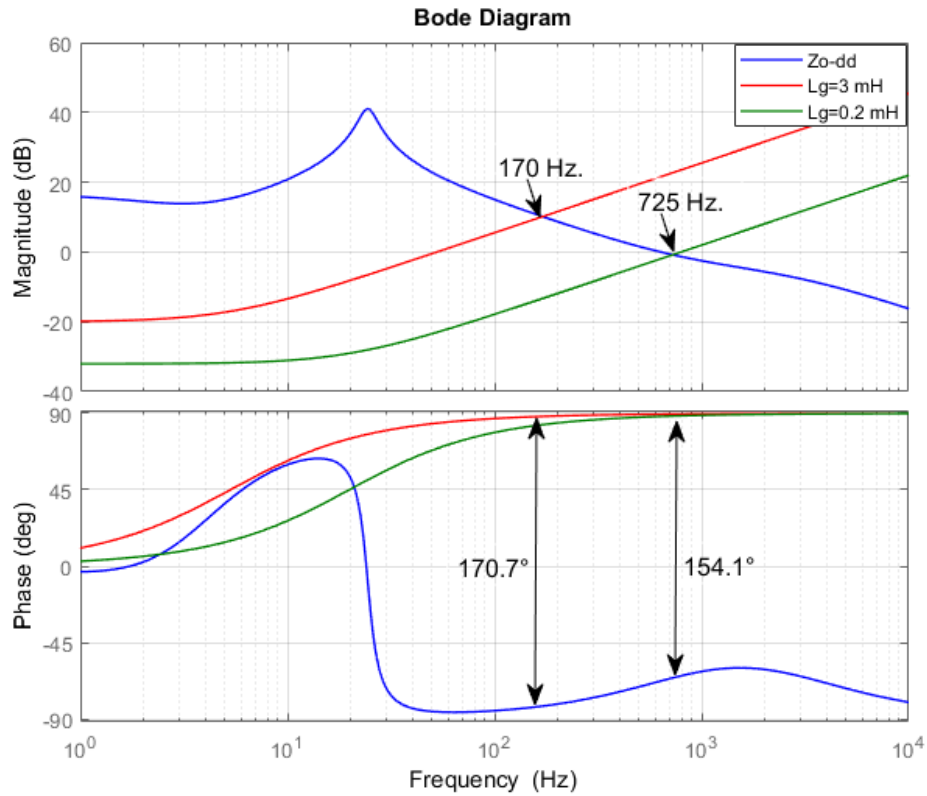


Figure 4.11. Frequency Responses of Inverter Output Impedance d Component and Grid Impedance

In addition to Bode plot, the stability can be considered based on Nyquist diagram given by Figure 4.12. The inverse minor loop gain Z_g/Z_{s-d} crosses the unity circle on the complex plane but the phase difference is less than 180° . Therefore, the diagram of the inverse minor loop does not encircle $(-1,0)$ point and the system is stable for both stiff and weak grid conditions.

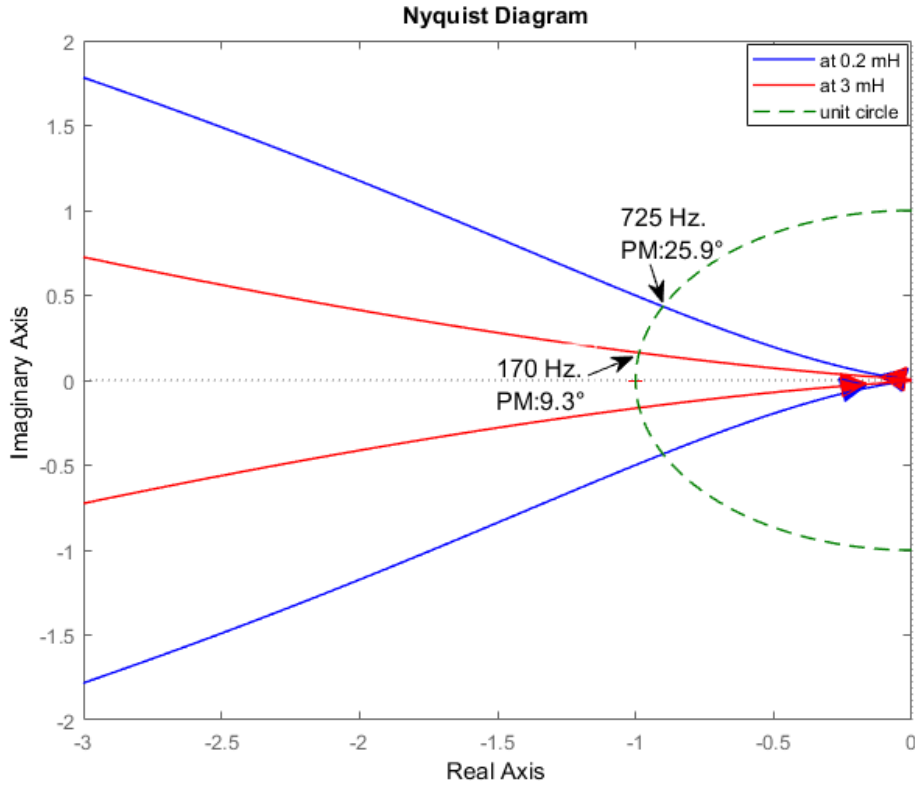


Figure 4.12. Ratio of Impedance d Components Z_g/Z_{s-d} on the Complex Plane

As seen from Figure 4.11, the phase difference between the inverter output impedance d component and grid impedance is smaller than 180° at all frequency range and the system is always stable independent from grid conditions and PLL settings. The phase angles of both impedances are between -90° and $+90^\circ$ and this means that they behave as a passive circuit at all frequency range. In order to avoid impedance based instabilities, inverter output impedance should be designed as close as possible to passive circuit characteristics [84], [85].

4.5.2. Impedance q Component Stability

Frequency responses of inverter output impedance q component for two different PLL parameters and grid impedance are shown in Figure 4.13. The blue and red lines represent inverter output impedance q components based on Eq. (4.39) to (4.41) for

faster and slower PLLs respectively. Also, the green and brown lines are used for grid impedance with 3 and 0.2 mH respectively. The faster PLL designed with 0.1 s settling time T_s has 22.2 Hz. control bandwidth. On the other hand, the slower PLL designed with 0.3 s settling time T_s has 7.4 Hz. control bandwidth. At stiff grid condition (when the grid inductance equals to 0.2 mH), magnitudes of inverter output impedance d component and grid impedance overlap at 725 Hz. with 154.3° phase difference for both the faster and slower PLLs. This means that the system is stable with 25.7° phase margin for both PLL parameters. At weak grid condition (when the grid inductance equals to 3 mH), magnitudes of inverter output impedance d component and grid impedance overlap at 170 Hz for both the faster and slower PLLs. At this point, the phase differences between inverter output impedance d component and grid impedance are 174° and 186° for the slower and faster PLLs. Thus, the system is stable with 6° phase margin for the slower PLL but unstable for the faster PLL.

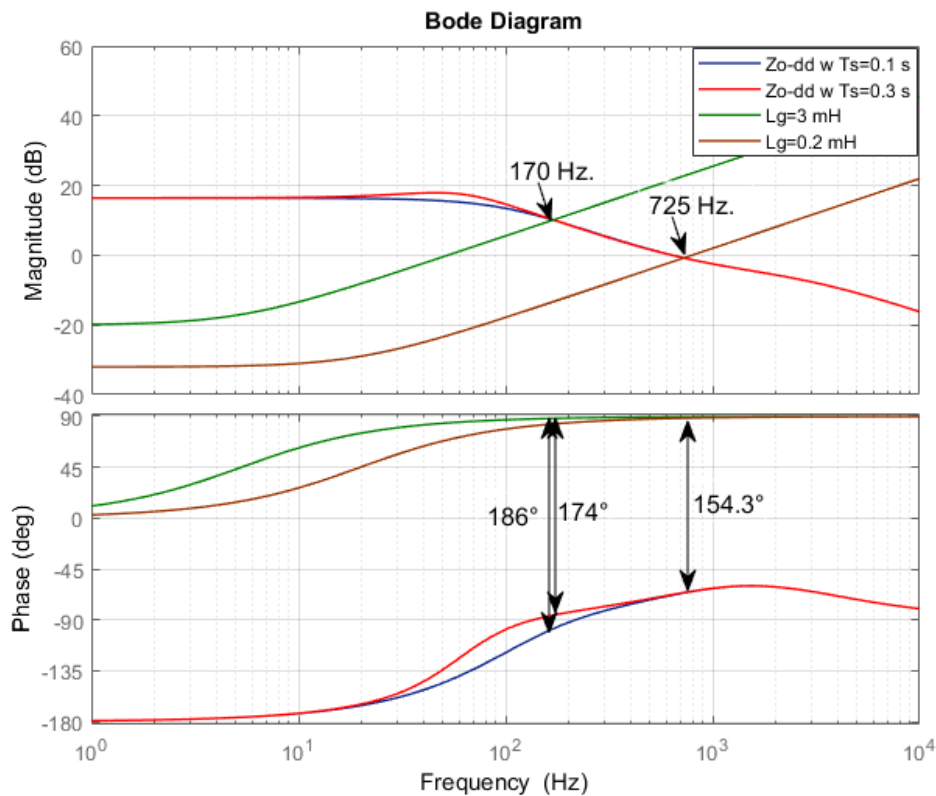


Figure 4.13. Frequency Responses of Inverter Output Impedance q Component and Grid Impedance

As seen by Figure 4.14, the inverse minor loop gain Z_g/Z_{s-q} crosses the unity circle on the complex plane but the phase difference is less than 180° . Therefore, the diagram of the inverse minor loop does not encircle $(-1,0)$ point and the system is stable with 25.7° phase margin for both the faster and slower PLLs under stiff grid conditions.

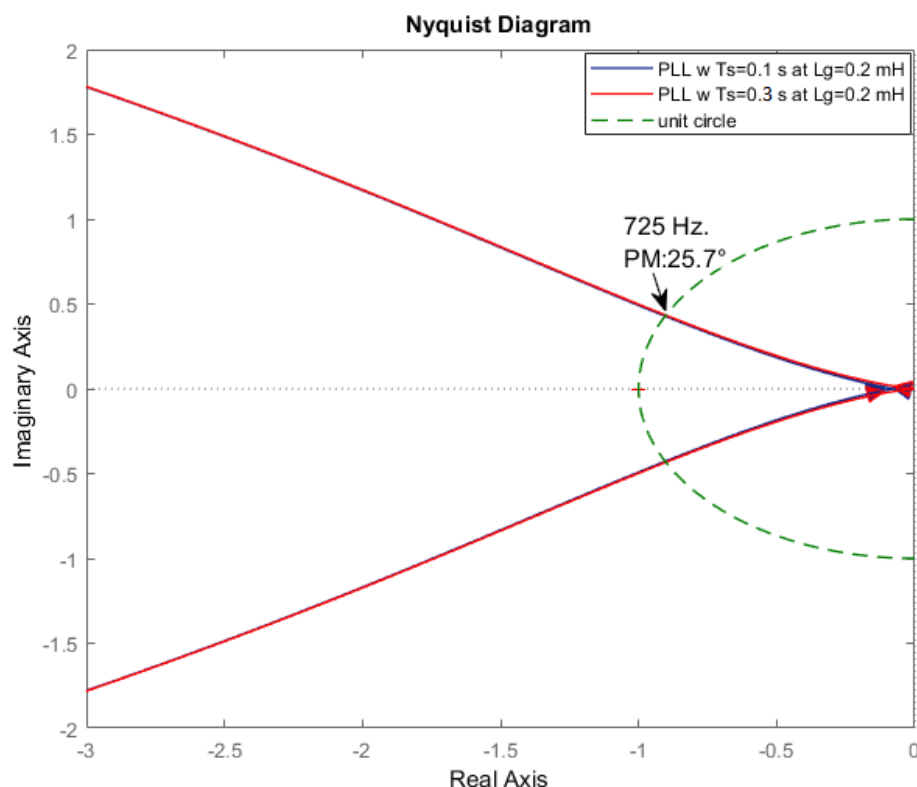


Figure 4.14. Ratio of Impedance q Components Z_g/Z_{s-q} on the Complex Plane under Stiff Grid

As seen by Figure 4.15, the inverse minor loop gain Z_g/Z_{s-q} crosses the unity circle on the complex plane but the phase difference is less than 180° for the slower PLL under weak grid conditions. Therefore, the diagram of the inverse minor loop does not encircle $(-1,0)$ point and the system is stable with 6° phase margin and 5.9 dB gain margin for the slower PLL under weak grid conditions.

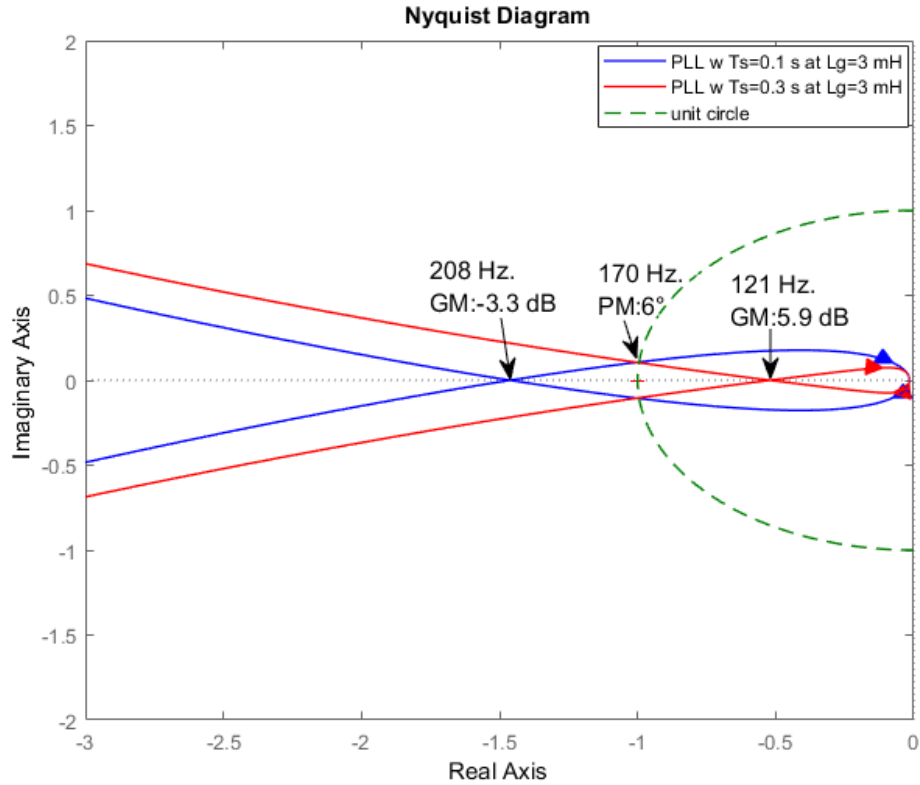


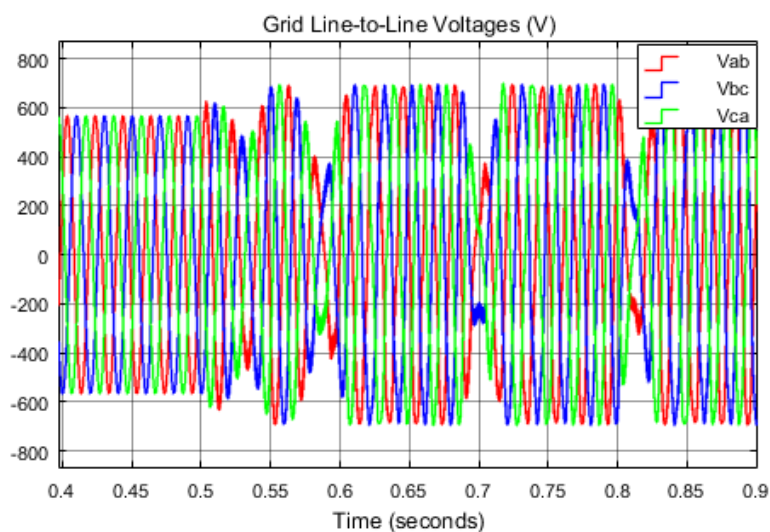
Figure 4.15. Ratio of Impedance q Components Z_g/Z_{s-q} on the Complex Plane under Weak Grid

As seen from Figure 4.15, for the faster PLL, the contour encircles $(-1,0)$ point in clockwise direction once under weak grid conditions and this means that the inverse minor loop has a Right Hand Plane (RHP) zero. Therefore, the last term of Eq. (5.1) has a RHP pole and the system is unstable with the faster PLL under weak grid conditions.

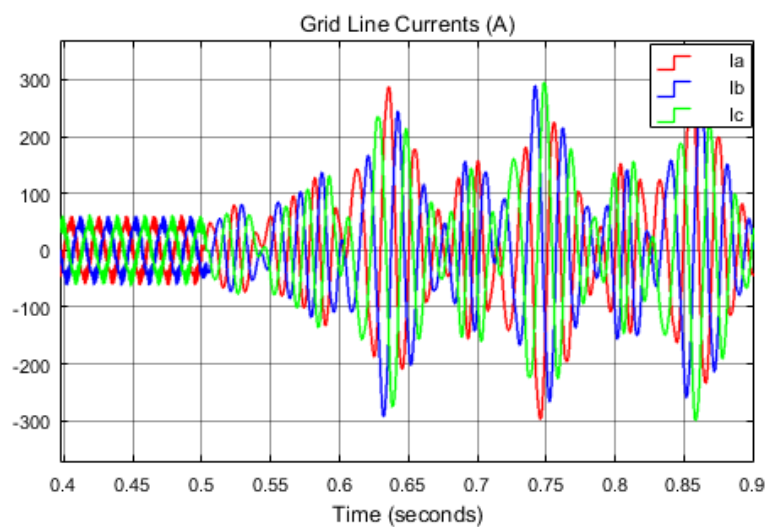
4.6. Stability Analysis with the Nonlinear Simulation Model

Impedance based stability analysis is performed and it is seen that in order to stably operate under weak grid conditions The response of the system is analyzed by the nonlinear model which is given in Chapter 1. The DSOGI-PLL of the system is designed by $T_s = 0.1\text{ s}$ and $\zeta = 0.707$ and run under ideal grid condition. While supplying 50 A_{peak} grid current, the inductance of the grid is increased from 0 to 3

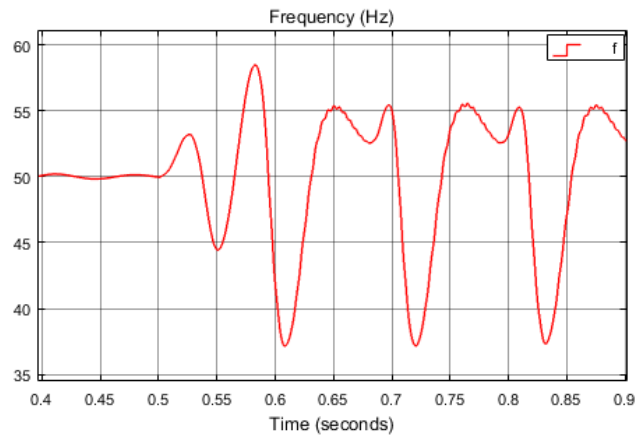
mH at $t = 0.5$ s to simulate weak grid condition. The change of voltage at the PCC, injected grid current, estimated frequency, active and reactive power of the system is shown in Figure 4.16.



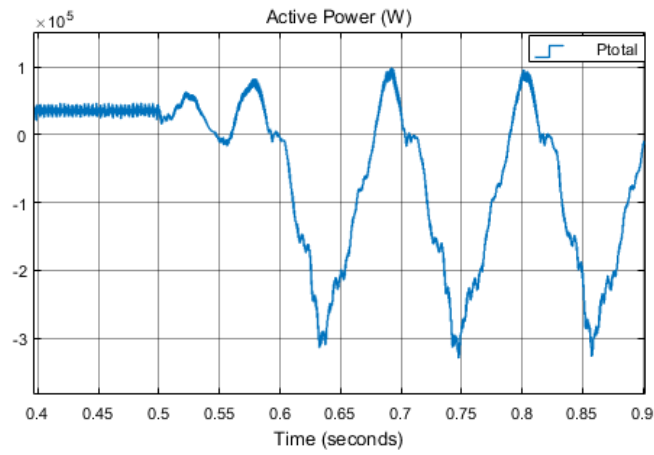
(a)



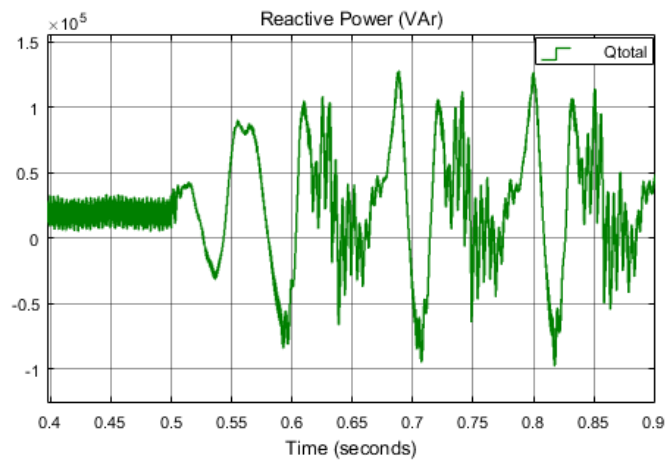
(b)



(c)



(d)

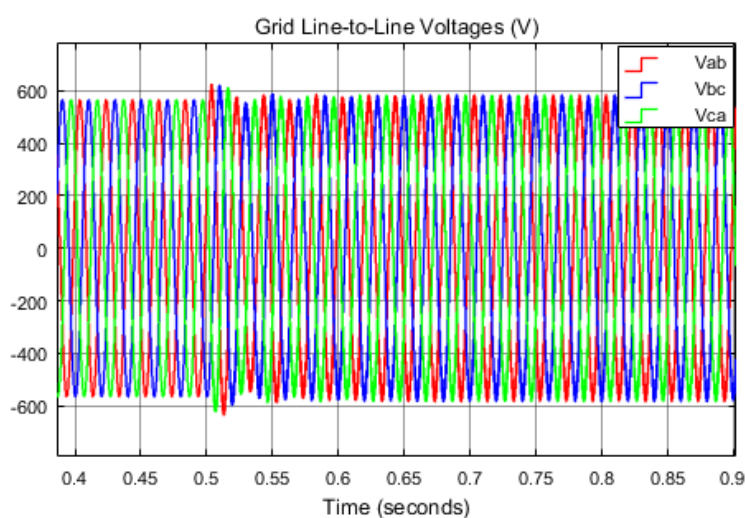


(e)

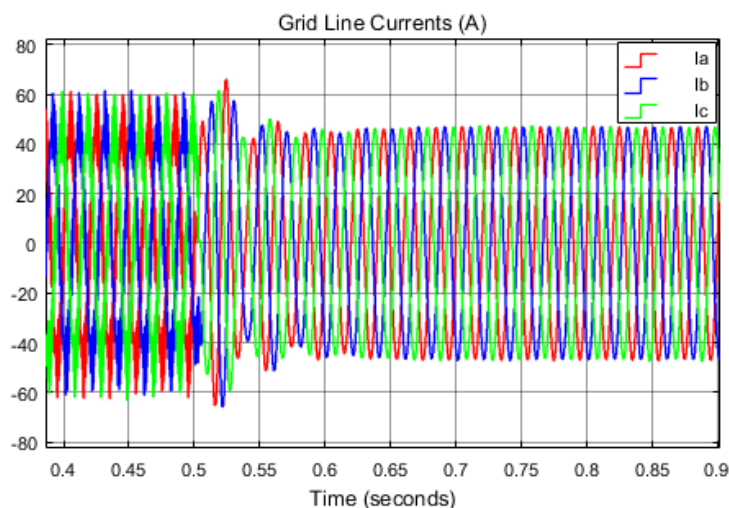
Figure 4.16. PCC Voltage (a), Injected Grid Current (b), Estimated Frequency (c), Active (d) and Reactive (e) Power at Sudden Grid Inductance Change with $T_s = 0.1$ s

As seen from Figure 4.16, the system is stably operating until sudden grid inductance change but after that point instability occurs and the estimated frequency is deviated from 50 Hz. Instable operation of the inverter causes high amount of current injection to the grid.

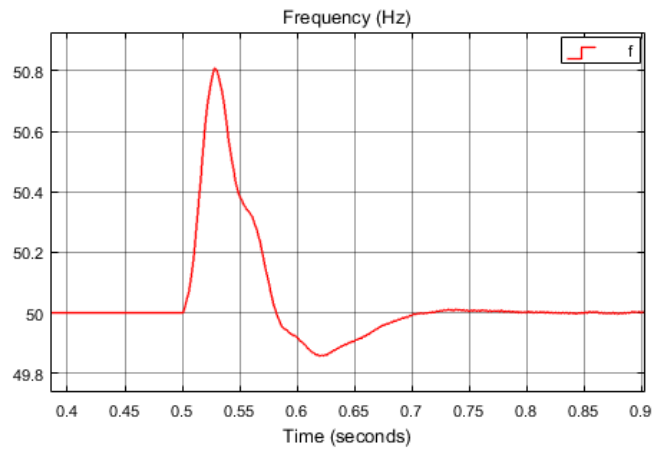
The settling time of the PLL is changed from 0.1 to 0.3 s and so the bandwidth of the PLL is changed from 22.2 to 7.4 Hz depending on Eq. (4.16). The same procedure is repeated for $T_s = 0.3$ s and grid inductance is suddenly increased at $t = 0.5$ s. The obtained waveforms are shown in Figure 4.17.



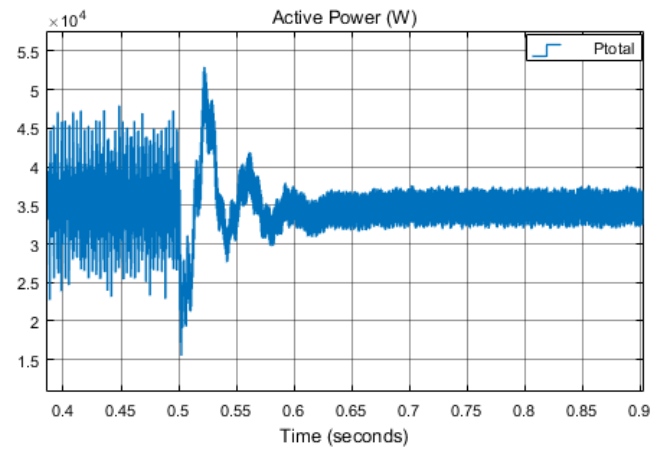
(a)



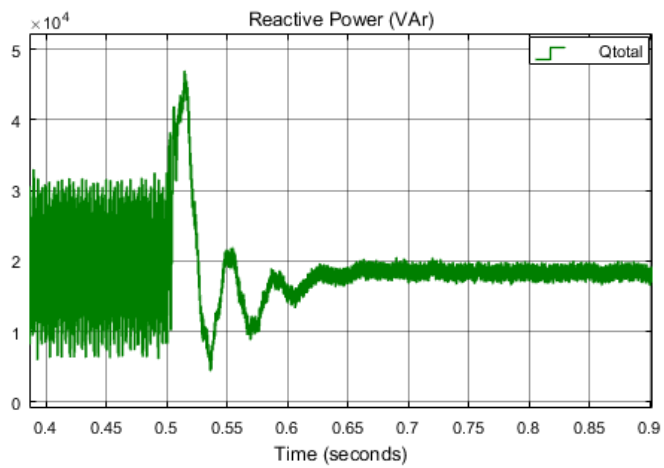
(b)



(c)



(d)



(e)

Figure 4.17. PCC Voltage (a), Injected Grid Current (b), Estimated Frequency (c), Active (d) and Reactive (e) Power at Sudden Grid Inductance Change with $T_s = 0.3$ s

As seen from Figure 4.17, the system maintains stable operation with $T_s = 0.3$ s despite the sudden grid inductance change. At the inductance change moment, estimated frequency deviates from 50 Hz a little bit but recovers fast. The injected current is not affected from the inductance change. As seen from the analysis an adaptive controller is required to maintain the stable operation under weak grid conditions.

4.7. Summary

In this chapter, impedance based stability analysis is performed considering the grid connected VSI system under stiff and weak grid conditions. In order to perform Nyquist and Bode stability criterions inverter output impedance and grid impedance are required. Inverter output impedance d and q components are derived by using mathematical model of the inverter but the grid has a dynamic behavior and its impedance is changing continuously. In this part, a grid impedance estimation method is proposed to adaptively set the PLL parameters. PRBS signal is added to d component grid current reference and injected to the grid with the current. The voltage response of the grid is measured and by using FFT analysis, grid impedance is estimated in a broad frequency range. Impedance based stability analyses are performed for two different PLLs under stiff and weak grid conditions. The obtained results are investigated in a more detailed aspect by using nonlinear MATLAB/Simulink model. It is obtained that the bandwidth of the PLL should be decreased in order to operate under weak grid conditions.

CHAPTER 5

EXPERIMENTAL RESULTS

Current and DC voltage controller, PLL and LCL filter design were given in Chapter 3 as a part of grid connected inverter controller. Stability analysis of the overall system was performed in Chapter 4 with analytical and nonlinear simulation model results. In this chapter, performance of the designed grid impedance estimation based adaptive controller is analyzed in detail with experimental results. The block diagram of the experimental setup is shown in Figure 5.1 and the picture of the system is given by Figure 5.2.

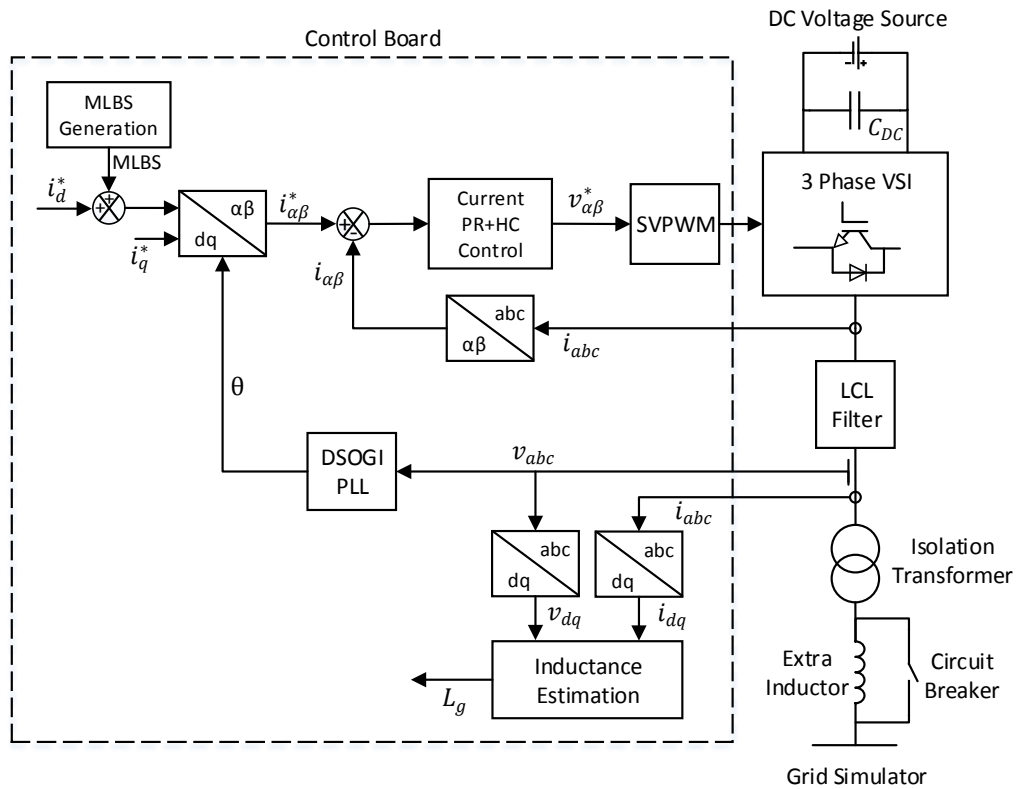


Figure 5.1. Block Diagram of the Experimental Setup

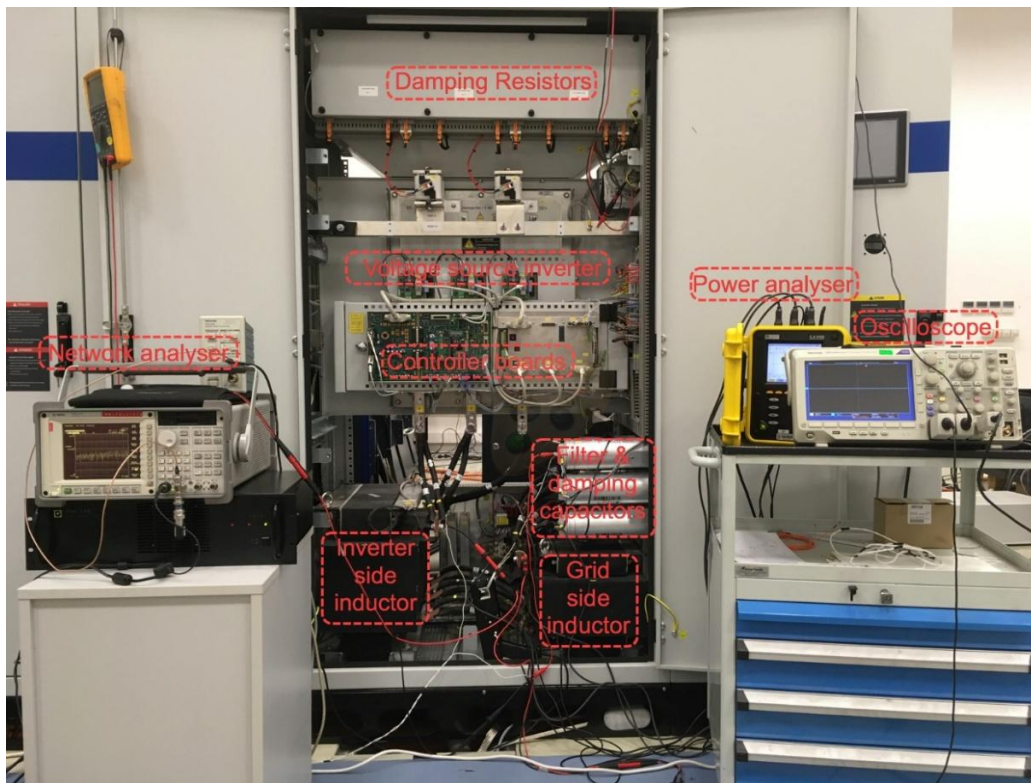


Figure 5.2. Experimental Setup

The setup includes a DC voltage source, a grid simulator as an AC voltage source, three phase VSI, control board, LCL filter, isolation transformer and extra inductor block with a parallel connected circuit breaker. For the experiments, outer DC voltage control loop is omitted because its control bandwidth is smaller than current controller and has no effect on the stability. Thus, a DC voltage source is connected to DC side of the VSI which is Semikron SKS SL 80 IGBT stack. At the output of the VSI a passive shunt R-C damped LCL filter is placed in order to filter high frequency contents of current and voltage waveforms. An isolation transformer is used between VSI and grid simulator to provide galvanic isolation between them. For simulation of stiff and weak grid conditions, a 2.8 mH inductor block with a circuit breaker whose picture is shown in Figure 5.3, is placed between isolation transformer and grid simulator. Aselsan Inverter Control Unit (ICU) which is a control board with Texas Instruments TMS320F28377D microcontroller runs the control algorithms and

generates the PWM signals for each IGBT. California Instruments MX45 power source which provides four-quadrant operation is used as grid simulator.

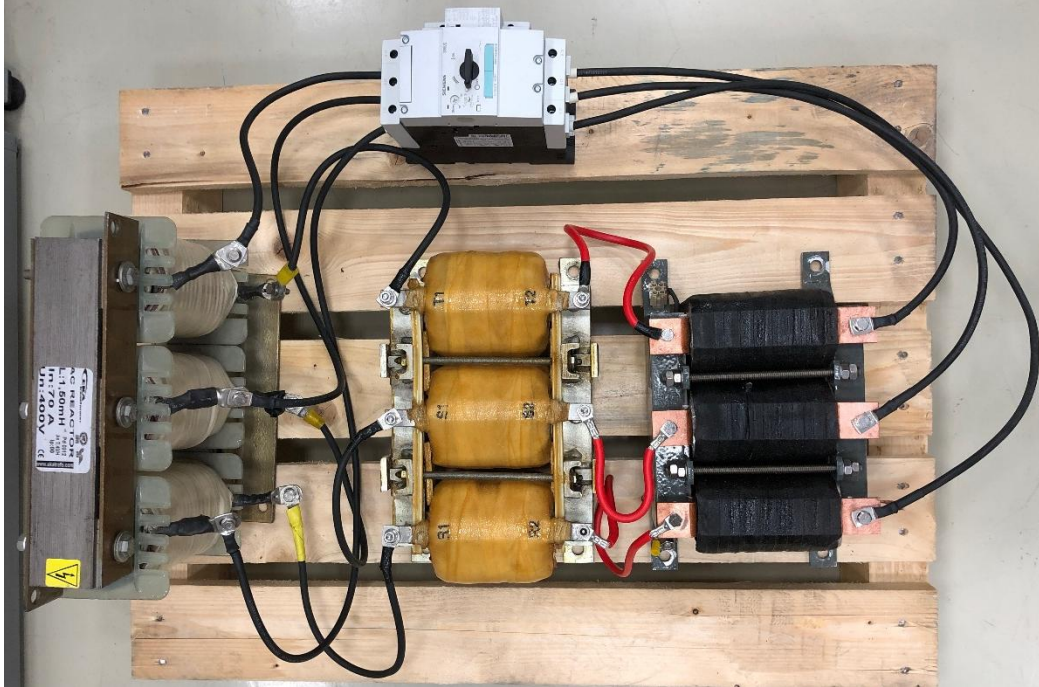


Figure 5.3. Inductor Block with a Circuit Breaker

In this study, the simulation studies are carried out in MATLAB/Simulink environment with nonlinear models. For the simulations, the controllers are designed in discrete domain and required c-codes for microprocessor are automatically generated from the designed controller blocks by using TI C2000 support from embedded coder package of MATLAB/Simulink.

The grid connected inverter system is operated at a certain steady state point and the impedance based stability analysis in Chapter 4 is performed considering that point. The system is designed for 300 kW but the operating point is limited by considering the ratings of the grid simulator and extra inductors. The reference of q component grid current is determined in a way to compensate the reactive power drawn by the LCL filter capacitors. The parameters of the grid connected inverter at steady state operating point are shown in Table 5.1.

Table 5.1. *System Parameters of the Experimental Setup*

Symbol	Quantity	Value	Unit
V_g	Nominal line-to-line grid voltage	400	V_{rms}
f_g	Grid frequency	50	Hz
f_{sw}	Switching frequency	5	kHz
f_{samp}	Sampling frequency	10	kHz
V_{DC}	DC link voltage	700	V
L_1	Converter side inductance	125	μH
L_2	Grid side inductance	60	μH
C_f	Filter capacitance	100	μF
C_d	Damping capacitance	200	μF
R_d	Damping resistance	0.9	Ω
L_{iso}	Isolation transformer inductance	0.2	mH
L_{ext}	Extra inductance	2.8	mH

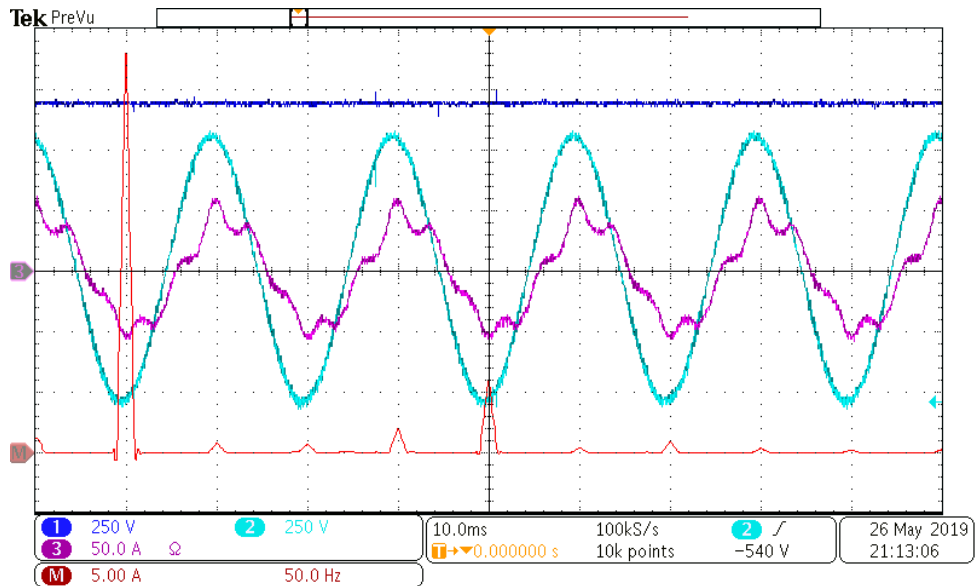
An oscilloscope is used in order to see DC link voltage (CH1), line to line PCC voltage (CH2) and injected grid current (CH3) waveforms. Also, math function is used for the FFT of injected grid current in all oscilloscope images of this chapter.

5.1. Harmonic Compensation under Distorted Grid Condition

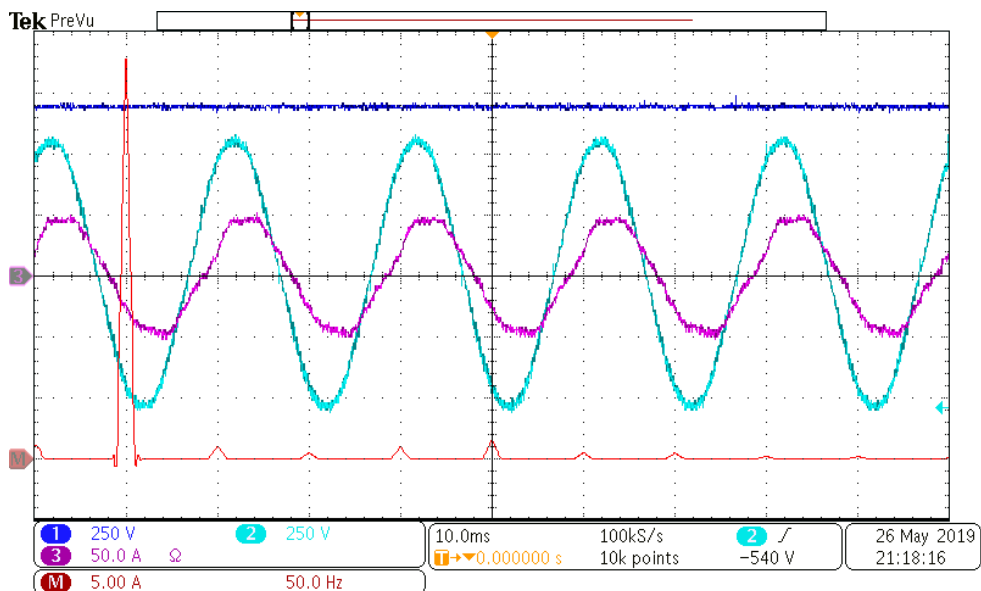
In this part, 5th and 7th harmonic compensation performance of the grid connected inverter system is analyzed in terms of the quality of the injected grid current. In order to see the difference between with and without harmonic compensator, each harmonic content is added to grid voltage at the amount of 1% of the fundamental grid voltage. THD values of the injected grid current are measured with power analyzer and compared for both conditions. The measured THD values are a little bit high because the system is designed for 300 kW operation but it is supplying 25 kW power to the grid.

5.1.1. 5th Harmonic Compensation

When 5th harmonic content is added to grid voltage at the amount of 1% of the fundamental grid voltage the obtained grid current waveforms are shown in Figure 5.4 without and with harmonic compensation.



(a)



(b)

Figure 5.4. DC Link Voltage (CH1), PCC Voltage (CH2), Grid Current (CH3) and FFT of Grid Current (Math) without (a) and with (b) 5th Harmonic Compensator

As seen from Figure 5.4, the grid current value at 5th harmonic is decreased from 6 A_{rms} to 2 A_{rms} with harmonic compensation.

THD values of each phase injected current are shown in Table 5.2 without and with harmonic compensation. It is seen that the quality of the injected grid current is improved with 5th harmonic compensator.

Table 5.2. THD Values of Grid Currents for without and with 5th Harmonic Compensation

	<i>Phase A</i>	<i>Phase B</i>	<i>Phase C</i>
without HC	16.7%	12.8%	18.2%
with HC	6.2%	5.5%	6.4%

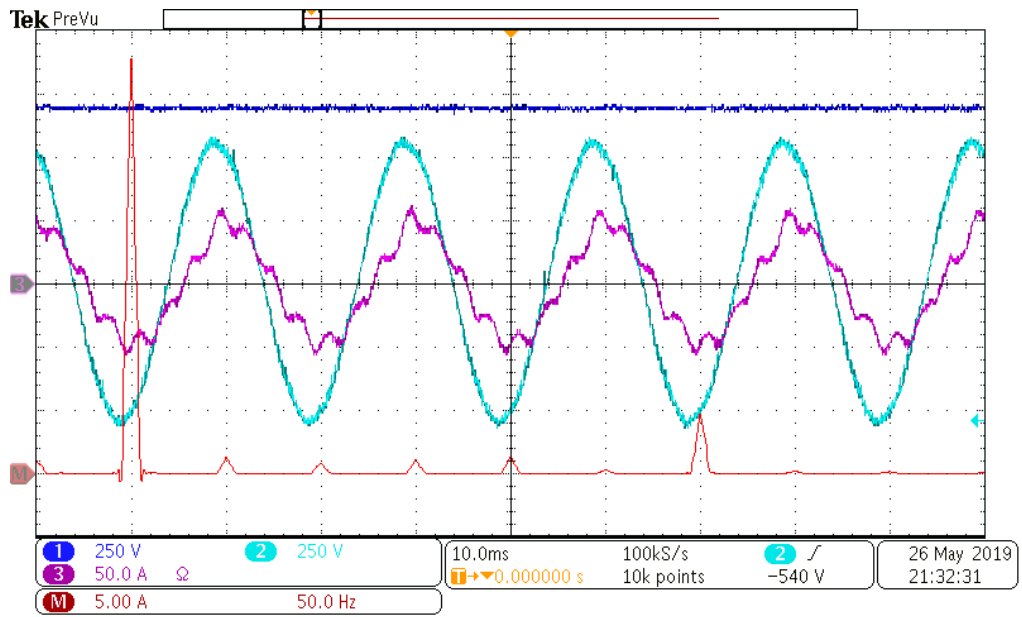
5.1.2. 7th Harmonic Compensation

When 7th harmonic content is added to grid voltage at the amount of 1% of the fundamental grid voltage the obtained grid current waveforms are shown in Figure 5.5 without and with harmonic compensation. As seen from Figure 5.5, the grid current value at 7th harmonic is decreased from 5 A_{rms} to 2 A_{rms} with harmonic compensation.

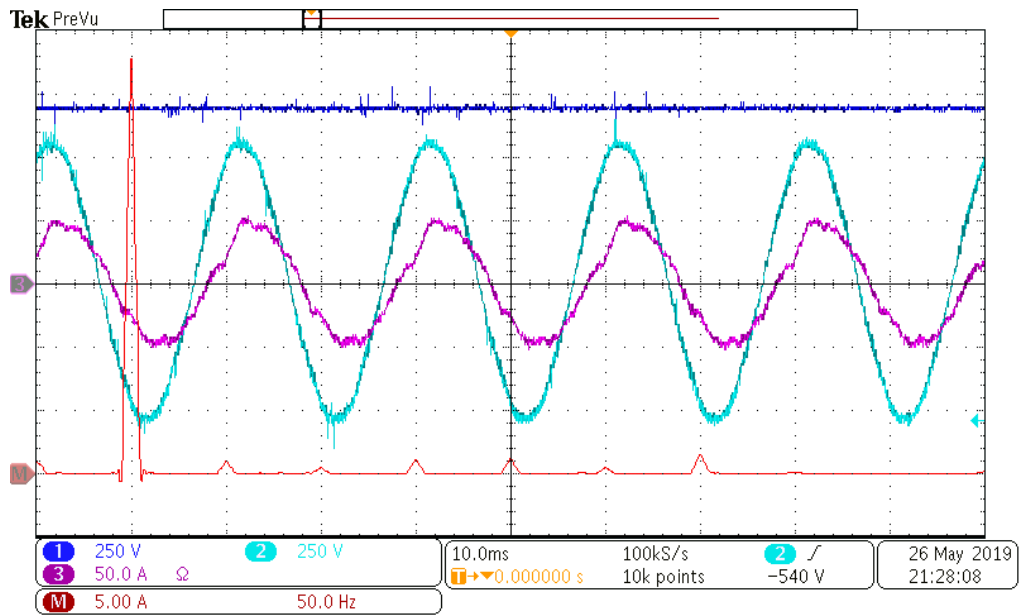
THD values of each phase injected current are shown in without and with harmonic compensation. It is seen that the quality of the injected grid current is improved with 7th harmonic compensator.

Table 5.3. THD Values of Grid Currents for without and with 7th Harmonic Compensation

	<i>Phase A</i>	<i>Phase B</i>	<i>Phase C</i>
without HC	12.6%	11.5%	13.9%
with HC	7.5%	7.8%	7.6%



(a)



(b)

Figure 5.5. DC Link Voltage (CH1), PCC Voltage (CH2), Grid Current (CH3) and FFT of Grid Current (Math) without (a) and with (b) 7th Harmonic Compensator

5.2. Estimation of Grid Inductance

The method for estimation of grid inductance was presented in Chapter 4.4. Two important points should be considered for real time inductance estimation. First one is that the injected MLBS signal should not cause high amount of distortions at the grid currents. Second one is that estimated grid inductance should be accurate for a stable operation.

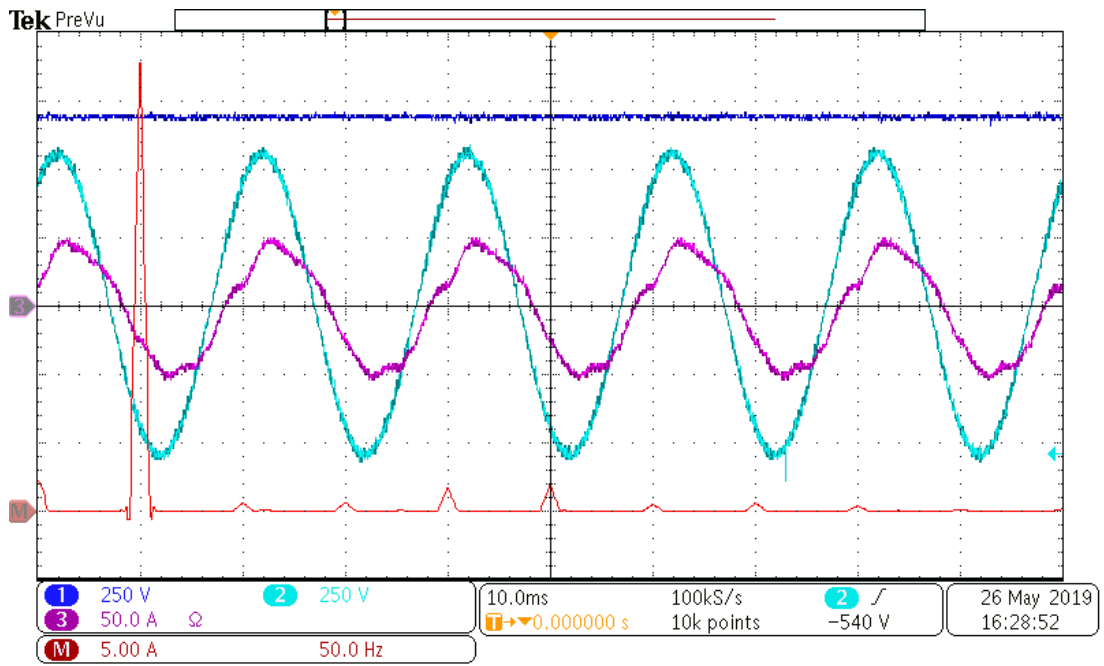
5.2.1. Grid Current Distortions Caused by MLBS Signal

In order to estimate the grid inductance, MLBS signal is added to the grid current d component reference. Increase of MLBS signal amplitude causes more distortions at the injected grid current. At this study, the amplitude of MLBS signal is selected as 10% of the d component current reference amplitude. The generated MLBS signal in Chapter 4.4.1 is used to determine the grid inductance. Injected current waveforms without and with the MLBS signal are given by Figure 5.6 and Figure 5.7 for stiff and weak grid conditions. As seen from Figure 5.6-b, the MLBS signal adds small amount of harmonic contents at all frequencies but does not cause serious distortions at the injected grid current. Under the weak grid conditions the effects of MLBS signal decrease and less distortions are observed at the grid current as seen from Figure 5.7.

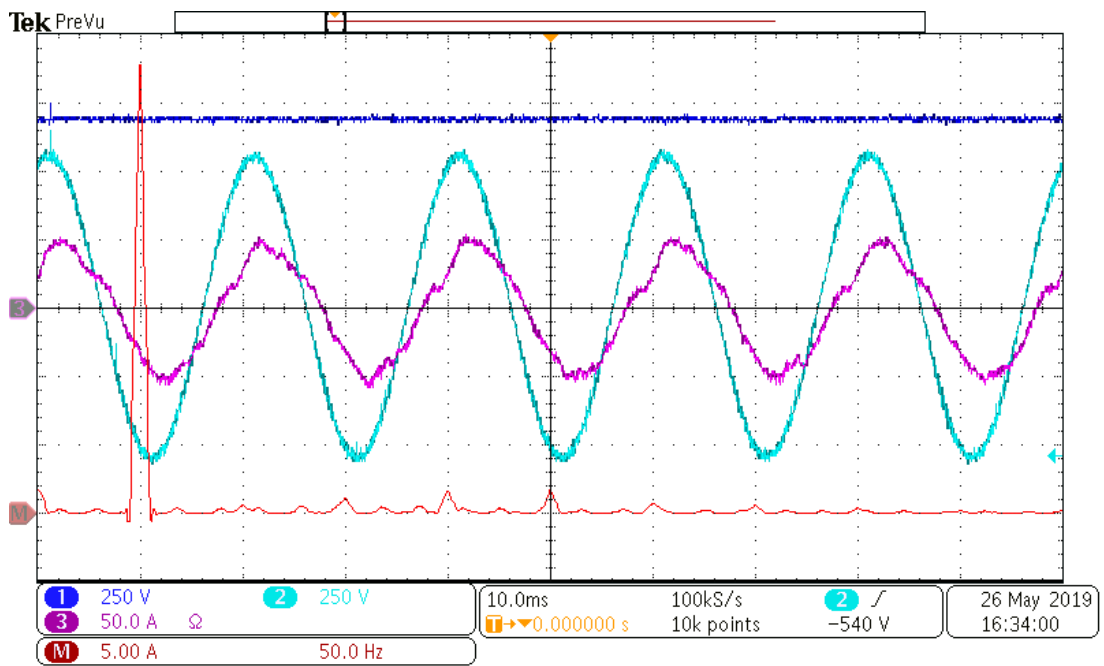
THD values of each phase injected current are shown in without and with MLBS signal under stiff and weak grid conditions. It is seen that the quality of the injected grid current is not affected so much from the MLBS signal. Also, increase of grid inductance have positive impact on the power quality.

Table 5.4. THD Values for without and with MLBS Signal under Stiff and Weak Grid Conditions

	<i>Phase A</i>	<i>Phase B</i>	<i>Phase C</i>
without MLBS under stiff grid	8.9%	8.6%	7%
with MLBS under stiff grid	8.2%	9.5%	7.7%
without MLBS under weak grid	5.4%	4.5%	4.5%
with MLBS under weak grid	5.1%	4.4%	4%

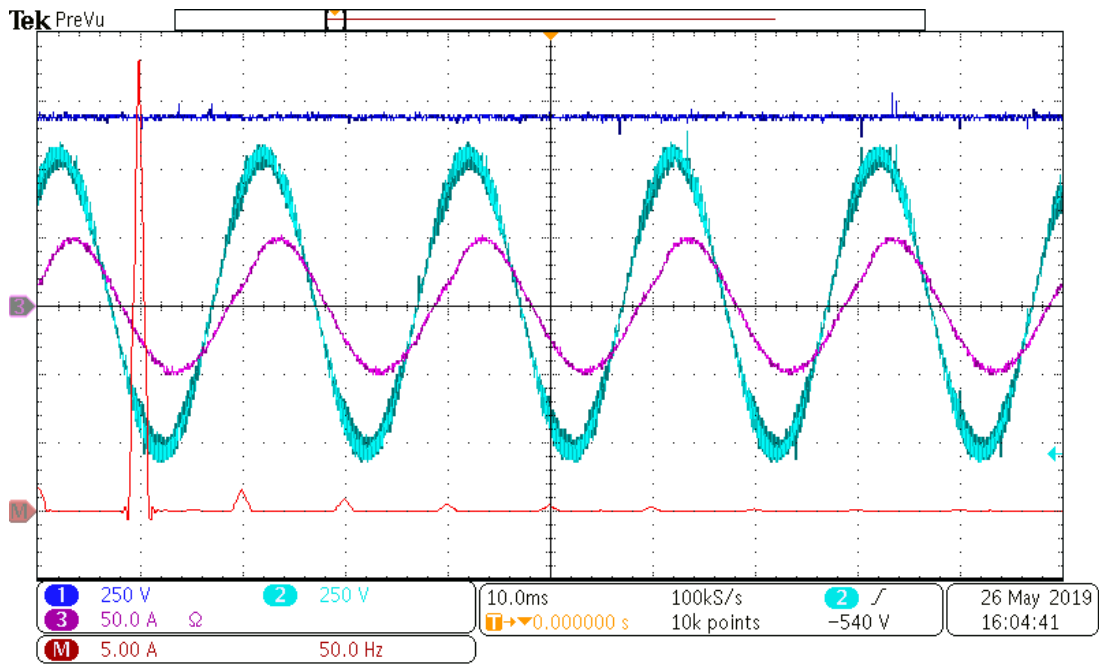


(a)

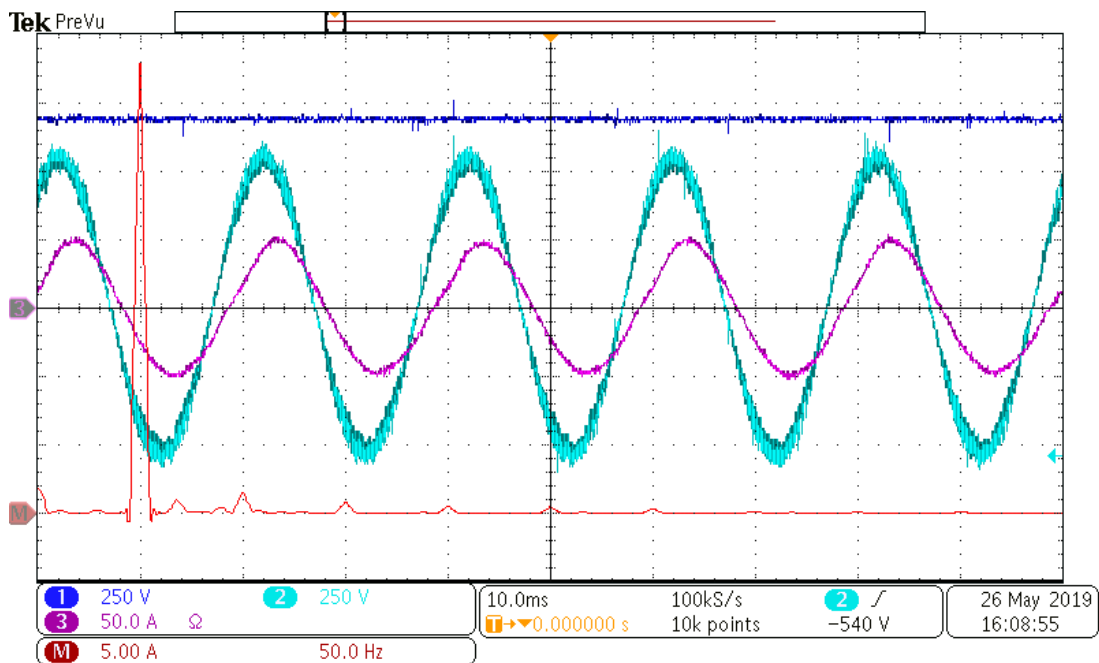


(b)

Figure 5.6. DC Link Voltage (CH1), PCC Voltage (CH2), Grid Current (CH3) and FFT of Grid Current (Math) without (a) and with (b) MLBS Signal under Stiff Grid



(a)



(b)

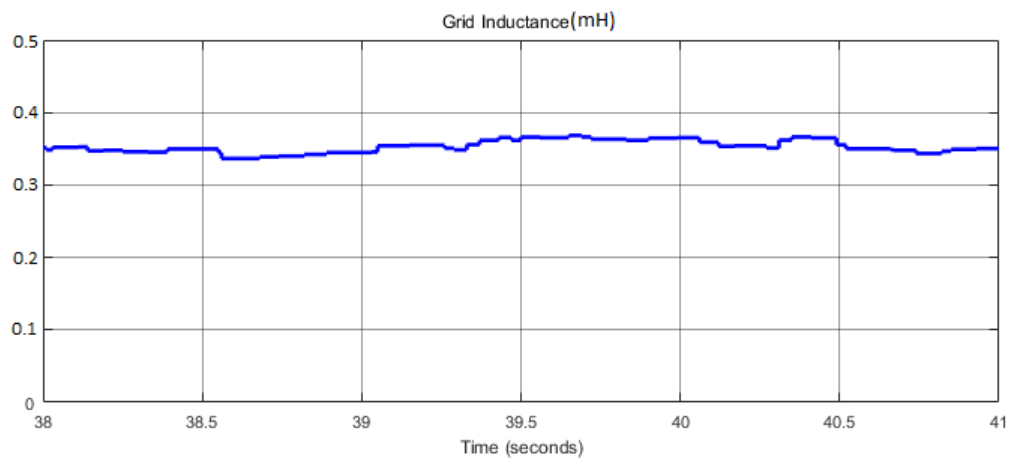
Figure 5.7. DC Link Voltage (CH1), PCC Voltage (CH2), Grid Current (CH3) and FFT of Grid Current (Math) without (a) and with (b) MLBS Signal under Weak Grid

5.2.2. Accuracy of the Estimated Grid Inductance

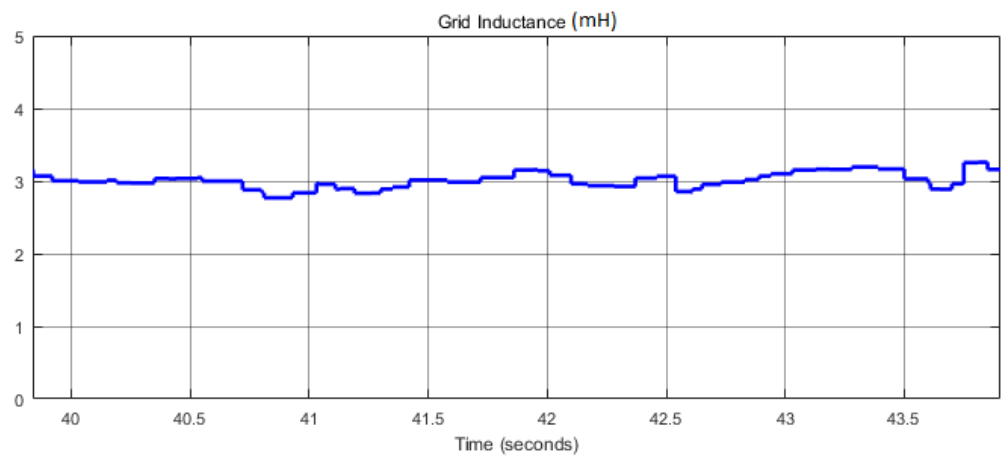
Accuracy of the grid inductance estimation is an important factor for the designed adaptive controller to avoid undesirable parameter changes. In the study, 127 bits long MLBS signal is generated at 5 kHz and so the estimation cycle becomes 25.4 ms. In order to increase the accuracy of the estimation averaging blocks are added to estimation models. Adding an averaging block provides more reliable results with the cost of longer transient durations which are long enough under real grid conditions. In this study, the measured PCC voltages and grid currents are averaged for 5 excitation cycles before transform the frequency domain by using FFT. Besides that the estimated inductance is averaged at the end. In this study, in order see the effects of change in PLL parameters the estimated inductance value is averaged over 20 excitation cycles. In order to see the estimated grid inductance, the real time data is send to a computer by Controller Area Network (CAN) communication and visualized by using MATLAB/Simulink. The estimated grid inductances under stiff and weak grid conditions are shown in Figure 5.8.

The transient of the averaged estimated inductance is given in Figure 5.9. When 2.8 mH inductor block is added to the system suddenly at the point which is stated with the red dashed line, the change of the estimated inductance is shown. With the inductance of isolation transformer, the total grid inductance is increased to 3 mH and nearly 2.5 s is required to reach steady-state.

The time duration to reach the steady state can be decreased and still accurate results can be taken from the model but in this study, the duration is kept long in order to see the unstable and stable operations when the grid inductance is suddenly changed.



(a)



(b)

Figure 5.8. Estimated Grid Inductance Value under Stiff (a) and Weak (b) Grid Conditions

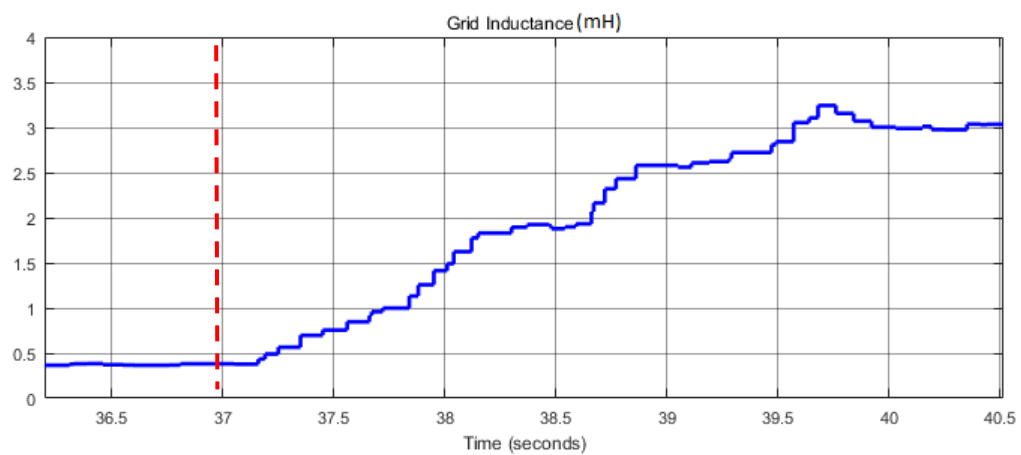
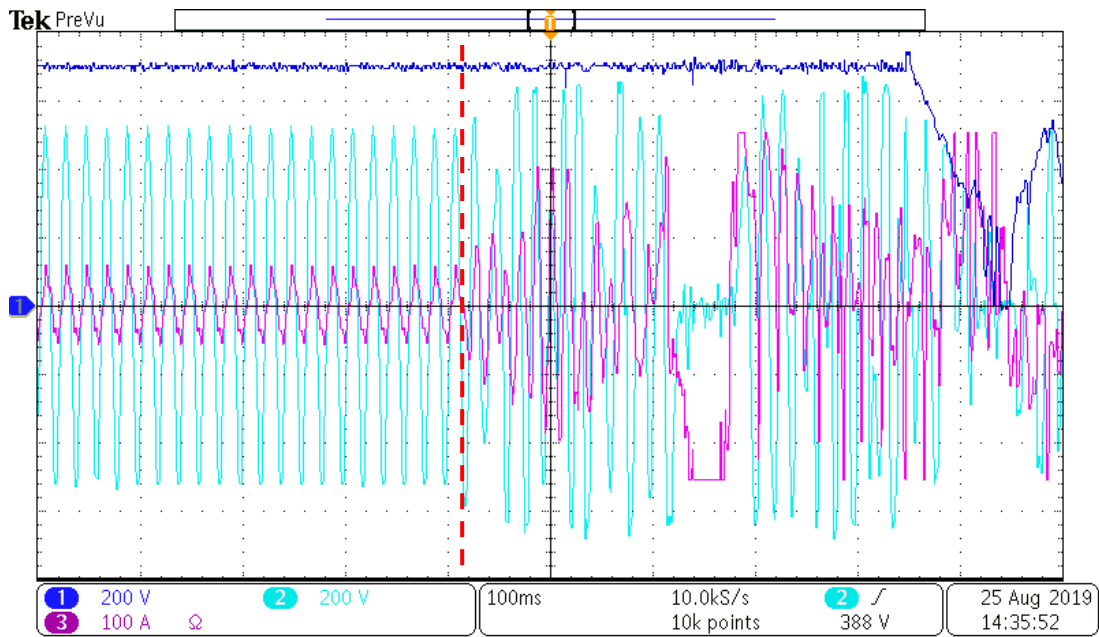


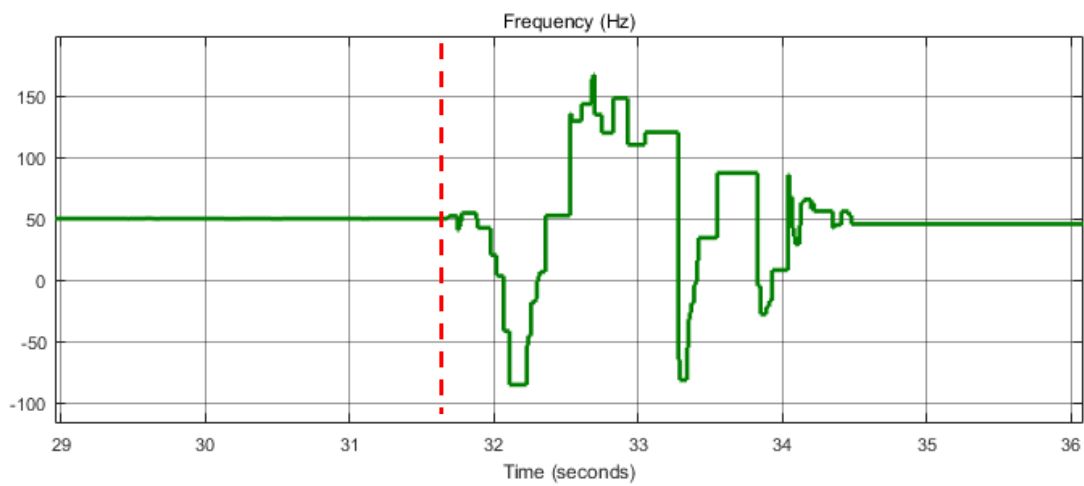
Figure 5.9. The Transient of the Averaged Estimated Inductance from 0.3 to 3 mH

5.3. Sudden Grid Inductance Change

In Chapter 4.6, nonlinear model of the system is simulated in order to see the differences between two PLL responses under sudden grid inductance change. For the experiment, the grid impedance is suddenly increased from 0.3 to 3 mH by using parallel connected circuit breaker while injecting 50 A_{peak} to the grid. The change of DC link voltage, grid voltage, injected grid current and estimated frequency are given by Figure 5.10 for $T_s = 0.1$ s. The grid inductance change points are shown by dashed red lines. As seen that, the system with PLL settling time $T_s = 0.1$ s becomes unstable when the grid inductance is changed. At the end, DC voltage source trips and stops the operation since the high amount of currents are injected to the source. On the other hand, as seen in Figure 5.11 the system with PLL settling time $T_s = 0.3$ s, maintains stable operation under sudden inductance change. The quality of the injected current increases because of high inductance. As expected, the PLL with lower bandwidth provided stable operation under weak grid conditions. The impedance based stability analysis which are performed at Chapter 4 shows that the increase in grid impedance causes impedance mismatches between q components of inverter output and grid impedances. As shown by Figure 4.13 and Figure 4.15, the system is not stable under weak grid conditions with PLL settling time $T_s = 0.1$ s. However, when the settling time is increased to $T_s = 0.3$ s, the system maintains stable operation under weak grid conditions. By the experiments whose results are given by Figure 5.10 and Figure 5.11, the performed stability analysis are verified.

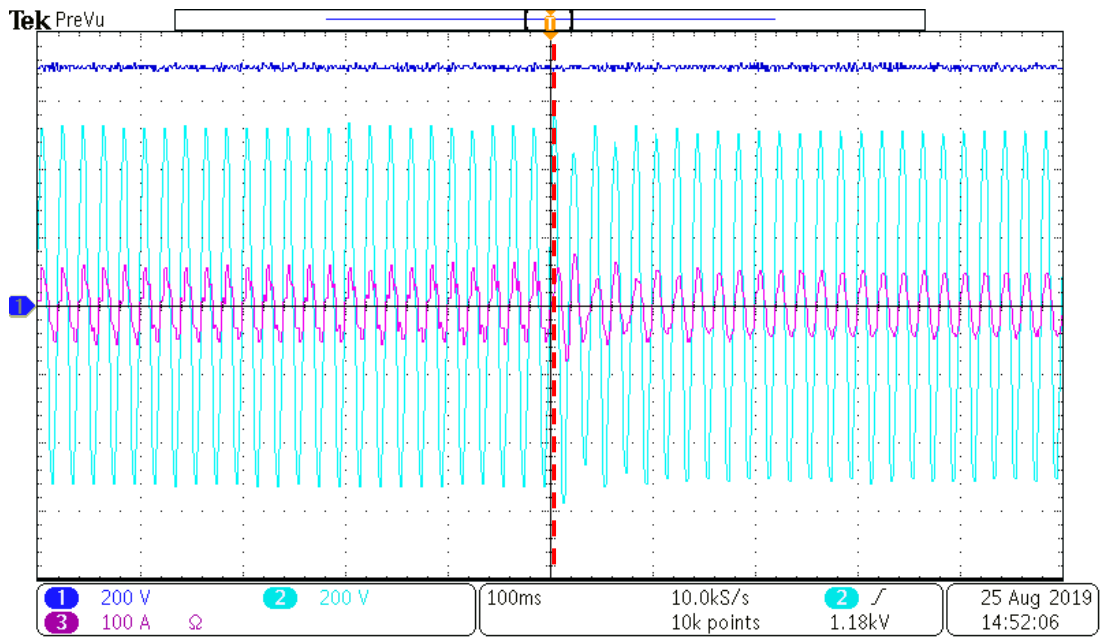


(a)

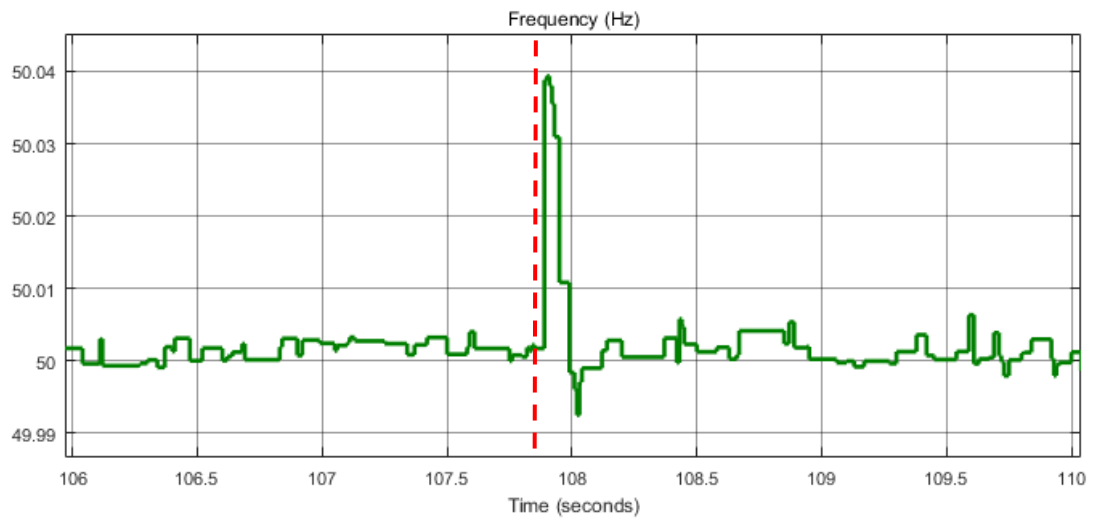


(b)

Figure 5.10. The Change of DC Link Voltage (CH1,a), PCC Voltage (CH2,a), Injected Grid Current (CH3,a) and Estimated Frequency (b) at Sudden Grid Inductance Change with $T_s = 0.1$



(a)



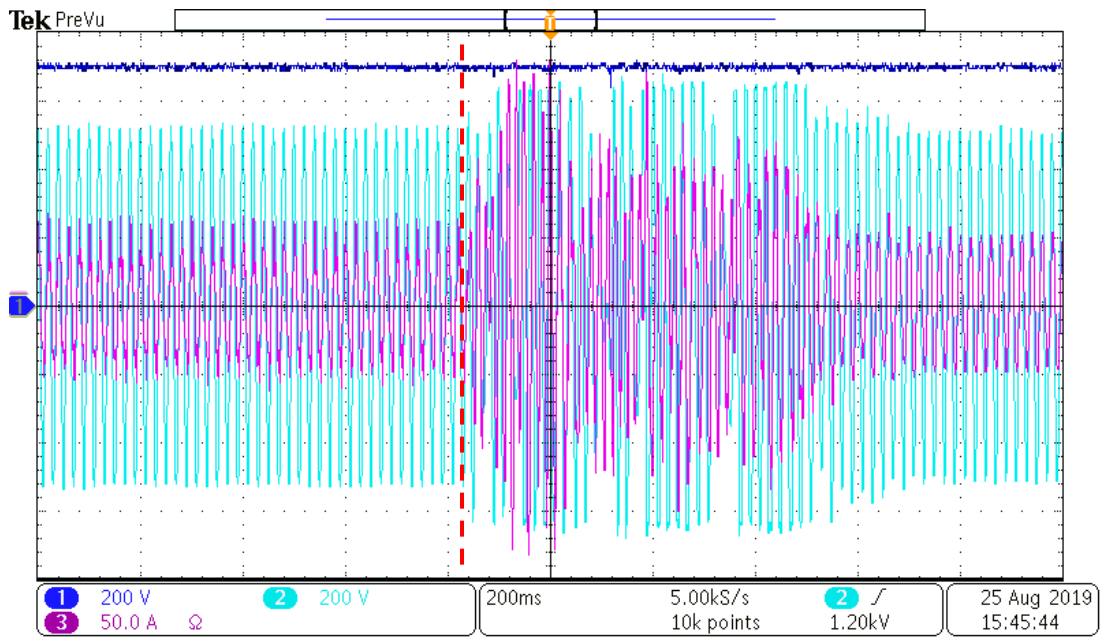
(b)

Figure 5.11. The Change of DC Link Voltage (CH1,a), PCC Voltage (CH2,a), Injected Grid Current (CH3,a) and Estimated Frequency (b) at Sudden Grid Inductance Change with $T_s = 0.3$

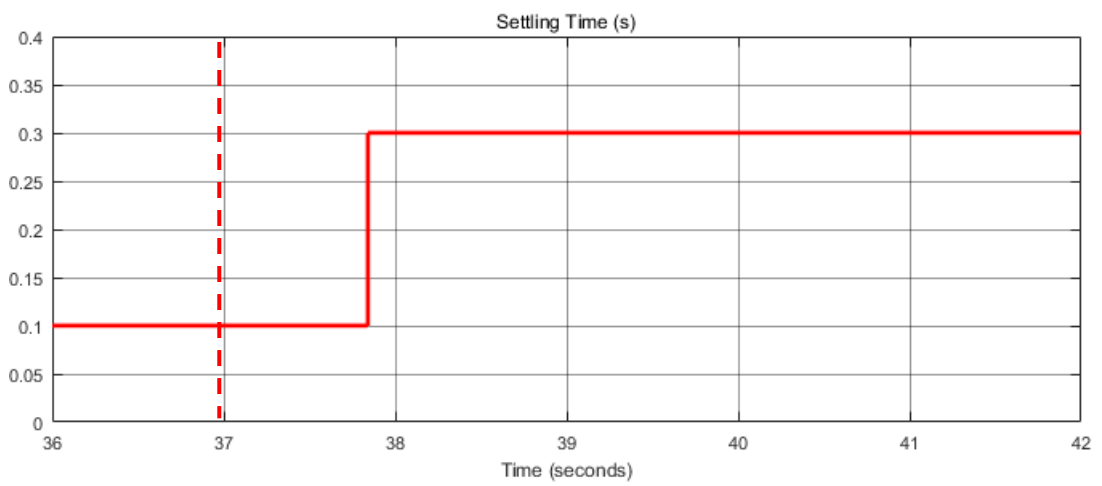
5.4. Adaptive Control

The impedance based stability analysis with different PLL parameters is performed in Chapter 4.5 and the results are verified by simulations in Chapter 4.6 and experiments in Chapter 5.3. It is concluded that increasing settling time decreases PLL bandwidth and provides slower response. Thus, the system stability is maintained under weak grid conditions thanks to slower response of the PLL. However, a system with slow dynamic responses is not desired under stiff grid conditions. For this reason, an adaptive controller is implemented by modifying settling time of the PLL in this study.

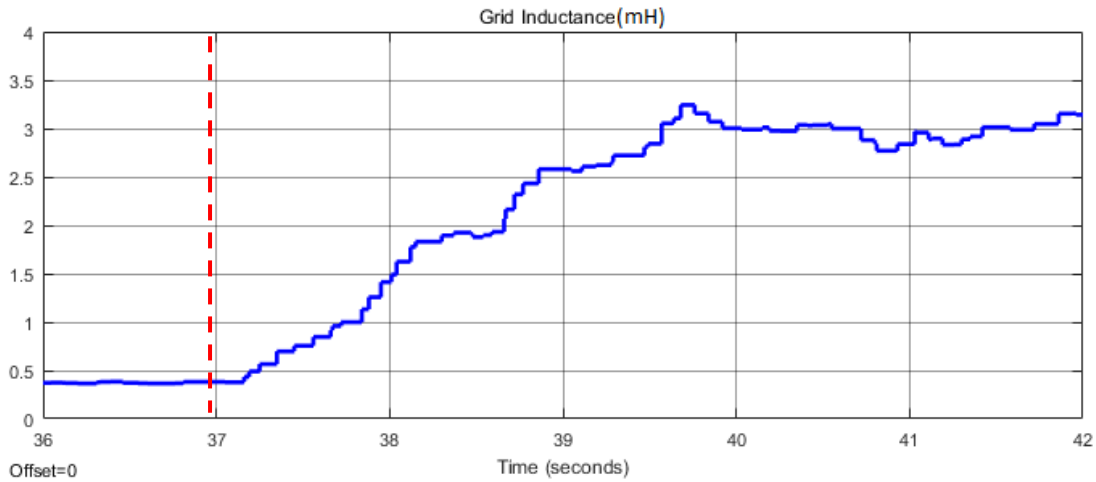
For the experiments, two cases are considered as stiff and weak grid conditions. Firstly, input and output of the inductor block is short circuited via circuit breaker and only inductance of the isolation transformer 0.2 mH is considered as stiff grid. Secondly, while supplying the current to the grid, the circuit breaker is opened suddenly and the grid inductance is increased to 3 mH to simulate weak grid conditions. Adaptive controller increases settling time of the PLL from 0.1 to 0.3 s , when the grid inductance exceeds 1 mH . The changes of the DC link voltage, PCC voltage, injected grid current, PLL settling time, estimated grid inductance and frequency are shown in Figure 5.12 when the grid inductance is suddenly changed from 0.3 to 3 mH . The grid inductance change points on the figures are shown by dashed red lines. When grid inductance is changed, instability occurs at the system and high amount of currents are injected to the grid with the deviation of estimated frequency from 50 Hz . Estimated grid inductance starts to increase and reaches 1 mH after approximately 0.8 s later. At this point, PLL settling time is changed from 0.1 to 0.3 s and deviated grid frequency is recovered to 50 Hz . At the end, injected grid current follows the given current reference.



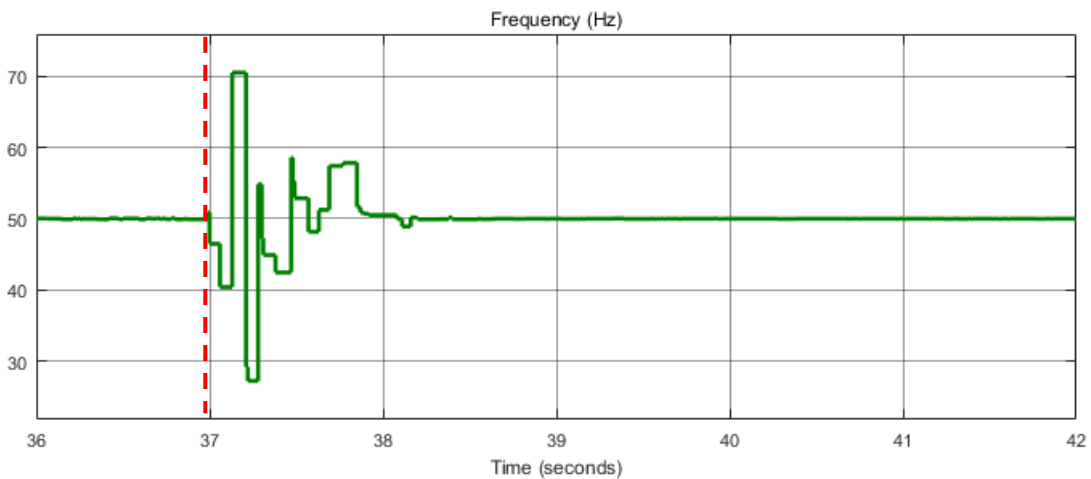
(a)



(b)



(c)

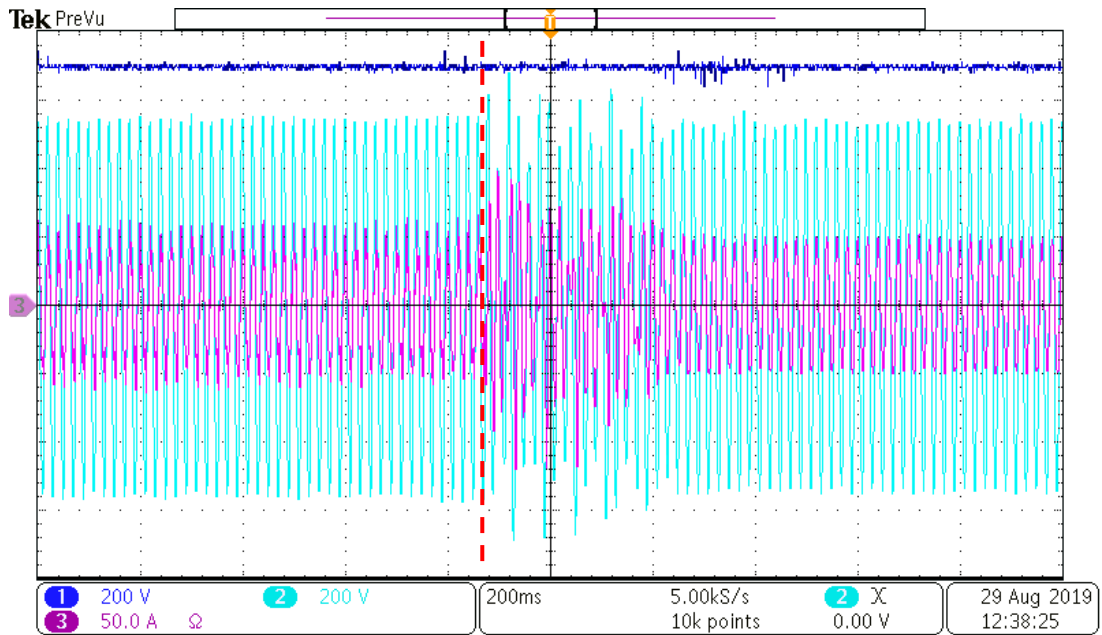


(d)

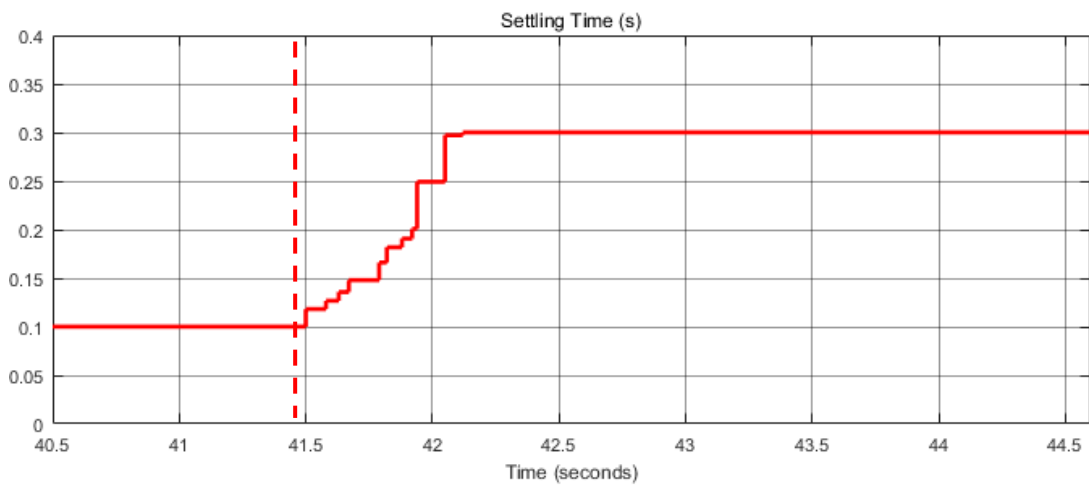
Figure 5.12. DC Link Voltage (CH1,a), PCC Voltage (CH2,a), Grid Current (CH3,a), PLL Settling Time (b), Estimated Grid Inductance (c) and Frequency (d) when Grid Inductance is suddenly changed from 0.3 to 3mH

For this study, recovering the system stability takes nearly 0.8 s. If the trip delay of the system is shorter than this value, the system trips and stops the operation. The given method is improved by defining a proportional relation between the settling time and grid inductance. The upper and lower limits for settling times are again determined as 0.1 and 0.3 s but it continuously increases between 0.4 and 1 mH. Thus, the delay between the sudden inductance change and settling time change reduces and instable operation duration becomes shorter. The changes of DC link voltage, PCC voltage,

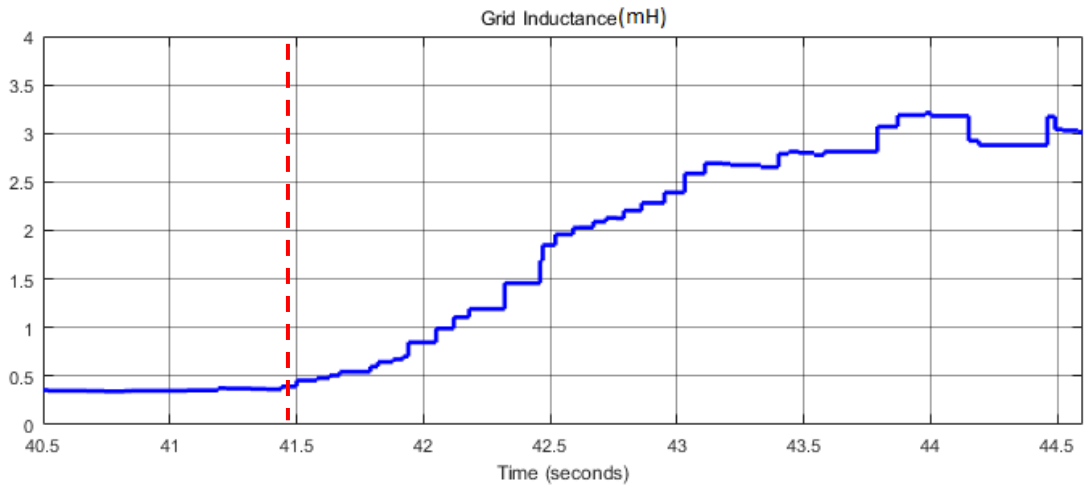
injected grid current, PLL settling time, estimated grid inductance and frequency with improved method are shown in Figure 5.13 when the grid inductance is changed from 0.3 to 3 mH. The grid inductance change points on the figures are shown by dashed red lines. As seen that the estimated frequency recovers to 50 Hz less than 0.3 s and the injected current follows the given reference.



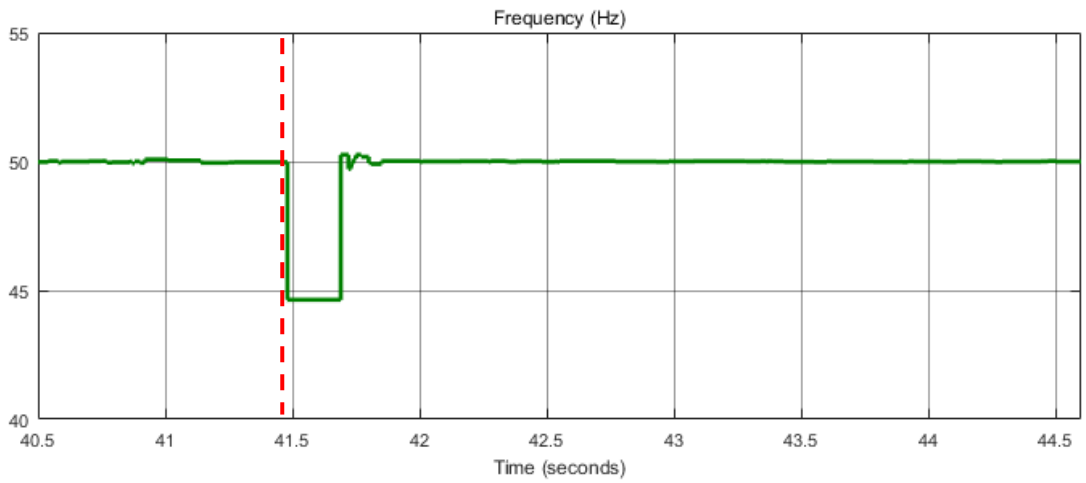
(a)



(b)



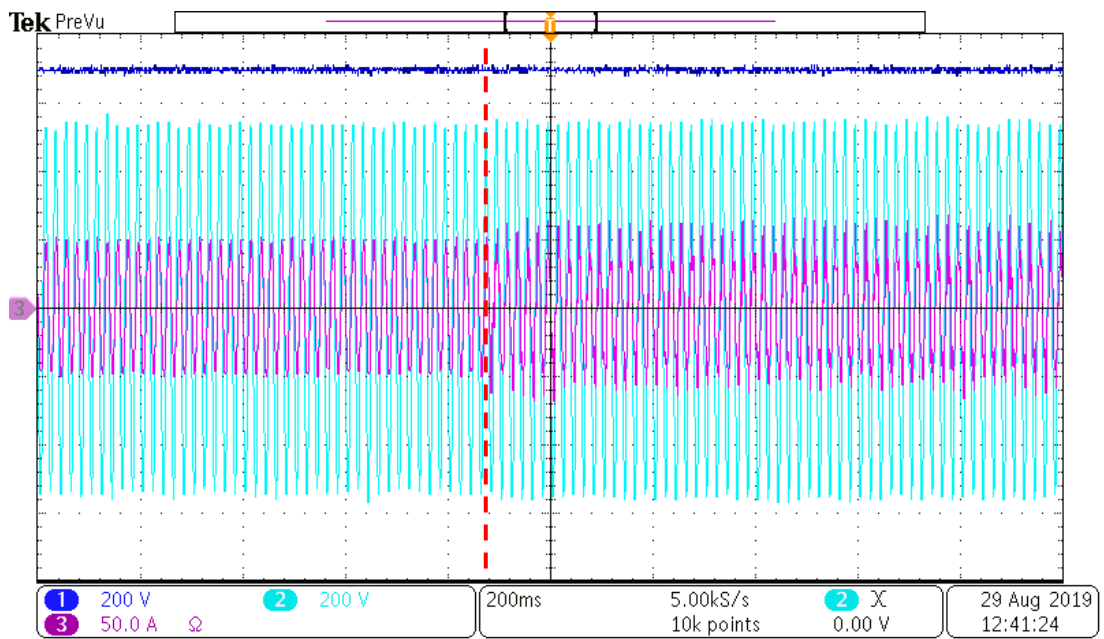
(c)



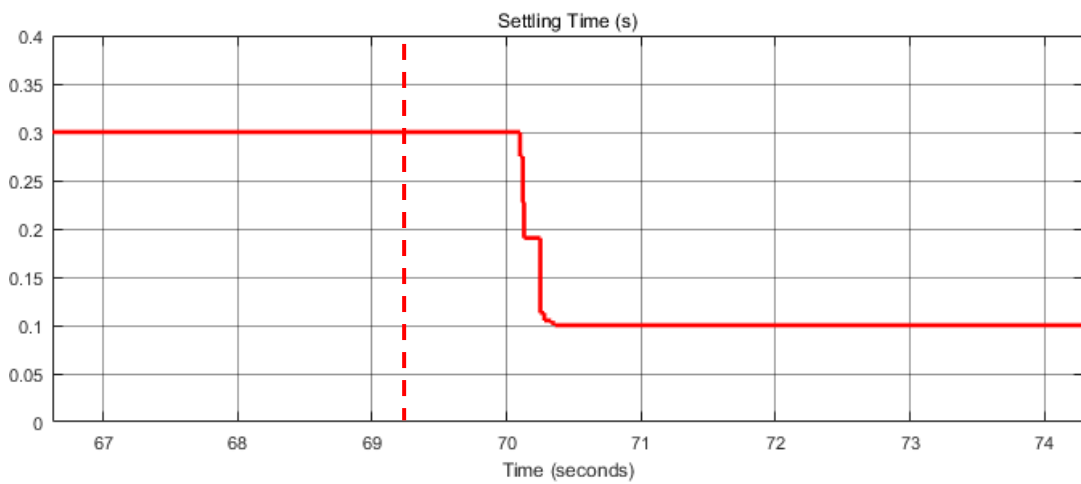
(d)

Figure 5.13. DC Link Voltage (CH1,a), PCC Voltage (CH2,a), Grid Current (CH3,a), PLL Settling Time (b), Estimated Grid Inductance (c) and Frequency (d) with Improved Method when Grid Inductance is changed from 0.3 to 3mH

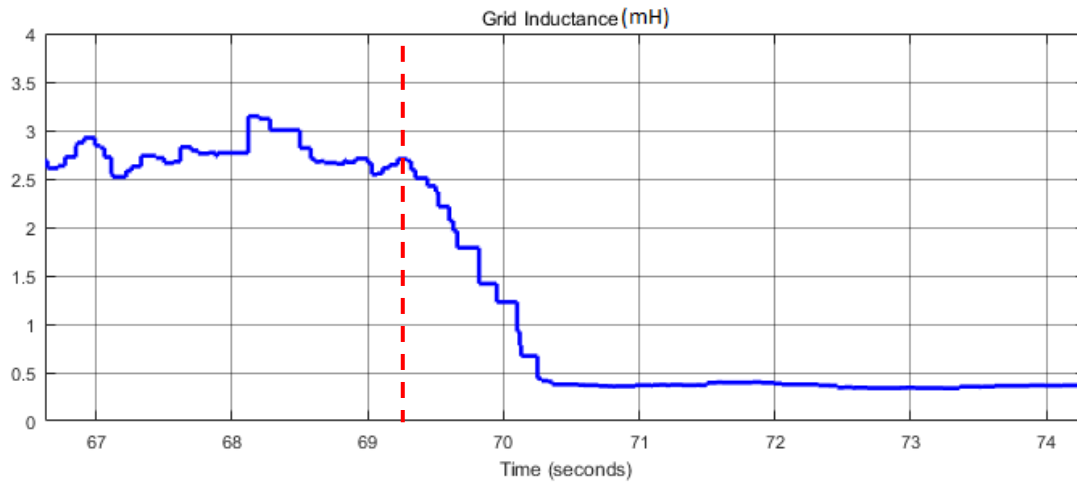
Until that point, as the tough case to maintain stability, transitions from stiff to weak grid conditions are considered. In Figure 5.14, the results are given for the transition from weak to stiff grid conditions. The grid inductance change points on the figures are shown by dashed red lines. As expected, any deviation at the frequency is not observed and the system maintains stable operation.



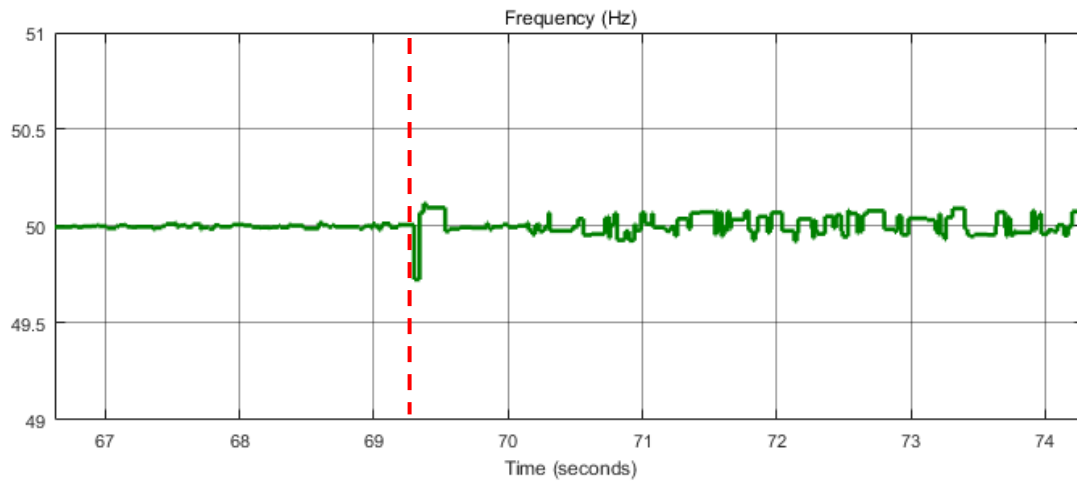
(a)



(b)



(c)



(d)

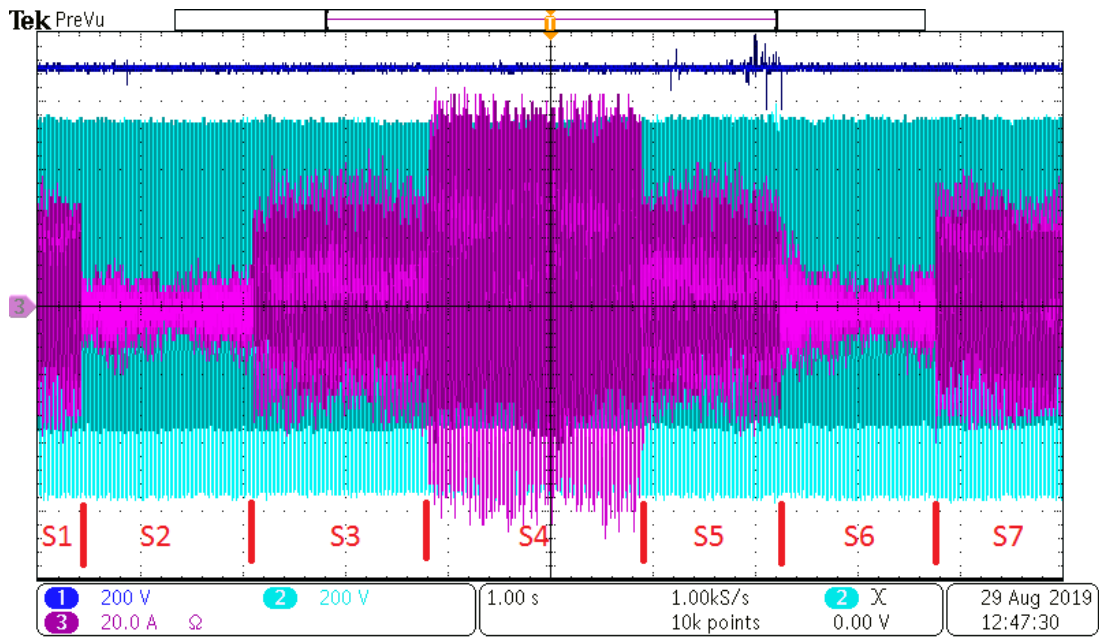
Figure 5.14. DC Link Voltage (CH1,a), PCC Voltage (CH2,a), Grid Current (CH3,a), PLL Settling Time (b), Estimated Grid Inductance (c) and Frequency (d) with Improved Method when Grid Inductance is changed from 3 to 0.3mH

5.5. Operation under Stiff and Weak Grid Conditions

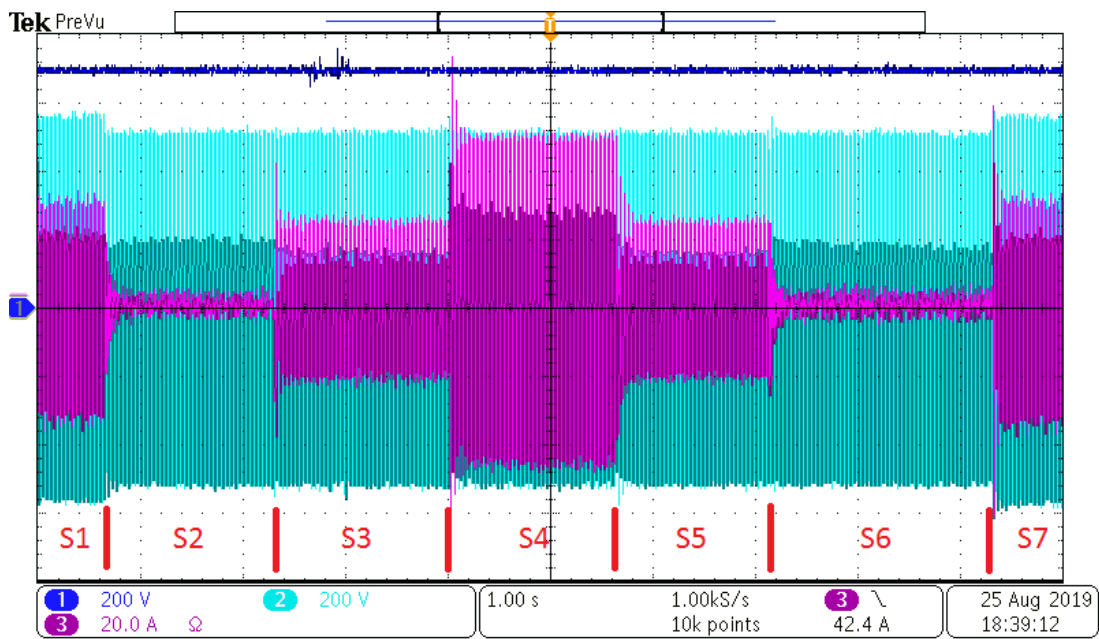
The designed controller provides stable operation under both stiff and weak grid conditions. The injected PRBS signal does not have a negative impact on the system stability. By considering d and q components grid current references, the system response is evaluated by 7 steps. At S1 and S7 regions, d and q component grid current references are zero and reactive current drawn by LCL filter capacitors is drawn from the grid. At S2 and S6 regions, reactive current drawn by LCL filter capacitors is provided from grid connected VSI but the injected active power to the grid equals to zero. At S3 and S5 regions, half of the rated active power is injected to the grid with unity power factor. At S4 region, full load condition is performed without injecting reactive power. In Figure 5.15, different operating points of the grid connected VSI are given by the current references. The current references of the given regions in the following figures are shown in Table 5.5. Under weak grid conditions, high frequency components on the grid current generated by PWM switching are filtered and do not appear on the measurements.

Table 5.5. Current References for the Given Regions in Following Figures

Area	i_{dref}	i_{qref}
S1	0	0
S2	0	30
S3	25	30
S4	50	30
S5	25	30
S6	0	30
S7	0	0



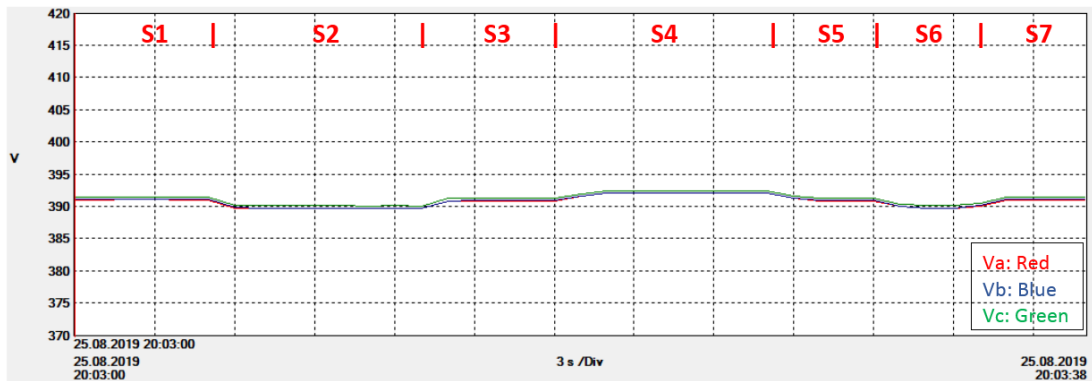
(a)



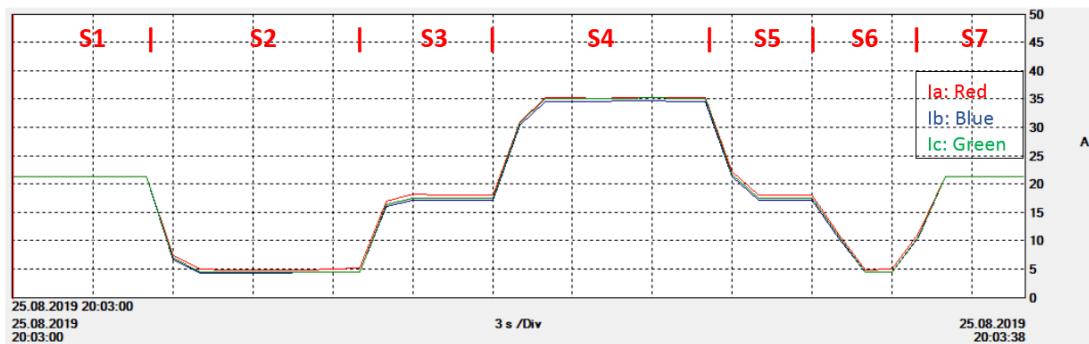
(b)

Figure 5.15. DC Link Voltage (CH1), PCC Voltage (CH2), Grid Current (CH3) under Stiff (a) and Weak (b) Grid Conditions

The applied sequences in Figure 5.15 are spread out longer durations and the change of PCC voltage, grid current, injected power, power factor and grid current THD values are given as in Figure 5.16 and Figure 5.17 for stiff and weak grid conditions respectively. The measurements are taken by the power analyzer with a period of 1 s.



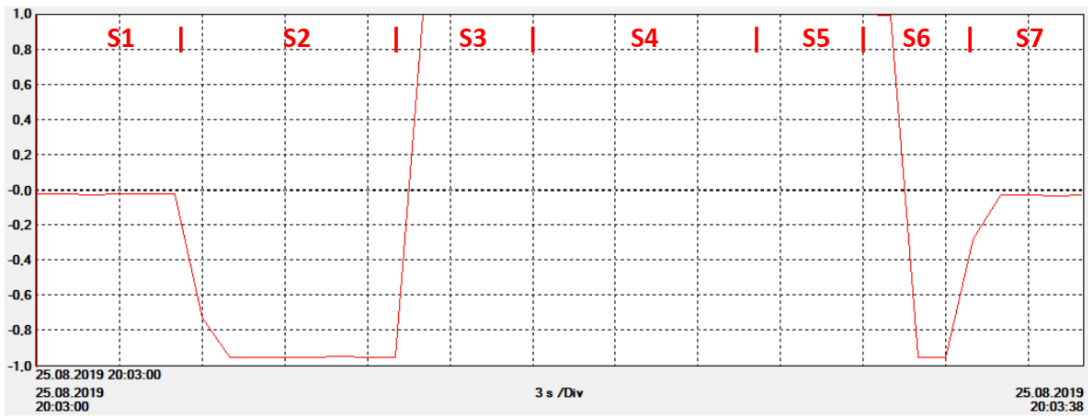
(a)



(b)



(c)

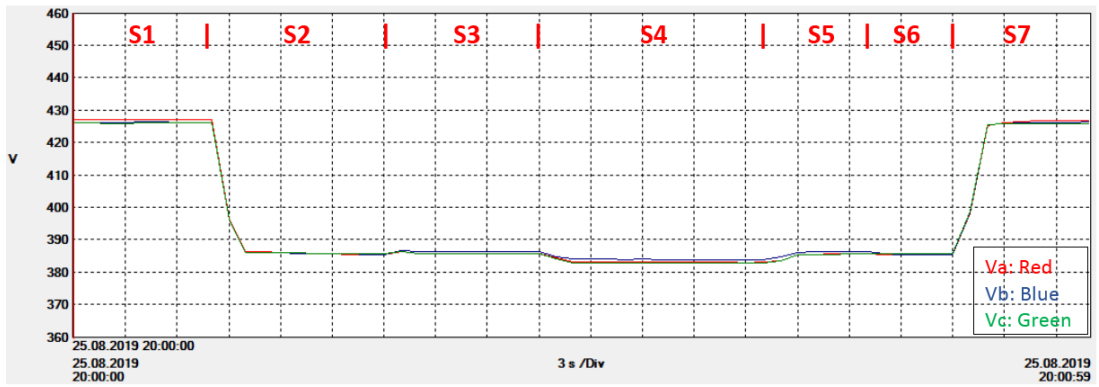


(d)



(e)

Figure 5.16. PCC Voltage (a), Grid Current (b), Injected Power (c), Power Factor (d) and THD of the Injected Grid Current under Stiff Grid Conditions



(a)



(b)



(c)



(d)



(e)

Figure 5.17. PCC Voltage (a), Grid Current (b), Injected Power (c), Power Factor (d) and THD of the Injected Grid Current under Weak Grid Conditions

When the obtained results are compared for stiff and weak grid conditions, the remarks which should be pointed out are listed as follows:

- Under weak grid conditions, reactive component of the injected grid current has more impact on the PCC voltage. When d and q component grid current references equal to zero (S1 and S7 region), consumed reactive power by LCL filter capacitors are provided from the grid. While this current is drawn under stiff grid, PCC voltage nearly constant around 390 V. On the other hand, when this current is drawn under weak grid, the PCC voltage increases to 427 V.
- When the q component of current reference is set as to provide the reactive power consumed by the LCL filter capacitors, unity power factor operation is

maintained with different load conditions. Weak grid conditions have no adverse effects on unity power factor operation.

- The measured THD values for grid currents are higher under stiff grid conditions because high frequency components of the currents are filtered by grid inductance under weak grid conditions. Besides that, grid current THD under stiff grid is higher than expected since the setup includes two serial connected inverters as the system under test and grid simulator. The inverters includes closed loop controllers which try to reach steady-state point. Thus, they adversely affect to stabilities of each other. At no load condition (S2 and S6 region), the THD values should not be considered because the fundamental component of the grid current equals to zero.

5.6. Summary

In this chapter, the analyses which are performed at Chapter 3 and 4 are verified by experimental results. Firstly, harmonic compensation performance of the grid connected VSI analyzed when 5th and 7th harmonic contents are added to fundamental grid voltage. Secondly, grid inductance estimation is investigated by considering the distortions caused by MLBS injection and accuracy of the estimation. After that system stability is examined in detailed with different PLL parameter when the grid inductance is suddenly increased. The effects of the PLL response time on the system stability is considered. Next, an adaptive controller is proposed and its performance is analyzed under transient and steady-state conditions. Finally, the adaptive controller is performed with different load conditions and the changes of PCC voltage, grid current, injected power, power factor and grid current THD values are examined.

CHAPTER 6

CONCLUSIONS

In this study, design of a grid impedance estimation based adaptive controller for DPGSSs is presented. The study focuses on the stable operation of the grid connected VSIs under distorted and weak grid conditions. At first the controller of the system is designed by considering the stiff grid conditions. After that the impedance based stability analysis is performed based on the weak grid conditions. According to these analysis, different PLL gain parameters are determined for stiff and weak grid conditions. Stable operations with the determined parameters are verified by simulations and experimental results.

6.1. Summary

In order to operate under distorted grid conditions, PR+HC is used as current controller. Harmonic compensation part of the controller attenuate the harmonic contents of the grid currents at desired frequencies. In the study, 5th and 7th harmonics of the grid currents are eliminated. The frequency of the eliminated harmonic content should be inside the controller bandwidth. To increase the controller bandwidth proportional gain of the current controller should be increased but it is limited by the high frequency poles of LCL filter. The upper limits of the current controller gains were determined by using root locus analysis.

In order to operate under weak grid conditions, PLL bandwidth modification is required. In the study, PLL parameters are determined according to stiff grid conditions. When impedance based stability analysis is applied, it is seen that the system is unstable under weak grid condition. Bandwidth of the PLL must be decreased for stable operation under weak grid. However, lower PLL bandwidth causes slower dynamic responses under transient conditions. For this reason, an

adaptive controller is required for weak grid condition. An adaptive controller is proposed by measuring the grid impedance in real time.

To measure the grid impedance, MLBS signal is injected to the grid with d component of current reference. The voltage and current signals at the PCC were transformed to frequency domain by using FFT method. The frequency responses of the voltage and current are divided and so the frequency response of the grid impedance was obtained at a broad frequency range. The inductance of the grid was extracted from the obtained impedance and averaged up to 1 kHz in order to increase the accuracy of the measurement.

The impedance based stability analysis is performed for the overall system. The analysis considers the inverter output impedance and grid impedance. The output impedance of the inverter is derived in the study by using small signal model for both d and q components. It is observed that d component of the output impedance and grid impedance does not cause instability at whole frequency range. However, q components of the impedances can cause instability based on PLL control bandwidth.

In the experiments, the grid inductance is suddenly increased and weak grid conditions are simulated. The inverter estimated the grid inductance adaptively changes the PLL settling time. Instability occurs at the change instant and frequency estimated by the PLL deviates from 50 Hz . After settling time is changed, the estimated frequency recovers to 50 Hz and inverter maintains its stable operation. Different load conditions are performed to see the stable operation with PRBS injection and adaptive control.

6.2. Contributions to the Field

The thesis presents a comprehensive study for the controller design of grid connected VSIs. Through the study, lots of mathematical models are derived and analysis are performed. Step by step design procedure of LCL filter with comparison of series R and shunt R-C passive damping methods is offered. Mathematical model of LCL filter is derived and pole zero map of the filter is plotted. Locations of high frequency poles are determined based on different damping methods and undamped cases. The relation

between the stability and high frequency poles of the system is explained. The design of a stable system is investigated in detail by using discrete Root locus analysis.

The main contribution of the thesis is the adaptive controller design for weak grid conditions. Real time grid impedance estimation technique is developed and small signal model of the inverter is derived. Impedance based stability analysis is implemented based on Nyquist and Bode stability criterions. The obtained results are verified with the experimental setup.

6.3. Future Work

The following topics can be covered in further researches:

- In this study, averaging procedure is used to increase the measurement accuracy with the cost of long transient durations. The proposed method can be improved by increasing the accuracy of the inductance measurements without using averaging blocks.
- In this study, impedance based stability analysis is performed and a relation between grid inductance and PLL settling time is defined. The applied analysis can be performed in real time and PLL parameters can change continuously.
- The adaptive method can be applied to harmonic compensation. FFT is implemented to grid voltage and its harmonic content is derived. If 5th or 7th harmonic is high, the current controller bandwidth is extended by increasing current controller gain parameters.
- The proposed MLBS injection and inductance estimation method can be performed to determine the motor parameters in a drive application. In order to estimate winding resistances and inductances, MLBS signal can be injected by motor driver and FFT is implemented.

REFERENCES

- [1] Agora Energiewende and Sandbag, “The European Power Sector in 2018. Up-to-date analysis on the electricity transition,” *State of Affairs and Review of Current Developments*, 2019.
- [2] C. Burgos-Mellado, A. Costabeber, M. Sumner, R. Cárdenas-Dobson, and D. Sáez, “Small-signal modelling and stability assessment of phase-locked loops in weak grids,” *Energies*, vol. 12, no. 7, 2019.
- [3] A. Adib and B. Mirafzal, “Stability in Weak Grids”, February 2019.
- [4] A. Adib, B. Mirafzal, X. Wang, and R. Blaabjerg, “On stability of voltage source inverters in weak grids,” *IEEE Access*, vol. 6, pp. 4427–4439, 2017.
- [5] T. Suntio, T. Messo, and J. Puukko, *Power Electronic Converters*. 2017.
- [6] H. S. Kim and D. D.-C. Lu, “Wind Energy Conversion System from Electrical Perspective—A Survey,” *Smart Grid Renew. Energy*, vol. 01, no. 03, pp. 119–131, 2010.
- [7] F. Iov, M. Ciobotaru, and F. Blaabjerg, “Power electronics control of wind energy in distributed power systems,” in *11th International Conference on Optimization of Electrical and Electronic Equipment, OPTIM 2008*, 2008.
- [8] A. D. Hansen, F. Iov, F. Blaabjerg, and L. H. Hansen, “Review of Contemporary Wind Turbine Concepts and Their Market Penetration,” *Wind Eng.*, vol. 28, no. 3, pp. 247–263, 2004.
- [9] European Wind Energy Association, “Large scale integration of wind energy in the European power supply: Analysis, issues and recommendations,” *Rep. Eur. Wind Energy Assoc.*, pp. 1–172, 2005.
- [10] “Elektrik piyasası şebeke yönetmeliğinde değişiklik yapılmasına ilişkin yönetmelik.” p. Resmi Gazete, 3 January 2013, Number: 28517.
- [11] IEC, “International Standard - Wind Turbines,” *Int. Stand.*, vol. 2005, 2005.
- [12] IEC 61400-21-1:2019, “IEC 61400-21-1:2019 Wind energy generation systems - Measurement and assessment of electrical characteristics – Wind turbines,” *Int. Stand.*, vol. 2004, 2019.
- [13] H. Emanuel, M. Schellschmidt, S. Wachtel, and S. Adloff, “Power quality measurements of wind energy converters with full-scale converter according to IEC 61400-21,” *2009 10th Int. Conf. Electr. Power Qual. Util. EPQU'09*, 2009.
- [14] R. Teodorescu, M. Liserre, and P. Rodriguez, *Grid Converters for Photovoltaic*

and *Wind Power Systems Chapter Grid Converter Structures for Wind Turbine Systems*. 2011.

- [15] O. Anaya-Lara, N. Jenkins, J. Ekanayake, P. Cartwright, M. Hughes, *Wind energy generation : modelling and control*. 2009.
- [16] J. L. Domínguez-García, O. Gomis-Bellmunt, L. Trilla-Romero, and A. Junyent-Ferré, “Indirect vector control of a squirrel cage induction generator wind turbine,” *Comput. Math. with Appl.*, vol. 64, no. 2, pp. 102–114, 2012.
- [17] V. P. B. Júnior, R. V. Jacomini, and A. J. S. Filho, “Simulation Study of Squirrel Cage Induction Generator Fed by a Back-to-Back Converter and by using a LCL filter,” pp. 572–580, 2013.
- [18] T. A. Novotny, Donald W.;Lipo, *41. Vector Control and Dynamics Of AC Drives*. 1998.
- [19] R. Teodorescu and F. Blaabjerg, “Flexible control of small wind turbines with grid failure detection operating in stand-alone and grid-connected mode,” *IEEE Trans. Power Electron.*, vol. 19, no. 5, pp. 1323–1332, 2004.
- [20] R. Teodorescu, F. Blaabjerg, U. Borup, and M. Liserre, “A new control structure for grid-connected LCL PV inverters with zero steady-state error and selective harmonic compensation,” pp. 580–586, 2004.
- [21] Seung-Ho Song, Shin-il Kang, and Nyeon-kun Hahm, “Implementation and control of grid connected AC-DC-AC power converter for variable speed wind energy conversion system,” vol. 00, no. C, pp. 154–158, 2003.
- [22] F. Blaabjerg, R. Teodorescu, M. Liserre, and A. V. Timbus, “Overview of control and grid synchronization for distributed power generation systems,” *IEEE Transactions on Industrial Electronics*, vol. 53, no. 5, pp. 1398–1409, 2006.
- [23] M. P. Kazmierkowski, F. Blaabjerg, and R. Krishnan, *Control in Power Electronics Selected Problems*. 2001.
- [24] Siyu Gao and M. Barnes, “Phase-locked loop for AC systems: analyses and comparisons,” *6th IET Int. Conf. Power Electron. Mach. Drives (PEMD 2012)*, no. 1, pp. A21–A21, 2012.
- [25] P. Rodríguez, A. Luna, R. S. Muñoz-Aguilar, I. Etxeberria-Otadui, R. Teodorescu, and F. Blaabjerg, “A stationary reference frame grid synchronization system for three-phase grid-connected power converters under adverse grid conditions,” *IEEE Trans. Power Electron.*, 2012.
- [26] M. Barnes and Siyu Gao, “Phase-locked loops for grid-tied inverters: comparison and testing,” *8th IET Int. Conf. Power Electron. Mach. Drives (PEMD 2016)*, pp. 1-6, 2016.

- [27] A. Timbus, R. Teodorescu, F. Blaabjerg, and M. Liserre, "Synchronization methods for three phase distributed power generation systems. An overview and evaluation," in *PESC Record - IEEE Annual Power Electronics Specialists Conference*, 2005, vol. 2005, pp. 2474–2481.
- [28] P. Rodríguez, A. Luna, M. Ciobotaru, R. Teodorescu, and F. Blaabjerg, "Advanced grid synchronization system for power converters under unbalanced and distorted operating conditions," in *IECON Proceedings (Industrial Electronics Conference)*, 2006, pp. 5173–5178.
- [29] G.-C. Hsieh and J. C. Hung, "Phase-locked loop techniques- A survey," *IEEE Trans. Ind. Electron.*, vol. 43, no. 6, pp. 609–615, 1996.
- [30] D. N. Zmood and D. G. Holmes, "Stationary frame current regulation of PWM inverters with zero steady-state error," *IEEE Trans. Power Electron.*, vol. 18, no. 3, pp. 814–822, 2003.
- [31] R. Teodorescu, F. Blaabjerg, and M. Liserre, "A New Control Structure for Grid-Connected LCL PV Inverters with Zero Steady-State Error and Selective Harmonic Compensation," 2004.
- [32] R. Teodorescu, F. Blaabjerg, M. Liserre, and P. C. Loh, "Proportional-resonant controllers and filters for grid-connected voltage-source converters," 2006.
- [33] G. Zeng and T. W. Rasmussen, "Design of current-controller with PR-regulator for LCL-filter based grid-connected converter," *2nd Int. Symp. Power Electron. Distrib. Gener. Syst. PEDG 2010*, pp. 490–494, 2010.
- [34] Y. Han, P. Shen, and J. M. Guerrero, "Stationary frame current control evaluations for three-phase grid-connected inverters with PVR-based active damped LCL filters," *J. Power Electron.*, vol. 16, no. 1, pp. 297–309, 2016.
- [35] D. Zammit, C. Spiteri Staines, M. Apap, and J. Licari, "Design of PR current control with selective harmonic compensators using Matlab," *J. Electr. Syst. Inf. Technol.*, pp. 1–12, 2017.
- [36] E. Hendawi, F. Khater, and A. Shaltout, "Analysis, Simulation and Implementation of Space Vector Pulse Width Modulation Inverter," *Aee '10 Proc. 9th Wseas Int. Conf. Appl. Electr. Eng.*, pp. 124–131, 2010.
- [37] H. K. Kim, S. I. Ao, and M. A. Amouzegar, "Transactions on engineering technologies: Special issue of the world congress on engineering and computer science 2013," *Trans. Eng. Technol. Spec. Issue World Congr. Eng. Comput. Sci. 2013*, no. November, pp. 1–781, 2014.
- [38] Z. Yu, "Application Report SPRA524 Digital Signal Processing Solutions Space-Vector PWM With TMS320C24x/F24x Using Hardware and Software Determined Switching Patterns," no. March 1999, 1999.

- [39] G. Chen, J. Kang, and J. Zhao, "Numeric analysis and simulation of space vector pulse width modulation," *Adv. Eng. Softw.*, vol. 65, pp. 60–65, 2013.
- [40] S. N. Usluer, "Switch Mode Converter Based Damping of PWM Converter with LCL Type Filter for Grid Interface of Renewable Energy Systems," 2014.
- [41] V. Blasko and V. Kaura, "A novel control to actively damp resonance in input LC filter of a three-phase voltage source converter," *IEEE Trans. Ind. Appl.*, vol. 33, no. 2, pp. 542–550, 1997.
- [42] M. Liserre, A. Dell'Aquila, and F. Blaabjerg, "Genetic algorithm-based design of the active damping for an LCL-filter three-phase active rectifier," *IEEE Trans. Power Electron.*, vol. 19, no. 1, pp. 76–86, 2004.
- [43] E. Wu and P. W. Lehn, "Digital current control of a voltage source converter with active damping of LCL resonance," *IEEE Trans. Power Electron.*, vol. 21, no. 5, pp. 1364–1373, 2006.
- [44] M. H. Bierhoff and F. W. Fuchs, "Active damping for three-phase PWM rectifiers with high-order line-side filters," *IEEE Trans. Ind. Electron.*, vol. 56, no. 2, pp. 371–379, 2009.
- [45] B. Terzić, G. Majić, and A. Slutej, "Stability Analysis of Three-Phase PWM Converter with LCL Filter by Means of Nonlinear Model," *Automatika*, vol. 51, no. 3, pp. 221–232, 2010.
- [46] H. Temiz, E. Demirok, O. Keysan, A. Türkay, and B. Çetinkaya, "Performance comparison of passive series R and shunt R-C damped LCL filter for grid-connected inverters," *J. Eng.*, vol. 2019, no. 18, pp. 4698–4702, 2019.
- [47] M. Liserre, F. Blaabjerg, and S. Hansen, "Design and control of an LCL-filter-based three-phase active rectifier," *IEEE Trans. Ind. Appl.*, vol. 41, no. 5, pp. 1281–1291, 2005.
- [48] R. N. Beres, X. Wang, M. Liserre, F. Blaabjerg, and C. L. Bak, "A Review of Passive Power Filters for Three-Phase Grid-Connected Voltage-Source Converters," *IEEE J. Emerg. Sel. Top. Power Electron.*, vol. 4, no. 1, pp. 54–69, 2016.
- [49] R. Beres, X. Wang, F. Blaabjerg, C. L. Bak, and M. Liserre, "A review of passive filters for grid-connected voltage source converters," *Conf. Proc. - IEEE Appl. Power Electron. Conf. Expo. - APEC*, pp. 2208–2215, 2014.
- [50] IEEE Power and Energy Society, "IEEE Std 519-2014 (Revision of IEEE Std 519-1992), IEEE Recommended Practice and Requirements for Harmonic Control in Electric Power Systems," *IEEE Std 519-2014 (Revision IEEE Std 519-1992)*, vol. 2014, pp. 1–29, 2014.
- [51] M. Ben Saïd-Romdhane, M. W. Naouar, I. S. Belkhodja, and E. Monmasson,

- “Simple and systematic LCL filter design for three-phase grid-connected power converters,” *Math. Comput. Simul.*, 2016.
- [52] R. N. Beres, X. Wang, F. Blaabjerg, M. Liserre, and C. L. Bak, “Optimal design of high-order passive-damped filters for grid-connected applications,” *IEEE Trans. Power Electron.*, vol. 31, no. 3, pp. 2083–2098, 2016.
- [53] J. Dannehl, F. W. Fuchs, and S. Hansen, “PWM rectifier with LCL-filter using different current control structures,” *2007 Eur. Conf. Power Electron. Appl. EPE*, 2007.
- [54] J. Dannehl, C. Wessels, and F. W. Fuchs, “Limitations of voltage-oriented PI current control of grid-connected PWM rectifiers with LCL filters,” *IEEE Trans. Ind. Electron.*, vol. 56, no. 2, pp. 380–388, 2009.
- [55] M. Liserre, R. Teodorescu, and F. Blaabjerg, “Stability of photovoltaic and wind turbine grid-connected inverters for a large set of grid impedance values,” *IEEE Trans. Power Electron.*, 2006.
- [56] Hong-Seok Song, R. Keil, P. Mutschler, J. van der Weem, and Kwanghee Nam, “Advanced control scheme for a single-phase PWM rectifier in traction applications,” pp. 1558–1565, 2004.
- [57] N. Hoffmann, F. W. Fuchs, C. Kiel, and D.- Kiel, “Models and Effects of Different Updating and Sampling Concepts to the Control of Grid-Connected PWM Converters – A Study Based on Discrete Time Domain Analysis Keywords,” *Ger. Res.*, no. Cc, pp. 1–10, 2011.
- [58] V. Blasko and V. Kaura, “A novel control to actively damp resonance in input LC filter of a three-phase voltage source converter,” *IEEE Trans. Ind. Appl.*, vol. 33, no. 2, pp. 542–550, 1997.
- [59] J. Dannehl, F. W. Fuchs, S. Hansen, and P. B. Thøgersen, “Investigation of active damping approaches for PI-based current control of grid-connected pulse width modulation converters with LCL filters,” *IEEE Trans. Ind. Appl.*, vol. 46, no. 4, pp. 1509–1517, 2010.
- [60] S. Gao and B. Mike, “Phase-locked loop for AC systems: analyses and comparisons,” *6th IET Int. Conf. Power Electron. Mach. Drives (PEMD 2012)*, no. 1, pp. 1–6, 2012.
- [61] M. Barnes and Siyu Gao, “Phase-locked loops for grid-tied inverters: comparison and testing,” *8th IET Int. Conf. Power Electron. Mach. Drives (PEMD 2016)*, no. c, pp. 6.-6 ., 2016.
- [62] P. Rodríguez, R. Teodorescu, I. Candela, A. V. Timbus, M. Liserre, and F. Blaabjerg, “New positive-sequence voltage detector for grid synchronization of power converters under faulty grid conditions,” in *PESC Record - IEEE Annual Power Electronics Specialists Conference*, 2006.

- [63] P. Rodriguez, A. Luna, M. Ciobotaru, R. Teodorescu, and F. Blaabjerg, "Advanced grid synchronization system for power converters under unbalanced and distorted operating conditions," in *IECON Proceedings (Industrial Electronics Conference)*, 2006.
- [64] A. Timbus, R. Teodorescu, F. Blaabjerg, and M. Liserre, "Synchronization methods for three phase distributed power generation systems. An overview and evaluation," in *PESC Record - IEEE Annual Power Electronics Specialists Conference*, 2005.
- [65] P. Rodríguez, A. Luna, R. S. Muñoz-Aguilar, I. Etxeberria-Otadui, R. Teodorescu, and F. Blaabjerg, "A stationary reference frame grid synchronization system for three-phase grid-connected power converters under adverse grid conditions," *IEEE Trans. Power Electron.*, vol. 27, no. 1, pp. 99–112, 2012.
- [66] G. F. Franklin, J. D. Powell, A. Emami-Naeini, *Feedback Control of Dynamic Systems*. 2010.
- [67] R. Luhtala, T. Reinikka, T. Roinila, T. Messo, and J. Sihvo, "Improved Real-Time Stability Assessment of Grid-Connected Converters Using MIMO-Identification Methods," *2018 IEEE Energy Convers. Congr. Expo. ECCE 2018*, pp. 5322–5329, 2018.
- [68] J. Sun, "Impedance-based stability criterion for grid-connected inverters," *IEEE Trans. Power Electron.*, vol. 26, no. 11, pp. 3075–3078, 2011.
- [69] R. Luhtala, "Adaptive Control of Grid-Connected Inverters Adaptive Control of Grid-Connected Inverters", Tampere University, 2018.
- [70] L. Jessen and F. W. Fuchs, "Modeling of inverter output impedance for stability analysis in combination with measured grid impedances," *2015 IEEE 6th Int. Symp. Power Electron. Distrib. Gener. Syst. PEDG 2015*, no. 1, 2015.
- [71] R. C. Dorf and R. H. Bishop, *Modern Control Systems*. 2008.
- [72] B. Wen, R. Burgos, D. Boroyevich, P. Mattavelli, and Z. Shen, "AC Stability Analysis and dq Frame Impedance Specifications in Power-Electronics-Based Distributed Power Systems," *IEEE J. Emerg. Sel. Top. Power Electron.*, vol. 5, no. 4, pp. 1455–1465, 2017.
- [73] R. Luhtala, T. Messo, and T. Roinila, "Adaptive Control of Grid-Voltage Feedforward for Grid-Connected Inverters based on Real-Time Identification of Grid Impedance," *2018 Int. Power Electron. Conf. IPEC-Niigata - ECCE Asia 2018*, pp. 547–554, 2018.
- [74] M. Liserre, R. Teodorescu, and F. Blaabjerg, "Stability of photovoltaic and wind turbine grid-connected inverters for a large set of grid impedance values," *IEEE Trans. Power Electron.*, vol. 21, no. 1, pp. 263–271, 2006.

- [75] C. M. Hackl, "On the equivalence of proportional-integral and proportional-resonant controllers with anti-windup," pp. 1–9, 2016.
- [76] H. Mao, D. Boroyevich, and F. C. Y. Lee, "Novel reduced-order small-signal model of a three-phase PWM rectifier and its application in control design and system analysis," *IEEE Trans. Power Electron.*, vol. 13, no. 3, pp. 511–521, 1998.
- [77] A. Knop and F. W. Fuchs, "High frequency grid impedance analysis by current injection," in *IECON Proceedings (Industrial Electronics Conference)*, 2009, pp. 536–541.
- [78] M. Belkhat and K. A. Corzine, "New Techniques for Measuring Impedance Characteristics of Three-Phase AC Power Systems," *IEEE Trans. Power Electron.*, vol. 24, no. 7, pp. 1802–1810, 2009.
- [79] M. Jordan, H. Langkowski, T. Do Thanh, and D. Schulz, "Frequency dependent grid-impedance determination with pulse-width-modulation-signals," *2011 7th Int. Conf. Compat. Power Electron. CPE 2011 - Conf. Proc.*, pp. 131–136, 2011.
- [80] M. Cespedes and J. Sun, "Online grid impedance identification for adaptive control of grid-connected inverters," *2012 IEEE Energy Convers. Congr. Expo. ECCE 2012*, pp. 914–921, 2012.
- [81] T. Roinila, M. Vilkkko, and J. Sun, "Broadband methods for online grid impedance measurement," *2013 IEEE Energy Convers. Congr. Expo. ECCE 2013*, pp. 3003–3010, 2013.
- [82] T. Roinila, M. Vilkkko, and J. Sun, "Online grid impedance measurement using discrete-interval binary sequence injection," *IEEE J. Emerg. Sel. Top. Power Electron.*, vol. 2, no. 4, pp. 985–993, 2014.
- [83] M. Liserre, F. Blaabjerg, and R. Teodorescu, "Grid impedance estimation via excitation of LCL-filter resonance," *IEEE Trans. Ind. Appl.*, vol. 43, no. 5, pp. 1401–1407, 2007.
- [84] L. Harnefors, X. Wang, A. G. Yepes, and F. Blaabjerg, "Passivity-Based Stability Assessment of Grid-Connected VSCs-An Overview," *IEEE J. Emerg. Sel. Top. Power Electron.*, vol. 4, no. 1, pp. 116–125, 2016.
- [85] L. Harnefors, M. Bongiorno, and S. Lundberg, "Input-admittance calculation and shaping for controlled voltage-source converters," *IEEE Trans. Ind. Electron.*, vol. 54, no. 6, pp. 3323–3334, 2007.

APPENDICES

A. Transformations Between abc , $\alpha\beta$ and dq Reference Frames

$$\begin{bmatrix} x_\alpha \\ x_\beta \\ x_0 \end{bmatrix} = \begin{bmatrix} \frac{2}{3} & -\frac{1}{3} & -\frac{1}{3} \\ 0 & \frac{1}{\sqrt{3}} & -\frac{1}{\sqrt{3}} \\ \frac{1}{3} & \frac{1}{3} & \frac{1}{3} \end{bmatrix} \begin{bmatrix} x_a \\ x_b \\ x_c \end{bmatrix}$$

$$\begin{bmatrix} x_a \\ x_b \\ x_c \end{bmatrix} = \begin{bmatrix} 1 & 0 & 1 \\ -1/2 & \sqrt{3}/2 & 1 \\ -1/2 & -\sqrt{3}/2 & 1 \end{bmatrix} \begin{bmatrix} x_\alpha \\ x_\beta \\ x_0 \end{bmatrix}$$

$$\begin{bmatrix} x_d \\ x_q \\ x_0 \end{bmatrix} = \begin{bmatrix} \cos(\omega t) & \sin(\omega t) & 0 \\ -\sin(\omega t) & \cos(\omega t) & 0 \\ 0 & 0 & 1 \end{bmatrix} \begin{bmatrix} x_\alpha \\ x_\beta \\ x_0 \end{bmatrix}$$

$$\begin{bmatrix} x_\alpha \\ x_\beta \\ x_0 \end{bmatrix} = \begin{bmatrix} \cos(\omega t) & -\sin(\omega t) & 0 \\ \sin(\omega t) & \cos(\omega t) & 0 \\ 0 & 0 & 1 \end{bmatrix} \begin{bmatrix} x_d \\ x_q \\ x_0 \end{bmatrix}$$